Boston University

OpenBU **http://open.bu.edu**

Boston University Theses & Dissertations Boston University Theses & Dissertations

2020

Casimir cavity physics with MEMS: force measurements and detecting the Casimir energy

https://hdl.handle.net/2144/39361

Downloaded from DSpace Repository, DSpace Institution's institutional repository

BOSTON UNIVERSITY

COLLEGE OF ENGINEERING

Dissertation

CASIMIR CAVITY PHYSICS WITH MEMS: FORCE MEASUREMENTS AND DETECTING THE CASIMIR ENERGY

by

ALEXANDER C. STANGE

B.Sc., McGill University, 2012
M.Sc.Eng., University of Pennsylvania, 2016

Submitted in partial fulfillment of the
requirements for the degree of
Doctor of Philosophy

2020

© 2020 by
ALEXANDER C. STANGE
All rights reserved

Approved by

First Reader

David J. Bishop, Ph.D.
Professor of Electrical and Computer Engineering
Professor of Physics
Professor and Division Head of Materials Science and Engineering
Professor of Mechanical Engineering
Professor of Biomedical Engineering

Second Reader

David K. Campbell, Ph.D.
Professor of Physics
Professor of Electrical and Computer Engineering
Professor of Materials Science and Engineering

Third Reader

Thomas G. Bifano, Ph.D.
Professor of Mechanical Engineering
Professor of Materials Science and Engineering
Professor of Biomedical Engineering

Fourth Reader

Alice E. White, Ph.D.
Professor and Chair of Mechanical Engineering
Professor of Materials Science and Engineering
Professor of Biomedical Engineering
Professor of Physics

Acknowledgments

I would like to thank my parents, Barbara and Eric, who have been incredibly supportive at all times. My mother has pushed me to stay curious about topics outside of my own research, to read about new technologies, and to engage with people and communities around me in order to constantly improve myself and my career. My father has taught me how to tell a compelling story–an essential skill for a scientist that is regrettably not emphasized enough in our classrooms. I would also like to thank my sister Mia for always being there to talk to and to unpack issues with work or life, or just to exchange a hilarious text or two. And to my amazing partner, Theonie, whose wisdom, brilliance, and drive for excellence inspire me daily... I love you. I am so lucky to have the support of these wonderful people in my life.

To my friends at BU, especially Ilya and Roderic, thanks for all the coffees, strolls, lunches, Celtics games, attempted sports, and the other activities that make graduate student life truly fun.

Next, I would like to acknowledge my lab mates: Josh Javor, Corey Pollock, Rich Lally, Diego Perez, Lawrence Barrett, Pablo Del Corro, and Nicolas Fuhr. Also previous members, Jackson Chang, Tom Stark, Jeremy Reeves, and Matthias Imboden. You all are amazing researchers and it's been a privilege bouncing crazy ideas off one-another and collectively becoming smarter people (or at least convincing ourselves we are).

Especially, I would like to acknowledge and thank Diego Perez, whose ingenious and carefully thought-out devices and experiments have contributed to a large portion of the work presented in this dissertation. Diego has taught me so much about the

topics discussed here, both in theory and in practice, and has been a great teacher and friend along the way.

Additionally, Dr. Vladimir Askyuk has been an amazing mentor and advisor during the second half of my thesis. Thank you for always being available to talk through experimental problems and accurately and intuitively clear up any (many) theoretical quandaries I find myself in.

Lastly and most importantly, I want to express my deep gratitude to Professor David Bishop, who above all else cares about the success and well-being of his students. His inexhaustible wealth of knowledge and passion for innovation and discovery have shaped me into the researcher I am today. Thank you for giving me the opportunity to discover and develop my talents in this career. I could not have hoped for a better Doctoral experience, and I look forward to continuing to work together.

Alex Stange

CASIMIR CAVITY PHYSICS WITH MEMS: FORCE MEASUREMENTS AND DETECTING THE CASIMIR ENERGY

ALEXANDER C. STANGE

Boston University, College of Engineering, 2020

Major Professor: David J. Bishop, Ph.D.
Professor of Electrical and Computer Engineering
Professor of Physics
Professor and Division Head of Materials Science and Engineering
Professor of Mechanical Engineering
Professor of Biomedical Engineering

ABSTRACT

The Casimir Effect is a physical manifestation of quantum fluctuations of the electromagnetic vacuum. When two metal plates are placed closely together, typically much less than a micron, the long wavelength modes between them are frozen out, giving rise to a net attractive force between the plates, scaling as d^{-4} even when they are not electrically charged. Additionally, the lower density of electromagnetic modes inside the cavity compared to outside is thought to result in a "negative energy density," however this has never been proven experimentally. Due to the small scale of this effect, we use micro-electromechanical systems (MEMS) to investigate the forces and energies which arise between these conductive surfaces. This dissertation presents measurements of the Casimir force using a modified commercial accelerometer as well as a novel chip-scale system for Casimir energy detection using a thin-film

superconductor in a tunable nano-cavity.

Contents

1 Introduction **1**

1.1 The Casimir Effect 1

1.2 Casimir cavities and negative energy 3

1.3 Casimir Effect in MEMS 4

2 Theory **7**

2.1 Basic derivation of the Casimir Effect 7

2.2 Non-idealities in the Casimir force 12

2.2.1 Sphere-plate geometry and the Proximity Force Approximation 13

2.2.2 Lifshitz Theory and optical properties of materials 15

2.3 Casimir free energy 17

2.3.1 Type I superconductors 17

2.3.2 Shift in T_c 19

2.4 MEMS equations 21

2.4.1 Simple harmonic oscillator 21

2.4.2 Accelerometer basics 23

2.4.3 Non-linear oscillators and the Duffing equation 24

3 Casimir Force Measurement **30**

3.1 Project outline 30

3.2 MEMS accelerometers 30

3.3 Micro-gluing 31

3.3.1 Residual electrical potential 34

3.4 Apparatus and measurement 35
  3.4.1 Methods 37
  3.4.2 Measurement calibration 39
3.5 Results and discussion 39
  3.5.1 Casimir force measurement 39
  3.5.2 Discussion 42

4 Casimir Energy Detection **46**
4.1 Experimental concept 46
4.2 Device design and fabrication 50
  4.2.1 Target 50
  4.2.2 Sources 51
4.3 *In Situ* deposition 53
4.4 Plate actuation and sample measurements 57
4.5 Results and discussion 61
  4.5.1 Superconducting transition of quench condensed Pb film . . . 61
  4.5.2 Plate mechanics 63
  4.5.3 High frequency detection of T_c shift 65
  4.5.4 Discussion of results 67

5 Related MEMS Projects **72**
5.1 Micro-gluing enabled devices 72
  5.1.1 Gradient magnetometer 72
  5.1.2 Large angle micro-mirror 76
5.2 MEMS drive techniques 80
  5.2.1 Open loop driving for fast step-and-settle times 80
  5.2.2 Pulse width modulation for analog positioning 82

6 Conclusions and future outlook 87

6.1 Summary of Casimir force measurement with a commercial MEMS sensor 87

6.2 Summary of Casimir energy detection with superconductor in a tunable cavity . . . 88

6.3 Future outlook . . . 89

6.3.1 Searching for evidence of the Casimir energy . . . 89

6.3.2 The Casimir Effect in technology . . . 90

A Supplementary information for Casimir force measurement 92

A.1 Surface roughness measurements . . . 92

A.2 Plate height sensitivity . . . 93

A.3 Casimir force sensor temperature stability . . . 94

B Supplementary information for Casimir energy detection 95

B.1 Deposition characteristics of MEMS micro-sources . . . 95

B.2 Determining plate height . . . 96

B.2.1 Static actuation . . . 96

B.2.2 Post-experimental sample characterization and estimate of minimum gap size . . . 97

References 100

Curriculum Vitae 107

List of Figures

2·1 An intuitive picture of the Casimir Effect 8

2·2 Diagram of a simple Casimir cavity 8

2·3 The proximity force approximation for a sphere-plate geometry 13

2·4 Plot of critical field for a type I superconductor 18

2·5 Simulations of expected Casimir induced shifts in superconductor T_c . 20

2·6 Diagram of a simple mass spring damper system 21

2·7 Resonant response of a linear, under-damped MEMS system 23

2·8 Ring down of an under-damped harmonic oscillator 24

2·9 Working principle of an accelerometer 25

2·10 Linear and non-linear spring constants 26

2·11 Duffing oscillator resonant responses 28

3·1 Functionalizing a MEMS accelerometer to measure the Casimir force 32

3·2 Casimir force measurement apparatus and calibration 36

3·3 Measurement of the Casimir force using the modified accelerometer device 41

4·1 Schematic of the cryogenic die arrangement for low temperature Pb deposition and Casimir measurement 49

4·2 Nano-cavity fabrication process 50

4·3 To-scale diagrams and images of released nano-mechanical cavity for Casimir energy detection 52

4·4 Micro-sources for quench condensed Pb deposition 54

4·5 Depositing Pb from poly-silicon micro-sources 56
4·6 4-point resistance detection scheme 58
4·7 High frequency detection circuit 61
4·8 Superconducting transition of the quench condensed Pb film 62
4·9 Resonant response of movable Au plate 64
4·10 Quench condensed Pb film transition at different plate bias voltages . 65
4·11 High frequency detection of superconducting Pb film resistance and cavity size 66
4·12 A closer look at high frequency results 67

5·1 SEM image of an ADXL203 accelerometer re-purposed into a magnetometer 73
5·2 Assembly process for MEMS gradient magnetometer 74
5·3 MEMS gradient magnetometer performance 75
5·4 Magnetically driven micro-mirror 77
5·5 Steering the magnetically actuated micro-mirror 78
5·6 Magnetically driven micro-mirror range results 79
5·7 Simulations of under-damped system response to one-sided advanced drive pulses 81
5·8 Plot of a typical PWM signal 82
5·9 PWM enabled analog positioning of an accelerometer 84
5·10 Comparison of DC voltage control with PWM control in a parallel plate system 85

A·1 Casimir force surface roughness measurements 92
A·2 Plate height sensitivity 93
A·3 Casimir force sensor temperature stability 94

B·1 Characterizing the micro-source deposition with a quartz crystal resonator and PLL 96
B·2 White light interferometry data of a released Au plate at room temperature 97
B·3 AFM analysis of the cavity 98
B·4 Modeling the shape of the deformed Au plate 99

List of Abbreviations

AC	Alternating current
ADC	Analog to digital converter
AFM	Atomic force microscope
DC	Direct current
EBL	Electron beam lithography
LIA	Lock-in amplifier
MEMS	Micro-electromechanical systems
PFA	Proximity force approximation
PID	Proportional-integral-derivative
PLL	Phase-locked loop
PWM	Pulse width modulation
SEM	Scanning electron microscope
SHO	Simple harmonic oscillator
TIA	Transimpedance amplifier

Chapter 1

Introduction

1.1 The Casimir Effect

The Casimir Effect is named after the Dutch physicist Hendrik Casimir, who, along with with fellow researcher Dirk Polder, developed a theory for considering the forces between polarizable, neutral atoms. Building off of the London-van der Waals model, Casimir and Polder considered the effect of retardation on the energy of interaction between the atoms—that is, considering the interaction to occur no faster than the speed of light [Casimir and Polder, 1948]. The form of the expression they derived in 1947 was, in their own words, "very simple" and suggested for this reason it could be derived from "more elementary considerations." The same year, Casimir wrote a paper on this interaction between not just two atoms, but two neutral, conducting plates [Casimir, 1948]. The force of attraction he calculated to be:

$$F = \frac{\hbar c \pi^2 A}{240 d^4} \tag{1.1}$$

Where $\hbar$ is Planck's reduced constant, c is the speed of light, A is the area of the plates, and d is the separation.

According to most accounts, Casimir then had a conversation with Niels Bohr, who suggested this expression could be derived from considering "zero-point energy"—an importantly non-zero quantity of ground-state energy in the vacuum [Weisskopf, 1935]. According to Casimir, Bohr had an ingenious way of making "fairly precise qualitative statements about what quantum mechanics would predict without really doing much mathematics" [Kuhn et al., 1963]. What Bohr suggested was conceptually simpler than the retarded dispersion forces laid out by Polder and Casimir, but implied an even more extraordinary physical picture. Much like two ships in the water, Bohr pictured the two conducting surfaces as obstacles interacting with fluctuations of the electromagnetic vacuum. Just like the sea, spacetime also has random waves of various amplitudes and wavelengths constantly propagating and interfering with each other. This idea is sometimes referred to as a "quantum foam" [Wheeler, 1955]. In this ocean analogy, the presence of the two ships produces boundary conditions on the random water waves. Because of this, over time, waves that are longer in length than the separation of the ships will be damped out, leaving a subset of shorter wavelengths in between. Outside of the ships however, no such boundary conditions are present and the longer waves still exist. Due to this difference in total energy density, the ships will feel a slight force pushing them together, which is indeed a real effect reported by mariners [Boersma, 1996]. What Bohr was suggesting was that this same phenomenon occurs with conducting surfaces and virtual particles in the electromagnetic vacuum. Sure enough, if one considers the difference in energy between the perfectly conducting plates (which only allow a subset of electromagnetic waves in between them) compared to the energy of the empty vacuum, one ends up deriving the same result as Casimir. It is important to note that although the Casimir Effect has been observed, it is not necessarily proof that these virtual particles exist, as one can derive the same result using Casimir's original dispersion force interpretation [Jaffe, 2005].

1.2 Casimir cavities and negative energy

The implications of the virtual particle interpretation of the Casimir Effect are interesting to say the least. Essentially, the physical picture in this case is a region of space between the conducting plates which has an energy less than that of the completely empty vacuum surrounding it. In other words, a Casimir cavity can have arbitrarily negative energy density. The concept of "negative energy" is very abstract, and while it can be described theoretically, it is difficult to imagine manifested in the real world. That being said, on paper, negative energy can allow for some fantastical physical outcomes, such as faster than light travel. Stephen Hawking has posited that negative energy could allow for stabilized wormholes, a requirement for instantaneous transportation between two points in space [Hawking, 1992]. Another potential application of negative energy is the warp drive, or Alcubierre drive; a propulsion system in which spacetime is contracted in front of a spacecraft and expanded behind it, leading to superluminal travel [Alcubierre, 1994].

Whether or not Casimir cavities can make science fiction a reality, it is evident that an accurate measurement of what goes on energetically inside a Casimir cavity could be a key to better understanding the physics of the vacuum. In fact, for the last few decades, one of the greatest unsolved mysteries in physics has been determining the magnitude of the Cosmological Constant–a value which describes the energy density of the vacuum. Current quantum field theory arguments estimate this constant to be up to 120 orders of magnitude larger than what is observed, leading to some dubbing it "the vacuum catasrophe" [Adler et al., 1995].

One experiment proposed to investigate the energy inside a Casimir cavity involves using a superconductor. Superconductivity is a fascinating state of matter that some materials reach when cooled below a certain critical temperature. In this superconducting phase, electrons can move through the crystal lattice of the material with exactly zero energy dissipation. This transition happens very abruptly such that the electrical and optical properties of the material can change by orders of magnitude over just a few tens of milli-Kelvin change in temperature. This sharp transition can be used to probe small changes in the environment, and, as discussed further on in this thesis, perhaps changes in the Casimir energy.

1.3 Casimir Effect in MEMS

Other than confirming or denying theory, Casimir Effect research has practical applications in engineering at the nanoscale. Micro-electromechanical systems (MEMS) are a wide class of devices which couple mechanical motion and electrostatics at micro (and also nano) scales. These devices either transduce a physical change in the environment into a measurable signal or, inversely, turn an input electrical signal into a physical change of the device and/or its surroundings (usually mechanical actuation of some kind). According to equation 1.1, the Casimir force between two plates of area $100\,\mu\mathrm{m}^2$ at a distance of $100\,\mathrm{nm}$ is $13\,\mathrm{nN}$. Considering typical spring constants in MEMS of roughly $1\,\mathrm{N\,m^{-1}}$, that corresponds to $13\,\mathrm{nm}$ of displacement. These types of forces become relevant with closely spaced objects and therefore understanding the role of this effect is necessary in MEMS design.

While engineers may be interested in avoiding the Casimir force in their designs, experimental physicists typically use MEMS for careful measurements of the Casimir force. Because of their mechanical stability and robustness, MEMS sensors can measure extremely small signals either electrically or optically. For example, an atomic force microscope (AFM) makes use of a MEMS cantilever with a nanoscale tip to interact with surfaces over a very small area. By measuring the deflection of a laser beam off the back of the cantilever, one can resolve nanometer displacements and atomic scale forces. Much experimental work has made use of AFM cantilevers for Casimir force measurements [Mohideen and Roy, 1998,Roy and Mohideen, 1999,Van Zwol and Palasantzas, 2010, Garrett et al., 2018]. Other work using MEMS has made use of torsional resonators [Chan et al., 2001a,Chan et al., 2001b,Decca et al., 2003]. MEMS devices that can integrate both Casimir surfaces onto a single chip [Zou et al., 2013] are less prone to low-frequency noise and thermal drift due to smaller components and higher mechanical resonant modes, but come at the cost of reduced interaction area and limited separation ranges.

But what if the Casimir Effect could be leveraged as a practical, controllable engineering tool within a MEMS system? Electrostatic MEMS sensors use a changing capacitance or electrostatic signal of some kind as a measurement, which will scale as one over separation or one over separation squared. We have seen that the Casimir force scales as one over separation to the fourth power. This extraordinary scaling with distance could be used to enhance the sensitivity of MEMS. For example, it has been suggested that a MEMS oscillator parametrically driven by the Casimir force would exhibit a gain that scales as one over the Casimir cavity size to the fifth power or as applied direct current (DC) voltage to the tenth power [Imboden et al., 2014b]. In addition to providing a means of investigating the Casimir Effect itself, a system such as this could be useful for temperature sensing, alternate current (AC) voltage measurements, low-impedance current measurements, or probing any measurand which could be coupled into a physical change in size of the Casimir cavity.

The MEMS industry has been incredibly successful mainly due the parallel nature of device fabrication. Most MEMS are built using the same processes used in the computer chip industry, so they benefit from the same technological improvements in cost per device and minimum feature size that has been driving the semiconductor industry over the last few decades [Bohr and Young, 2017]. As a result, MEMS sensors can be built reliably, cheaply and in large numbers. This rapid advancement of commercial MEMS has resulted in devices with truly remarkable performance. Current state-of-the-art low g MEMS accelerometers are capable of sensing sub mg accelerations with noise densities of around 0.1 mg/Hz$^{1/2}$ or less [Tez et al., 2015, Sabato et al., 2017, Analog Devices Data Sheet, 2018]. Integrating the Casimir effect into mature, high performance MEMS systems could result in a class of novel quantum-enabled sensing devices.

Chapter 2

Theory

2.1 Basic derivation of the Casimir Effect

One of the many interesting and counter-intuitive results of quantum theory is that the ground-state energy, or “zero-point energy” of an empty electromagnetic field is not zero, but rather [Milonni, 1994]:

$$\langle E \rangle = \frac{1}{2} \sum_{k} \hbar \omega_k \tag{2.1}$$

As seen by the expression in equation 2.1, this energy is an infinite sum of independent harmonic oscillators with frequency ω_k. The Casimir force can be derived by considering the difference between the ground-state energy of the electromagnetic field and the ground-state energy of only the field inside the cavity. A good illustration as to why this difference is not simply zero can be seen in figure 2·1. In this schematic, we see there is a series of standing waves inside the cavity due the boundary conditions imposed by the perfectly conducting plates (recall that Maxwell’s equations state that the transverse electric field must equal zero on the surface of a conductor). Outside of the cavity, however, a continuum of modes are able to exist. This inherent difference in energy density is what causes a net pressure, pushing the two plates together.

For the following derivation (adapted from [Szulc, 2012]), we consider a 3D box of side length L and an additional plate of dimension L × L at a distance R (R $\ll$ L)

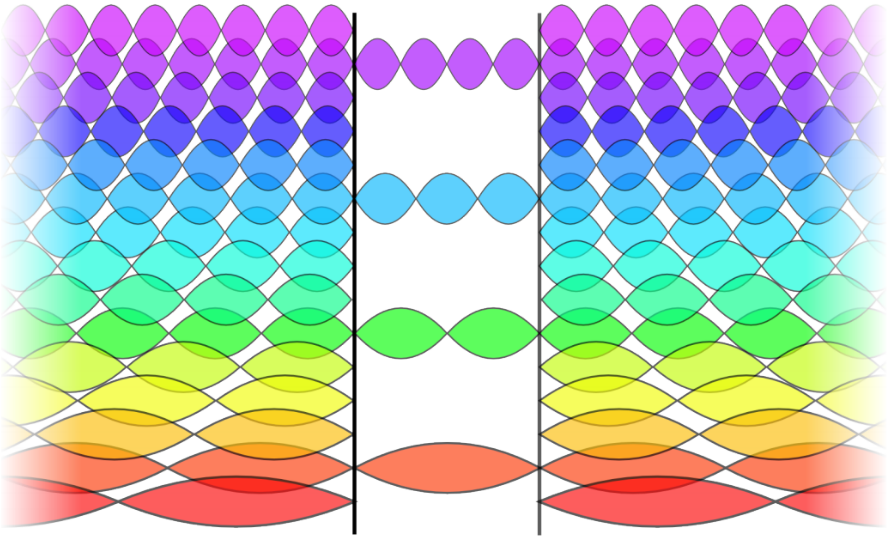

Figure 2·1: An intuitive picture of the Casimir Effect [Kingsbury, 2009]

.

from the XY plane:

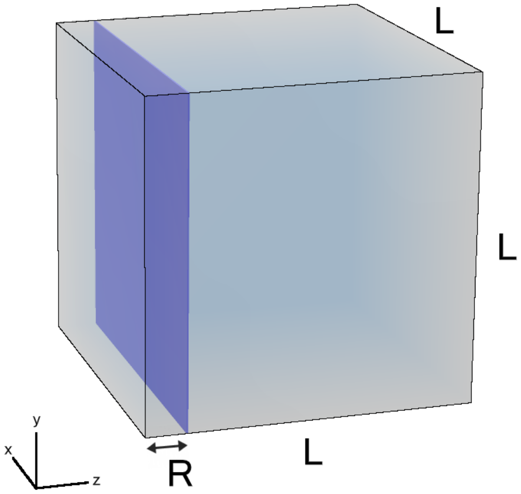

Figure 2·2: Diagram of a simple Casimir cavity. The presence of the inner wall (shown in purple) changes the total energy inside the cube.

We are interested in determining the difference of the zero-point energies of the box without the plate, and the cube with the plate, that is:

$$\Delta E = E_R + E_{L-R} - E_L \tag{2.2}$$

Where E_R denotes the energy of the region bounded between the XY axis and the plate, E_L denotes the energy of the whole box, and E_{L-R} denotes the energy of the region in the box, but outside of the plate. We assume all surfaces are perfect conductors. Because of the boundary conditions imposed by the walls, the solution of the wave equation is a series of standing waves whose wavevectors, $k = k_x\hat{x} + k_y\hat{y} + k_z\hat{z}$ are given by:

$$k_x = \frac{n_x \pi}{L}, \qquad k_y = \frac{n_y \pi}{L}, \qquad k_z = \frac{n_z \pi}{R} \tag{2.3}$$

Where n_x, n_y, n_z are positive integers. As introduced in equation 2.1, in the ground state, each of these modes contributes an energy of $\hbar\omega/2$. Recalling that $\omega = ck$, we can therefore express the total energy in any region of the box as:

$$\langle E \rangle = \frac{1}{2}\hbar c \sum \sqrt{k_x^2 + k_y^2 + k_z^2} \tag{2.4}$$

To solve equation 2.2, we want to determine equation 2.4 in each region. Because R ≪ L, the large regions can be approximated as integrals:

$$E_L = \frac{2L^3}{\pi^3} \int\int\int_0^\infty \frac{1}{2}\hbar c \sqrt{k_x^2 + k_y^2 + k_z^2} dk_x dk_y dk_z \tag{2.5}$$

$$E_{L-R} = \frac{2L^2(L-R)}{\pi^3} \int\int\int_0^\infty \frac{1}{2}\hbar c \sqrt{k_x^2 + k_y^2 + k_z^2} dk_x dk_y dk_z \tag{2.6}$$

$$E_R = \sum_{n_z=0}^{\infty} 2\theta_{n_z} \frac{L^2}{\pi^2} \int\int_0^\infty \frac{1}{2}\hbar c \sqrt{k_x^2 + k_y^2 + \left(\frac{n_z \pi}{R}\right)^2} dk_x dk_y \tag{2.7}$$

In the integrals, a change of variables has been made in order to integrate over k_x, k_y, k_z rather than n_x, n_y, n_z. Note that the small region in equation 2.7 still retains the summation in the Z direction. The variable $\theta_{n_z} = 1/2$ for $n_z = 0$ and $\theta_{n_z} = 1$ for $n_z > 0$. This accounts for the number of polarization states of k (i.e. there exist two independent modes for each positive integer n_z).

Looking at these equations, it is clear that they diverge to infinity. In reality however, a conductor should not reflect up to arbitrarily high frequencies. We can use the concept of the "plasma frequency" as a physical argument for this upper limit. The plasma frequency is the cut-off at which free electrons in the conductor are no longer able to keep up with the incident optical field. Above this frequency, light will penetrate the conductor and not be reflected [Kittel, 1953]. From the Drude model for metals, the plasma frequency, ω_p, is can be written as:

$$\omega_p = \sqrt{\frac{Ne^2}{\varepsilon_0 m}} \tag{2.8}$$

Where N is the number density of electrons, e is the electron charge, and m is the electron mass. For this derivation, the expression for the plasma frequency is not important, however it is worth mentioning to justify why we expect an upper limit in these integrations. For simplicity, we multiply everything by a cut-off function f with the following properties:

$$f(k/k_p) \to 1, \text{ for } k \ll k_p \tag{2.9}$$

$$f(k/k_p) \to 0, \text{ for } k \gg k_p \tag{2.10}$$

Here, $k = \sqrt{k_x^2 + k_y^2 + k_z^2}$ is the modulus of the wave vector, and k_c is just the modulus of the wave vector corresponding to the plasma frequency (from $w_p = ck_p$).

Substituting equations 2.5, 2.5, and 2.5 into equation 2.2, we get:

$$\Delta E = \frac{\hbar c L^2}{\pi^2}\left[\sum_{n_z=0}^{\infty} \theta_{n_z} g\left(\frac{n_z \pi}{R}\right) - \frac{R}{\pi}\int_0^{\infty} g(k_z) dk_z\right] \tag{2.11}$$

Where we have defined the function g to simplify things:

$$g(\xi) = \int\int_0^{\infty} f\left(\frac{k}{k_p}\right)\sqrt{k_x^2 + k_y^2 + \xi^2} dk_x dk_y \tag{2.12}$$

Switching to cylindrical coordinates further simplifies the expression for $g(k_z)$. Here, $\kappa = \sqrt{k_x^2 + k_y^2}$ is the inverse of the radial coordinate, so $g(k_z)$ becomes:

$$g(k_z) = \frac{\pi}{2}\int_0^{\infty} \sqrt{\kappa^2 + k_z^2} f\left(\frac{\sqrt{\kappa^2 + k_z^2}}{k_p}\right) \kappa d\kappa \tag{2.13}$$

The angular coordinate has been integrated from 0 to $\pi/2$, resulting in the leading factor of equation 2.13. Now, a variable α is introduced where $\kappa = \alpha\pi/R$. Therefore, $\kappa d\kappa$ becomes $(\pi/R)\alpha d\alpha$. We also recall that $k_z = n_z\pi/R$. Now we can write:

$$g(n_z) = \frac{\pi}{2}\int_0^{\infty} \sqrt{\frac{\pi^2}{R^2}(n_z^2 + \alpha^2)} f\left(\frac{\sqrt{\frac{\pi^2}{R^2}(n_z^2 + \alpha^2)}}{k_p}\right) \frac{\pi}{R}\alpha d\alpha \tag{2.14}$$

which simplifies to

$$g(n_z) = \frac{\pi^3}{2R^2}\int_0^{\infty} \sqrt{n_z^2 + \alpha^2} f\left(\frac{\pi\sqrt{n_z^2 + \alpha^2}}{R k_p}\right) \alpha d\alpha \tag{2.15}$$

One more change of variables to $\omega = n_z^2 + \alpha^2, d\omega = 2\alpha d\alpha$ gives:

$$g(n_z) = \frac{\pi^3}{4R^2} \int_{n_z^2}^{\infty} \sqrt{\omega} f\left(\frac{\pi\sqrt{\omega}}{Rk_p}\right) d\omega \tag{2.16}$$

Defining the integral in equation 2.16 as $F(n_z)$, we can re-write equation 2.11 as:

$$\Delta E = \frac{\pi^2 \hbar c L^2}{4R^3} \left[\sum_{n_z=0}^{\infty} \theta_{n_z} F(n_z) - \int_0^{\infty} F(n_z) dn_z \right] \tag{2.17}$$

This term in square brackets is called the "Euler-Maclaurin formula" [Stoer and Bulirsch, 1993] and can be approximated as:

$$\sum_{n=0}^{\infty} \theta_n F(n) - \int_0^{\infty} F(n)dn = -\frac{1}{6 \times 2!} F'(0) + \frac{1}{30 \times 4!} F'''(0) - ... \tag{2.18}$$

Evaluating these terms, $F'(0) = 0$ and $F'''(0) = -4$. Thus, equation 2.18 is approximately equal to $-4/(30 \times 4!) = -1/180$. Adding this into equation 2.17 gives:

$$\Delta E = -\frac{\hbar c \pi^2 L^2}{720 R^3} \tag{2.19}$$

Here, L^2 is just equal to the area, A, and the force due to this energy is $-\frac{d\Delta E}{dR}$ which is equal to

$$F_{\text{cas}} = \frac{\hbar c \pi^2 A}{240 R^4} \tag{2.20}$$

as introduced in section 1.1.

2.2 Non-idealities in the Casimir force

Equation 2.20 is only for ideal conditions: absolute zero temperature and perfectly flat, smooth infinitely conducting surfaces. Experimentally, however, these conditions are never realized. First of all, our Casimir force experiment is done at room temperature. Also, the metals used (Au and Ag) have different plasma frequencies and thus an adjustment of the calculated Casimir force must be made. Finally, the two surfaces likely will not be perfectly smooth and planar. Surface roughness is always present on any evaporated metal surface and will strongly affect surface forces at separations comparable to the scale of that roughness. Also, aligning two planes to be perfectly parallel is quite challenging. A much simpler set-up involves bringing one planar and one spherical surface into close separation. In this arrangement, the orientation of the plane relative to the sphere is unimportant, as the interaction area will be the same at any given separation, d. Each of these non-idealities will be expanded upon in the following sections.

2.2.1 Sphere-plate geometry and the Proximity Force Approximation

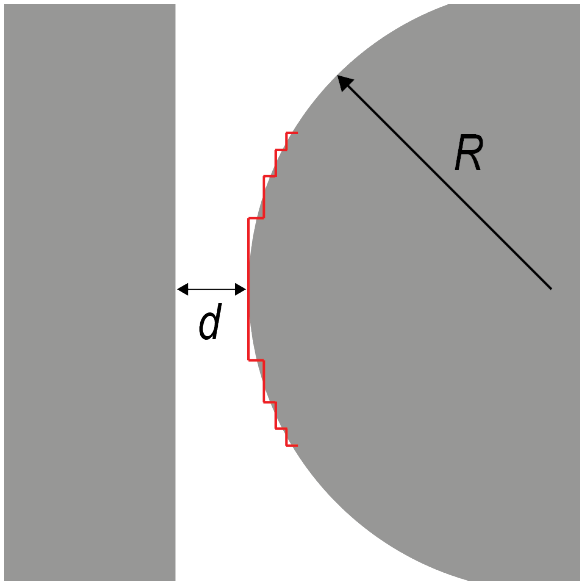

Figure 2·3: The proximity force approximation for a sphere-plate geometry.

To calculate the Casimir Energy (and force) in a sphere-plate configuration, the spherical surface can be approximated as many small parallel rings at different separations from the plate. This is known as the Derjaguin Approximation or the Proximity Force Approximation (PFA) and is a commonly used method in much surface energy and tribology work [Derjaguin, 1934]. The PFA assumes a geometry like that depicted in figure 2·3 in which the spherical surface is broken up into many small parallel surfaces. In the PFA, it is assumed that the separation, d is much less than the radius of curvature of the surfaces (R). In this limit, the interaction energy between the non-planar surfaces is approximated by summing the energetic contribution per unit area from each set of parallel surfaces and then integrated over the area, as expressed in equation 2.21.

$$E = \int\limits_S W(d)\mathrm{d}A \tag{2.21}$$

Here, W is the interaction energy per unit area. It can be shown [Israelachvili, 2011] that for two spherical surfaces with respective radii R_1 and R_2, which interact with any force law that scales with distance, equation 2.21 leads to the an approximated force:

$$F(d)_{\text{sphere-sphere}} = 2\pi \frac{R_1 R_2}{R_1 + R_2} W(d) \tag{2.22}$$

If one of these radii of curvature is infinite (as in the case of a plane), equation 2.22 becomes simply:

$$F(d)_{\text{sphere-plate}} = 2\pi R W(d) \tag{2.23}$$

The energy per unit area is just equation 2.19 without the area term, so the Casimir force for a sphere-plate geometry (with $d \ll R$) is then:

$$F_{\mathrm{C}}^{0}(d) = \frac{\hbar c \pi^3 R}{360 d^3} \tag{2.24}$$

2.2.2 Lifshitz Theory and optical properties of materials

As mentioned in the introductory section 1.1, Casimir and Polder's first theoretical findings arose from considering the effects of retardation on van der Waals forces. Casimir then used this interpretation to derive the well-known Casimir force equation between two conducting surfaces. Some years later, Evgeny Lifshitz came up with a generalized theory of macroscopic forces which arise between solid bodies due to pairs of charges in each material [Lifshitz, 1956]. Unlike the previous London-van der Waals theory, however, Lifshitz considered the effect of the neighboring molecules in each material. For example, a conducting material which has a lot of free electrons may screen individual point charges more than an insulating material. In the framework of the Lifshitz Theory, the surface interactions which arise from fluctuations of molecules are lumped into macroscopic properties of the materials: the dielectric permittivity and dynamic atomic polarizability. It turns out that by using the Lifshitz Theory in the limit where the two bodies are separated by a distance that is large compared to the absorption wavelength of the material, the Casimir force can be reproduced [Klimchitskaya et al., 2009].

There is much theoretical work that has been done developing realistic models for the Casimir energy and force based off of the Lifshitz Theory [Gies and Klingmüller, 2006, Bulgac et al., 2006, Emig et al., 2007, Rahi et al., 2009, Klimchitskaya et al., 2009]. In the project discussed in chapter 3, a relatively simple model is considered [Geyer et al., 2002] which accounts for realistic physical effects such as non-zero temperature and the finite conductivity of both metallic surfaces (in our case, Au and Ag). In this model, shown in equation 2.25, a perturbation expansion in powers of the relative penetration depths of electromagnetic oscillations into each metal (using a plasma model) provides a corrected equation for the Casimir force given as:

$$F_C^P(d) = F_C^0 \left[1 + \frac{45\zeta(3)}{\pi^3 t^3} - \frac{1}{t^4} - 2\frac{\delta}{d}\left(2 - \frac{45\zeta(3)}{\pi^3 t^3} + \frac{2}{t^4}\right)\right.$$

$$\left. + \frac{75}{5}\frac{\delta^2}{d^2} - \frac{320}{7}\frac{\delta^3}{d^3}\left(1 - \frac{2\pi^2}{105}(1-3\kappa)\right) + \frac{400}{3}\frac{\delta^4}{d^4}\left(1 - \frac{326\pi^2}{3675}(1-3\kappa)\right)\right] \quad (2.25)$$

Here, F_C^0 is the Casimir force for a sphere-plate geometry given by equation 2.24, ζ is the Reimann Zeta function, t is a dimensionless temperature parameter given by $t = (\hbar c)(2k_B T d)^{-1}$, and δ and κ are optical parameters given by:

$$\delta \equiv \frac{\delta_{\mathrm{Au}} + \delta_{\mathrm{Ag}}}{2} \quad (2.26)$$

$$\kappa \equiv \frac{\delta_{\mathrm{Au}} + \delta_{\mathrm{Ag}}}{(\delta_{\mathrm{Au}} + \delta_{\mathrm{Ag}})^2} \quad (2.27)$$

Where δ_{Au} and δ_{Ag} are the effective penetration depths of the electromagnetic oscillations into each metal film given by $\hbar c/\omega_p$ in which we have used $\omega_p = 9\,\mathrm{eV}$ for Au and $\omega_p = 8.6\,\mathrm{eV}$ for Ag [Rioux et al., 2014]. Equation 2.27 is a limiting case of this theory in which $1/t \ll 1$, which is a valid approximation at our operating temperature ($T = 301.15\,\mathrm{K}$) and $d < 1\,\mu\mathrm{m}$.

Finally, a second order correction for surface roughness is included [Mohideen and Roy, 1998, Maradudin and Mazur, 1980]:

$$F_C^R(d) = F_C^P(d)\left[1 + 6\left(\frac{A_R}{d}\right)^2\right] \quad (2.28)$$

Where A_R is the stochastic RMS roughness amplitude of both surfaces. In the experiment discussed in chapter 3, the Au plate and Ag spherical surfaces are characterized with AFM. The surface roughness values were found to be $A_{\mathrm{R,plate}} = 2\,\mathrm{nm}$ and $A_{\mathrm{R,sphere}} = 8\,\mathrm{nm}$ (appendix A.1). The total RMS roughness used in equation 2.28

is $A_{\mathrm{R}} = (A^2_{\mathrm{R,sphere}} + A^2_{\mathrm{R,plate}})^{1/2} = 8.25\,\mathrm{nm}$. Equation 2.28 is the final corrected model used to compare data with the ideal case (equation 2.24).

2.3 Casimir free energy

As discussed in section 1.2, a method of detecting the Casimir energy is by looking at the transition of a superconducting material inside a Casimir cavity. It is theorized that the Casimir energy should modify the condensation energy of the material, shifting the critical field or temperature at which it becomes superconducting [Bimonte et al., 2005c]. The physical mechanism behind this argument has to do with the abrupt change in the optical properties of a superconductor as it transitions. Because the Casimir energy depends on the reflectivity of the surfaces, when the metal becomes superconducting, there should be a sharp change in the Casimir energy (and force). Conversely, a variation of the size of the Casimir cavity would theoretically change the free energy of the system, thus altering the critical field.

2.3.1 Type I superconductors

Superconductivity is a phase that occurs in certain materials at low temperatures (typically < 10 K). Physically speaking, a state of zero resistivity is attained in the material, where currents can flow with no loss of energy. The Nobel Prize in Physics was awarded in 1972 to John Bardeen, Leon Cooper, and John Robert Schrieffer whose eponymous “BCS Theory” explained the physical mechanism for this effect as a phonon mediated pairing of electrons within the material. Alone, only two electrons (Fermions) can occupy the same state, however in these pairs, they act like Bosons, and a large number of pairs can all be in the same quantum state. This is what occurs in a superconductor and what allows for electron probability currents to flow

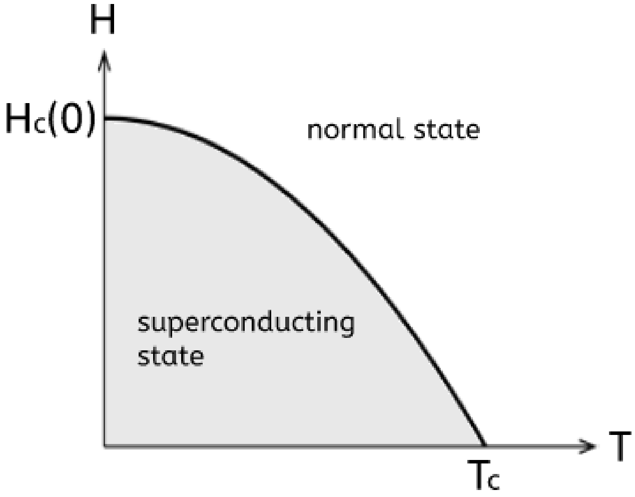

Figure 2·4: Plot of critical field for a type I superconductor.

throughout the lattice with exactly zero energy loss [Kittel, 1953].

As a result of these dissipationless currents, all external magnetic fields are expelled from the body of the superconductor (this is known as the Meissner effect). If the external field is large enough, however, the superconducting phase breaks down and the material goes back to its normal properties (in type II superconductors, the material first goes through an intermediate superconducting phase called the vortex state, but here we will only focus on type I). The field strength at which this occurs is known as the critical field (H_c) and it is a function of temperature, with a parabolic relation given by $H_c(T) = H_0\left(1 - T/T_c\right)^2$ and plotted in figure 2·4.

For a type I superconducting film, we can write the condensation energy ($\varepsilon_{\text{cond}}$) which is equal to the difference in free energy between the normal state and that of condensed state [Poole, 2000]:

$$\varepsilon_{\text{cond}} = \frac{V}{8\pi}\left(\frac{H_c(T)}{\rho}\right)^2 \tag{2.29}$$

Here, V is volume of the sample, ρ is a coefficient which accounts for thin film effects, and H_c is the critical magnetic field which destroys superconductivity. According to Bimonte et al., when this film now makes up one half of a Casimir cavity (the other half being a non-SC metal), the condensation energy is shifted by another term, $\Delta E_{\text{Casimir}}$, which is the difference in the Casimir free energy of the cavity in the normal state (E^n_{Casimir}) and the superconducting state (E^s_{Casimir}) [Bimonte et al., 2005c]:

$$\Delta E_{\text{Casimir}} = E^n_{\text{Casimir}} - E^s_{\text{Casimir}} \tag{2.30}$$

We now have an expression which relates the critical field in a cavity (a measurable quantity) with a shift in Casimir energy:

$$\varepsilon_{\text{cond}} + \Delta E_{\text{Casimir}} = \frac{V}{8\pi}\left(\frac{H_C^{\text{cav}}(T)}{\rho}\right)^2 \tag{2.31}$$

Although this equation conveys the basic idea behind this detection scheme, it is experimentally more straightforward to measure a shift in the critical temperature, T_c, instead of the critical field. Theoretically however, as explained further on, the expected shift is less easy to predict. In the experimental work presented, a change in T_c is measured, although future work may require looking at both applied fields and changing temperatures.

2.3.2 Shift in T_c

Conceptually, the presence of the superconductor results in a positive $\Delta E_{\text{Casimir}}$ for the reason that optically a superconductor more closely resembles an ideal mirror than that same material would in its normal state. Some calculations from [Bimonte

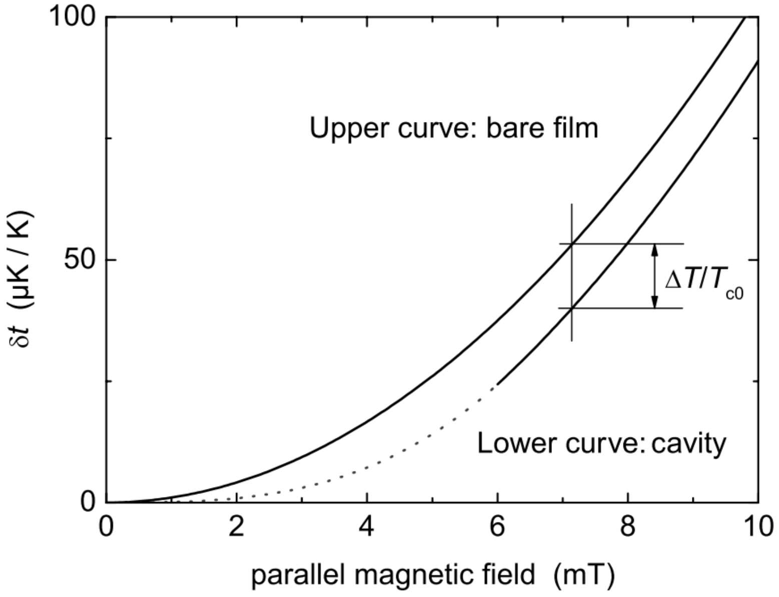

Figure 2·5: Simulation of the expected shift of the T_c vs. applied field curve for a thin Al film of thickness 14 nm. Upper curve is the Al film alone, and the lower curve is for a cavity consisting of the Al film separated from a 100 nm thick Au layer by 6 nm. From [Bimonte et al., 2008].

et al., 2008] indicate what one might expect in terms of the magnitude of this shift, plotted in figure 2·5.

In figure 2·5, the y axis is a reduced value, δt, which is equal to $1 - T/T_c^0$, T being the temperature and T_c^0 being the critical temperature at zero-field. These two curves show a couple of things: 1) the order of magnitude shift of critical temperature is tens of µK for moderate applied fields and 2) in the low-field limit, there currently is no theory for what the shift in T_c should be (indicated by the dashed line in the lower curve of figure 2·5). Bimonte et al. explain that in this regime, the Casimir free energy is on the order of the condensation energy, and the perturbative approach used in these calculations is no longer valid [Bimonte et al., 2008]. Despite this lack of theory, the magnitude of the effect should be larger when this is the case–i.e., the larger the Casimir energy term is compared to the condensation energy, the larger a shift in critical field or critical temperature we should expect. This can be seen by using equations 2.29 and 2.31 to express a relative change in critical field, $\delta H_c/H_c$:

$$\frac{\delta H_c}{H_c} = \frac{H_c^{\text{cav}} - H_c}{H_c} \tag{2.32}$$

$$\frac{\delta H_c}{H_c} = \sqrt{\frac{\Delta E_{\text{Casimir}}}{\varepsilon_{\text{cond}}} + 1} - 1 \tag{2.33}$$

We can see from equation 2.33 that the larger the Casimir free energy is compared to the condensation energy, the larger the expected shift.

2.4 MEMS equations

2.4.1 Simple harmonic oscillator

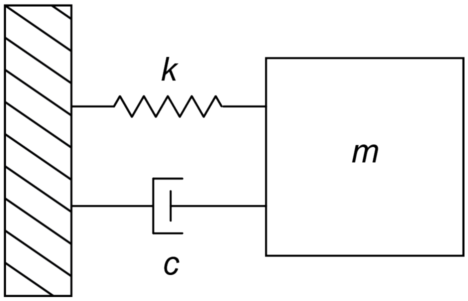

Figure 2·6: Diagram of a simple mass spring damper system.

The simple harmonic oscillator, or forced-damped harmonic oscillator, is an invaluable model for understanding many MEMS systems (not to mention countless other physical systems!). The classic picture of this model is a mass connected to a spring and a damper, as pictured in figure 2·6. The spring follows Hooke's law, such that it provides a restoring force proportional to its displacement from equilibrium by a constant, k. The damper also provides a force opposite to the motion of the mass, and linearly proportional to the velocity by constant, c. We can then write the equation of motion as:

$$F_{ext}(t) = m\ddot{x} + c\dot{x} + kx \tag{2.34}$$

Where $\dot{x}$ is the derivative of the position with respect to time and $\ddot{x}$ is the second derivative of the position with respect to time. It is convenient to divide through by the mass and re-express equation 2.34 as:

$$G(t) = \ddot{x} + 2\lambda\dot{x} + \omega_0^2 x \tag{2.35}$$

Where $G(t) = \frac{F_{ext}}{m}$, $\lambda = \frac{c}{2m}$, and $\omega_0 = \sqrt{\frac{k}{m}}$. Solving this differential equation is not important here, however a few points will be made. A key system parameter is ω_0, which, in units of time^{-1}, is the "natural frequency" of the system. All of the MEMS systems discussed in this dissertation are "under-damped"–that is, the damping force ($c\dot{x}$) is small compared to the inertial force ($m\ddot{x}$). In under-damped systems, the natural frequency is essentially the frequency at which the system will oscillate with the largest amplitude. One way of visualizing this is by driving $G(t) = G_0 \cos(2\pi f t)$ at a range of frequencies and plotting the amplitude of the resulting oscillations, $|x(t)|$. Some real data for this type of system is plotted in figure 2·7. In this mini-experiment, we drive a poly-silicon mass and spring system in air (so moderate damping is present) across its natural resonance frequency of $\sim 3\,\mathrm{kHz}$. For driving frequencies close to this value, the amplitude is larger by about 3X. Another way that the natural frequency shows up in experiment is in the response to a step input.

If one were to suddenly apply a non-zero force to the mass shown in figure 2·6, the mass would move towards a new equilibrium position, overshoot it, come back undershoot it, and so on until it finally settled at this new equilibrium point. This motion is referred to as a "step-and-settle" response and it seen in every under-damped system. The frequency at which it oscillates about the equilibrium point will be very close to the natural frequency (in the limit of zero damping, it will be

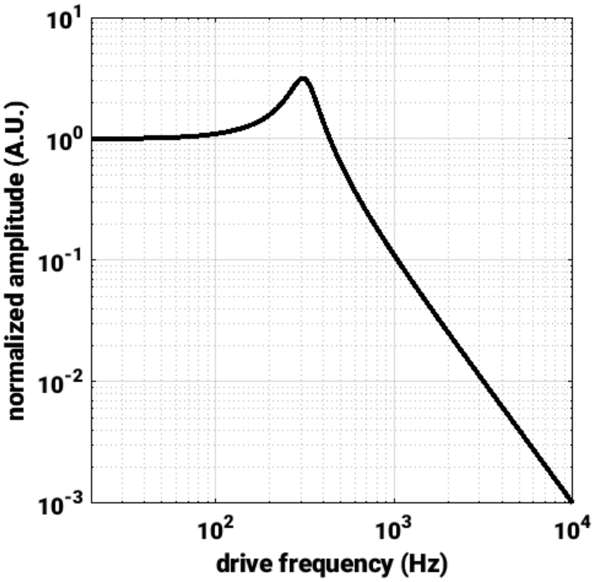

Figure 2·7: Resonant response of a linear, under-damped MEMS system. The natural frequency of this system is around 3 kHz.

equal to the natural frequency) and the time it takes to ring down to $1/e$ of its initial amplitude is equal to $1/\lambda$. Shown in figure 2·8 is the response of an oscillator whose equilibrium point is $x = 0$ but starts at some point $x(t = 0) \neq 0$. The transient response (exponential decay) in this case is identical to that of a step-and-settle response.

2.4.2 Accelerometer basics

The operating principle of a MEMS accelerometer is simple, and closely related to that of the simple harmonic oscillator shown previously. In an accelerometer, a moveable structure (known as the proof-mass) forms a capacitor with a fixed structure (these are both typically doped poly-silicon). The proof-mass is tethered by some compliant springs to the substrate. Under an applied acceleration, the proof-mass will move, changing the capacitance, which is sensed electrically with on-board integrated circuitry. This type of device is shown in figure 2·9. For some applications, like tilt

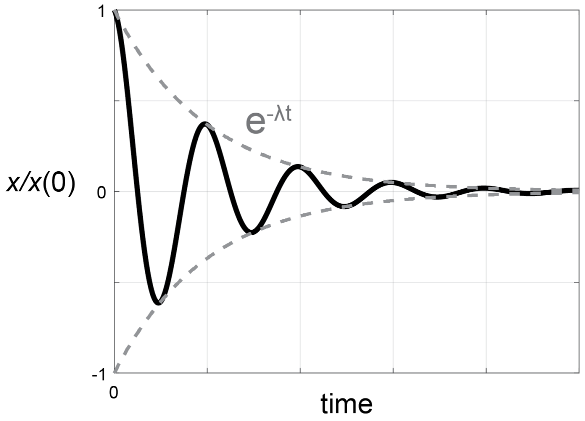

Figure 2·8: Ring down of an under-damped harmonic oscillator. The decay envelope is equal to $e^{-\lambda t}$.

sensing, we are not concerned with the dynamic response of the system–some applied tilt will apply a gravitational force to the proof-mass and it will move to a new position, and the capacitance reading will be different. Other applications, however, like vibration sensing require the proof-mass to be able to move along with higher frequency accelerations applied to the device. In this case, the proof-mass will be able to resolve these high frequencies up to its natural frequency. Beyond this frequency, as we can see in figure 2·7, the amplitude quickly drops off and the sensor can no longer respond.

2.4.3 Non-linear oscillators and the Duffing equation

Equation 2.34, though very helpful in understanding myriad physical phenomena, is a greatly simplified model and may not capture all that may be happening in a real system. One assumption in this model, is that the spring constant, k, is linear with displacement, x. This linearity, however, often holds only for small displacements. What is often observed in real systems is that the restoring spring force may actually vary non-linearly for large displacements due to various reasons [Elshurafa et al., 2011, Liu, 2012]. This is known as "spring hardening" or "spring softening" which is

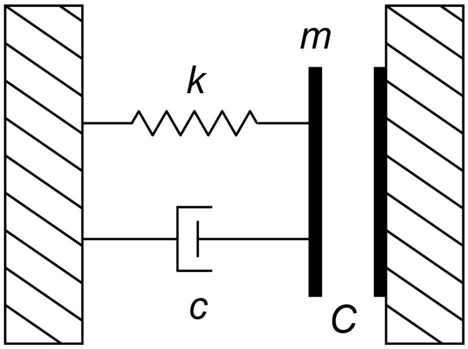

Figure 2·9: Working principle of an accelerometer. At its most basic form, a MEMS accelerometer is just a capacitor on a spring. The proof-mass (of mass m) will move under an applied acceleration. It will come to equilibrium when the external force is balanced by an equal and opposite force due to the spring (spring constant k). The changing position is sensed electrically by measuring the capacitance, C. When driven dynamically, a damping force proportional to the velocity by c is also present.

shown in the plot of restoring force vs. displacement in figure 2·10.

A system in which spring softening can occur is electrostatically driven MEMS. In a device like the one shown in figure 2·9, the mass can be driven with a voltage applied between the two plates. In this case, the mass will feel an electrostatic force that is proportional to V^2/d where d is the separation between the plates. Therefore, as the amplitude of oscillation gets larger, the movable plate will get closer and closer to the fixed plate, increasing the electrostatic force. This will result in a non-linear and asymmetric effective spring constant. Because of this increased pulling force on one side of the cycle, the mass will feel as if the restoring spring is getting softer on that side. This spring non-linearity is shown qualitatively by the thin dashed line in figure 2·10.

The spring hardening effect often occurs due to geometry. Many MEMS designs involve resonators that are moving transverse to their orientation (imagine a cantilever fixed on one end like a diving board or a doubly clamped beam). As the

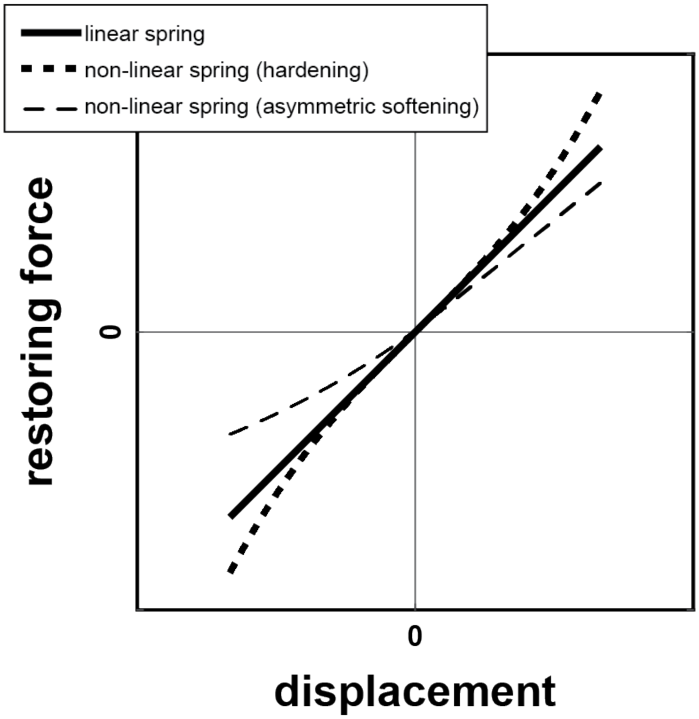

Figure 2·10: Linear and non-linear spring constants. The solid line is a linear spring with an unchanging slope. The thick dotted line depicts spring hardening behavior, symmetric about equilibrium. The thin dashed line shows what spring softening behavior due to a one-sided electrostatic driving force may look like.

beam deflects downwards in the transverse direction, an axial strain along its length is also introduced, like a guitar string being tightened. This stiffens the beam and will increase the spring constant and also the resonant frequency [Liu, 2012]. Spring hardening of this nature will occur in a symmetric manner about zero displacement, resulting in a spring constant profile like that shown in the thick dotted line in figure 2·10.

The Duffing oscillator

A straightforward way to capture non-linear dynamics due to changing spring constants is to modify the equation of motion (equation 2.34). Instead of a linear kx term, the Duffing model includes both a linear term as well as a cubic term:

$$F_{ext}(t) = m\ddot{x} + c\dot{x} + k_0 x + k_1 x^3 \tag{2.36}$$

A positive k_1 term is meant to approximate deviations from the typical linear slope of $k = \frac{\mathrm{d}F}{\mathrm{d}x}$ at large x like those seen in geometry induced spring hardening. A negative value of k_1 would then result in spring softening (but unlike the electrostatic spring softening described above, this would be symmetric). Solving this differential equation is not important, but we can get a good idea of the dynamic behavior of this model by examining some plots in figure 2·11.

The plots in figure 2·11 are meant to qualitatively show how the Duffing model behaves for a given input parameter. These plots are produced by solving equation 2.36 numerically with a Euler approximation method. The parameters used in this model are: $F_{\mathrm{ext}} = A_0 \cos(2\pi f t)$ where $A_0 = 5/8$, $m = 1$, $c = 0.01$, $k_0 = 4\pi^2$, and k_1 is varied between -25 and 25 (figure 2·11 on the left side). Note that for $k_1 = 0$, we

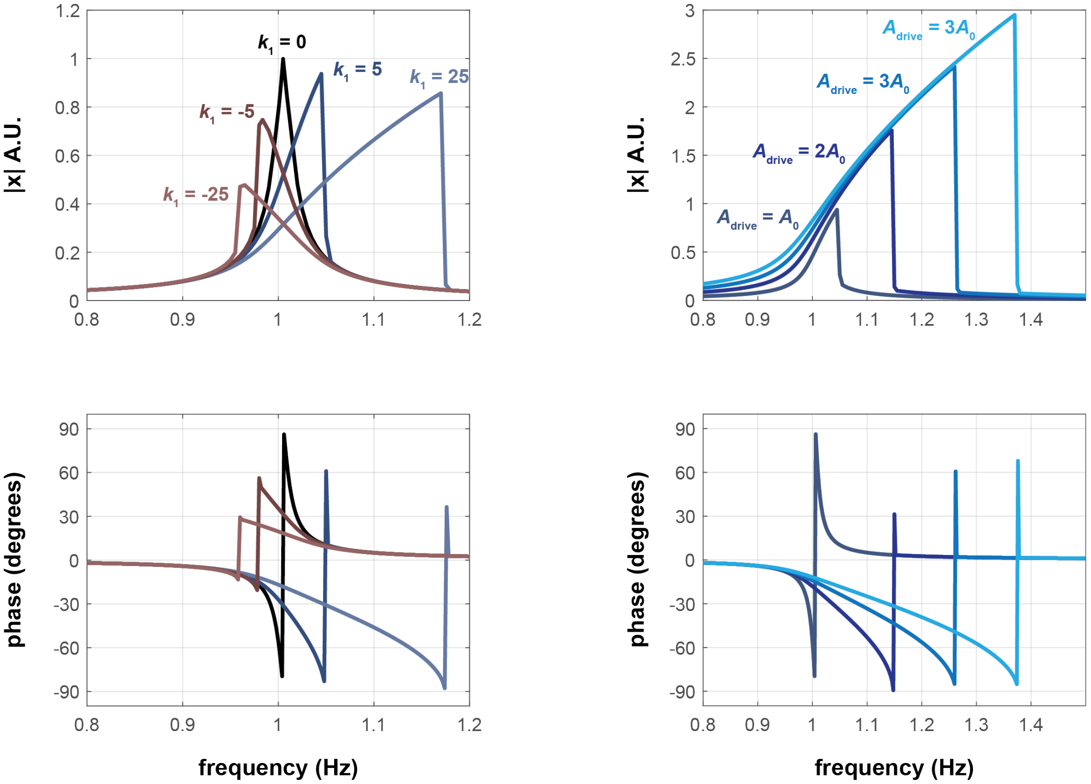

Figure 2·11: Duffing oscillator resonant responses. Amplitude response (top row) and phase response (bottom row) are shown for varying non-linear spring constant k_1 (left side) and for varying drive amplitude, A_0 (right side).

obtain the typical resonant response of the SHO. On the right side of figure 2·11 we have set $k_1 = 5$.

As explained previously, negative values of k_1 result in spring softening, which shift the resonant frequency to lower frequencies, while positive k_1 values shift the frequency upwards. The resonant curves in the case of large k_1 are wider and display more asymmetry. Instead of a linear oscillator, which climbs up one side towards its resonant peak and then back down the other side, Duffing oscillators will climb up one side then abruptly drop down to near zero amplitude. This jump represents an instability in the solution for equation 2.36 where there exist multiple solutions. In all the plots in figure 2·11, the frequency is swept from low to high. If one were to instead sweep from high to low frequencies, the discontinuous jump would occur at a different frequency.

The Duffing oscillator presented here, specifically one with spring hardening behavior, is a very good model of the doubly clamped plate system we use to detect the Casimir energy in chapter 4. We will use arguments from the results of this model versus what we observe in experiment to infer about what may be going on mechanically in our system at large driving amplitudes.

Chapter 3

Casimir Force Measurement

3.1 Project outline

In this chapter, the Casimir force between two spherical and planar metal surfaces is measured using a modified commercial MEMS accelerometer [Stange et al., 2019]. The operating principle of the device, the modification, and the measurement, are all discussed in the following sections.

3.2 MEMS accelerometers

Accelerometers are a part of our everyday lives, from sensing the orientation of smartphones (low g) to detecting collisions in automobiles in order to deploy airbags (high g). In this project, a two-axis low g MEMS accelerometer from Analog Devices (ADXL203) is used. Its proof-mass typically weighs about $1\,\mu\mathrm{g}$ and has a spring constant of $1\,\mathrm{N\,m^{-1}}$ so the accelerometer is therefore able to resolve approximately $1\,\mathrm{pN}$ of force. These platforms are thus well suited for Casimir force measurements. The goal of this project is to re-purpose the commercial MEMS accelerometer to perform a sensitive Casimir force measurement in ambient conditions. The main advantage of a modified accelerometer over other types of measurement methods is the pre-optimized design of the MEMS and the supporting integrated circuitry simplify the device fabrication and apparatus immensely. Compared to AFM, the size and cost is superior by orders of magnitude and the linear transduction of an applied force to an electronic output signal is a built-in feature of the accelerometer.

Furthermore, the ability to measure the Casimir Effect with commercial MEMS accelerometers is an exciting prospect because it indicates that this effect could be used as a practical, controllable engineering tool within a MEMS system. Successfully integrating a Casimir cavity into the well-developed, scalable technology of MEMS accelerometers is an important step in realizing Casimir-enabled sensing devices as a practical, room temperature quantum metrology tool.

3.3 Micro-gluing

Because the modification involves bonding objects to a post-release MEMS device, great care must be taken in keeping mechanical forces exerted on the freely moving proof-mass to a minimum. The technique presented here allows us to glue microspheres directly to the proof-mass of the accelerometer without compromising the functionality of the MEMS.

Outlined in figure 3·1b and 3·1d is our process which involves depositing $\sim$ pL volume droplets of UV curable epoxy using a micro-pipette attached to a piezoelectric actuator onto the proof-mass then dropping a microsphere onto the droplet using a probe tip (contact forces are sufficient to pick up the microsphere). The pipette or probe tip can be moved in plane with a micromanipulator while the Z position is controlled with nanometer precision using the piezoelectric actuator. An advantage of assembling onto a post-release MEMS accelerometer is that we can sense when contact with the proof-mass occurs by actively monitoring the noise on the outputs of the accelerometer (see figure 3·1b inset). This feedback is what allows us to deposit droplets gently onto the proof-mass without forcing liquid into the release holes or

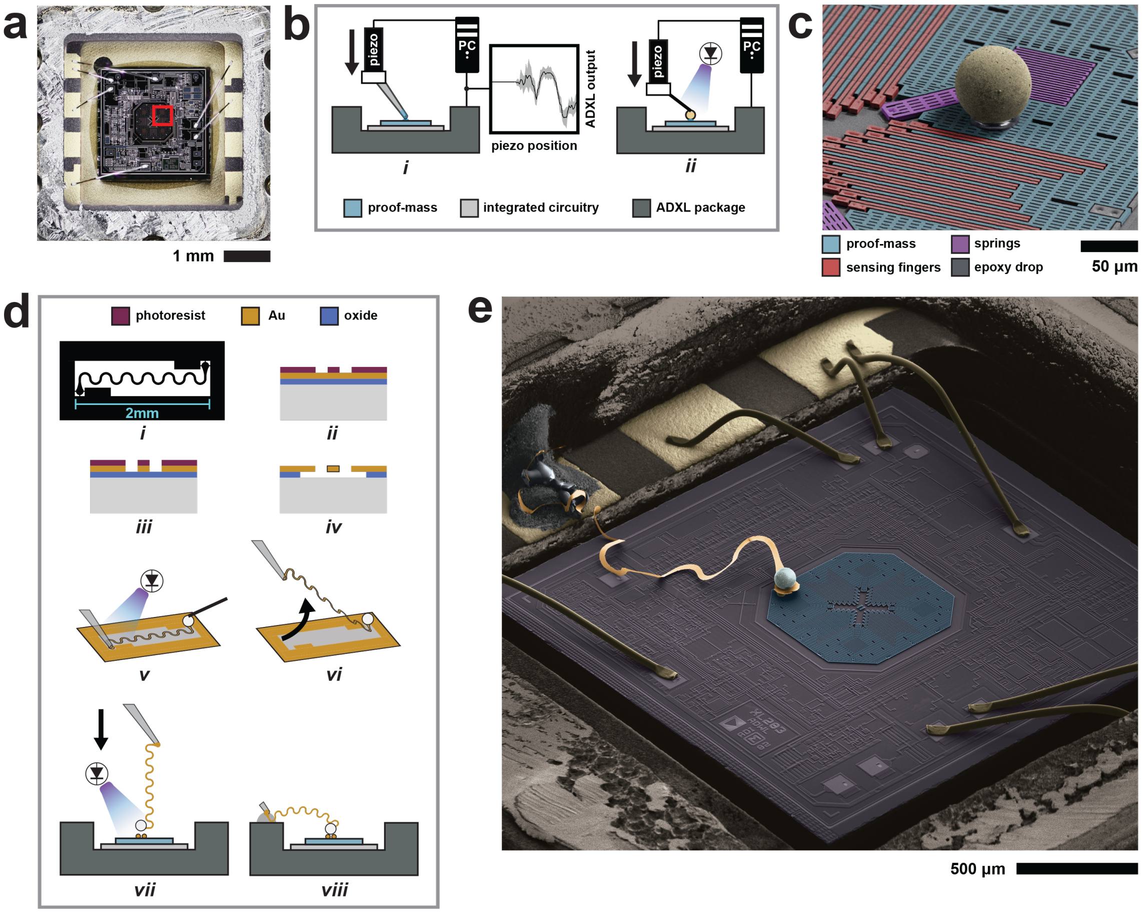
a
1 mm
b
piezo
PC
ADXL output
piezo position
i
piezo
PC
ii
proof-mass
integrated circuitry
ADXL package
c
proof-mass
sensing fingers
springs
epoxy drop
50 µm
d
photoresist
Au
oxide
2mm
i
ii
iii
iv
v
vi
vii
viii
e
500 µm

Figure 3·1: a). Top-view optical image of the ADXL203 die inside the package with the lid removed. The octagonal proof-mass can be seen in the center. Highlighted red box indicates the area of the proof-mass shown in the scanning electron microscope (SEM) image in c. b). Schematic of feedback-assisted attachment of microspheres onto the proof-mass. c). Colorized SEM image of one quadrant of the micro-electromechanical system (MEMS) with a microsphere glued to the proof-mass using the micro-gluing technique. The interdigitated sensing electrodes and anchoring springs of the proof-mass can also be seen. All of the MEMS structures are 4 µm thick. d). Schematic of device assembly steps. e Colorized SEM image of an example of a fully modified ADXL203 (not the device used in this work).

breaking the springs. As shown in figure 3·1b.i. the ADXL output is monitored while a piezoelectric actuator lowers a micro-pipette (30 µm tip diameter) containing UV curable epoxy. Upon contact, surface forces draw out a few picoliters of epoxy and the pipette is automatically retracted. In figure 3·1b.ii. the ADXL output monitored as before while the sphere is lowered into the droplet. Once contact is made, the epoxy is cured by ultraviolet (UV) exposure.

As can be seen in figure 3·1c, the proof-mass (shown in blue) provides only a few small areas over which droplets can be placed without interfering with other parts of the MEMS such as the sensing fingers or the springs. In order to attach larger objects, we use one or more spheres (Au-coated solid barium titanate glass) as supports for other objects to be set upon, like legs of a table. Once these "legs" are formed, one can then attach a wide variety of micro-scale objects providing they don't interfere with the MEMS and are able to be picked up and placed gently. For example, it is possible to place a sub-mm neodymium rare-earth magnet on top of the support spheres for high resolution gradient magnetometry [Javor, 2018]. For the device presented here, two 30 µm diameter solid spheres were glued onto the proof-mass as a platform for the rest of the assembly to be built on top of.

The functional component of the device is a conductive microsphere attached to the proof-mass of the inertial sensor that forms one-half of the Casimir cavity. Doing this results in a device that can not only measure accelerations applied to the device body (as was originally intended) but also forces exerted directly onto the sphere, namely electrostatic and Casimir forces. The sphere is 55 µm in radius, made up of a hollow borosilicate glass shell coated with 50 nm of Ag. It has a mass of roughly 0.1 µg. It was found that Ag-coated hollow spheres had much lower surface roughness than Au-coated solid spheres (appendix A.1), so an Ag sphere was used in the Casimir cavity, while two smaller Au spheres (about 0.5 µg each) were used as supports. It should be noted that the mass added to the proof-mass does not affect the functionality of the device at DC. For dynamic measurements, however, the added mass does lower the overall bandwidth of the device.

3.3.1 Residual electrical potential

One requirement in any Casimir device is the ability to control the electric potential on the interacting surfaces. This is due to the presence of residual electrostatic forces, which are caused by trapped charges, adsorbates, and the poly-crystalline nature of the metallic surfaces [Van Blokland and Overbeek, 1978, Lamoreaux, 1997, Nonnenmacher et al., 1991]. The latter results in local differences in the work function of the materials (also known as patch potentials), which sum up to a non-zero effective potential difference, even when the materials are electrically connected [Speake and Trenkel, 2003]. This overall residual potential is a common source of error in Casimir force measurements if not controlled for. To do this, a 500-nm-thick serpentine ribbon wire connects the surface of the Ag microsphere to an open bonding pad on the ceramic package. The conductivity of the wire provides a means of controlling the voltage on the sphere and its flexible geometry ensures a low spring constant, thus allowing for minimal restriction of the motion of the proof-mass and the restoring force of the poly-silicon springs. The lithography mask for the nano-ribbon wire (figure 3·1d.i.) is designed with a 2 mm nominal length, 25 µm lateral width, and a 58 µm radius circle at each end for attachment.

The effect that the wire has on the overall effective spring constant of the system (and therefore the force sensitivity) is minimal and easily accounted for as the post-modification force sensitivity is re-calibrated by using known electrostatic forces between the sphere and the plate. Additionally, because the electrostatic calibration is done with the sphere and plate in the same configuration as the Casimir force measurement, any rotational movement of the proof-mass due to torque applied from the sphere (which is not perfectly centered) will be accounted for. The process of assembling this device is shown schematically in figure 3·1d. After fabricating the wires out of a 500 nm layer of evaporated Au on oxide with standard lithography and etching (3·1d.ii.–iv.), the device is assembled (3·1d.v.–viii.) by attaching a microsphere to one end of the wire, peeling the wire off the substrate with a pipette, then lowering the Au nano-ribbon wire (with the Ag sphere attached) onto two smaller support spheres, which have been previously bonded to the ADXL203 proof-mass using the micro-gluing technique shown in 3·1b.

3.4 Apparatus and measurement

The modified ADXL203 is mounted on an XY translation stage attached to an optical breadboard. On the same breadboard is another XYZ stage on which the Au-coated plate (which forms the second half of the Casimir cavity) is mounted. This stage has its Z position controlled by a Newport Picomotor stick-slip piezoelectric actuator. An additional Newport NPC3SG piezoelectric stack actuator controls the fine position of the plate in the X direction. The apparatus is contained inside a polystyrene foam container along with a 50 Ω power resistor and resistance temperature detector for PID controlled temperature with a 28 °C setpoint. Due to building heaters cycling on and off, the maximum temperature variations inside the enclosure over long periods of time are $\sim 12\,\mathrm{m}^\circ\mathrm{C}$; however, for shorter time periods (2 h or less), the temperature can be held within $\sim 3\,\mathrm{m}^\circ\mathrm{C}$. The entire setup is mounted on an optical breadboard

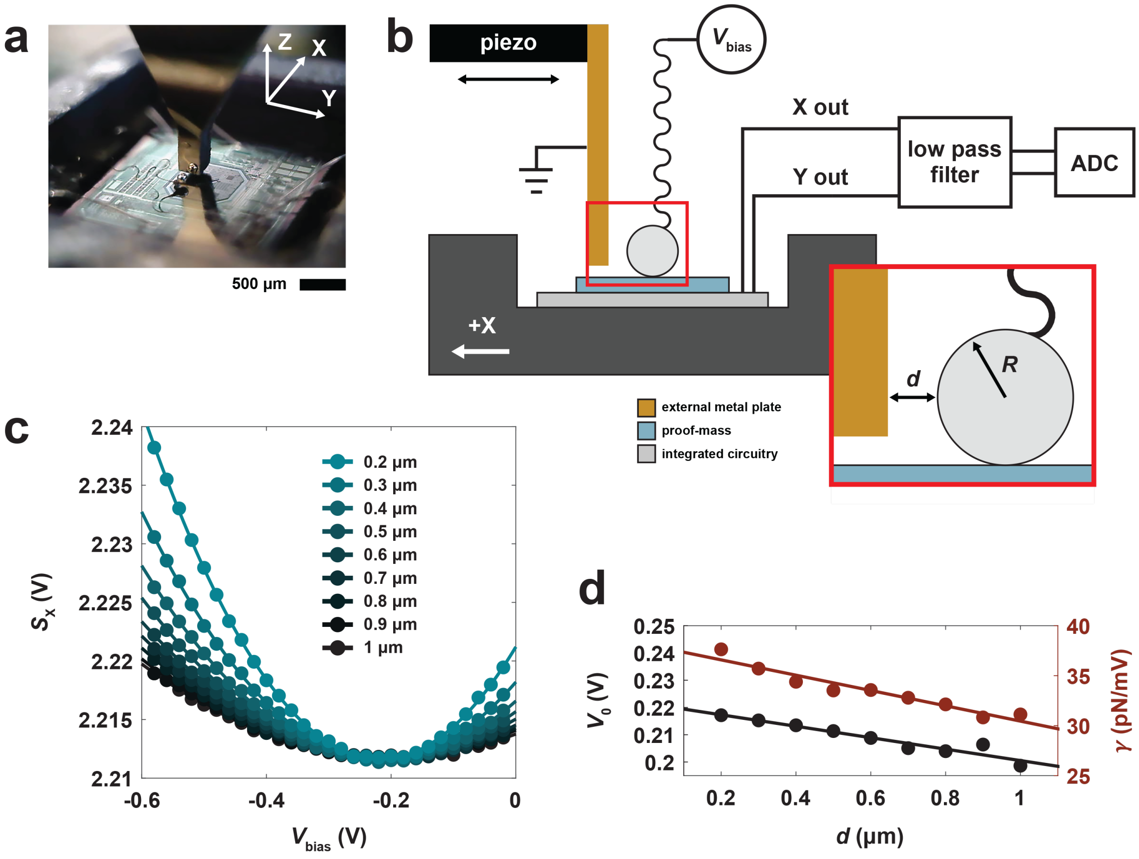

Figure 3·2: a. Optical image of the modified ADXL203 used to collect the data presented in this thesis. Also pictured is the external Au-coated plate mounted on a piezoelectric actuator (out of frame). b. Schematic of full setup. The sensor X and Y outputs are fed through an 8-pole low-pass filter with a 3 Hz cutoff to isolate the desired direct current (DC) signal and then read by a 16-bit ADC. The Casimir force acts along the X direction for this particular device. INSET: Diagram of Casimir cavity geometry showing sphere-plate separation (d) and sphere radius (R). For simplicity, the two support spheres are not pictured. In reality, the Ag sphere is sitting roughly 30 µm above the proof-mass. c. Sensor signal data as V_{bias} is varied at different separations. Circles are measured data and the solid lines are second order polynomial fits to the data. d. V_0 and γ versus separation. These values are computed from the minima and curvature of parabolas fit to data in c.

and contained in a temperature-controlled enclosure on top of an active vibration isolation table. A schematic of the device and apparatus can be seen in figure 3·2.

3.4.1 Methods

Electrostatic force calibration and residual potential cancellation

As discussed in section 3.3.1, electrostatic forces are present between the sphere and plate metal surfaces, even when the two metals are shorted together. By applying a voltage equal and opposite to the residual potential, this unwanted electrostatic effect can by minimized. Additionally, by applying known electrostatic forces between the plate and the sphere, the force sensitivity of the output can be calibrated.

The forces acting on the sphere are assumed to be only due to electrostatic and Casimir interactions. For the following equations, we define the separation: $d = x_p - x_s$, where x_p is the absolute position of the plate and x_s is the absolute position of the sphere. Assuming a simple electrostatic model, we can write:

$$F(d, V_{\text{bias}}) = \frac{\epsilon_0 \pi R (V_0 + V_{\text{bias}})^2}{d} + F_{\text{Casimir}}(d) \tag{3.1}$$

where ϵ_0 is the permittivity of free space, V_0 is the residual potential, V_{bias} is the applied DC voltage between the sphere and plate, and R is the radius of the sphere. Equation 3.1 uses the PFA for a sphere-plate geometry, which assumes $d \ll R$. At large separations (typically $> 200\,\text{nm}$) and large applied voltages ($V_0 + V_{\text{bias}} > 100\,\text{mV}$), the Casimir force term is negligible, and the force scales as V_{bias}^2. The residual potential can be measured by sweeping the bias voltage and finding the value of V_{bias} at which the force is minimized. At this minimum, the applied bias is equal and opposite to the residual potential.

The sensor outputs an analog voltage, so to get a measurement in units of force, a calibration must be performed. Because of the linear response of the device, the output signal, S, is proportional to the force applied on the proof-mass by a constant, γ:

$$F(d, V_{\text{bias}}) = \gamma S(d, V_{\text{bias}}). \tag{3.2}$$

For large separations and voltages, we can ignore the Casimir term in equation 3.1 and can now write:

$$S(d, V_{\text{bias}}) = \frac{1}{\gamma} \frac{\varepsilon_0 \pi R \left(V_0 + V_{\text{bias}}\right)^2}{d}. \tag{3.3}$$

We can then write γ in terms of the second derivative of the signal with respect to V_{bias}:

$$\gamma = \frac{2\pi\varepsilon_0 R}{d} \left(\frac{\partial^2 S}{\partial V_{\text{bias}}^2} \right)^{-1} \tag{3.4}$$

From these relations, the residual potential and force sensitivity can be measured by fitting the raw signal data, S, to the function $S = c_1 V_{\text{bias}}^2 + c_2 V_{\text{bias}} + c_3$. Using the returned fitting parameters we can calculate:

$$V_0 = \frac{c_2}{2c_1} \tag{3.5}$$

$$\gamma = \frac{\varepsilon_0 \pi R}{c_1 d} \tag{3.6}$$

provided we are in a region where the electrostatic force is dominant over the Casimir force.

3.4.2 Measurement calibration

Electrostatic forces are used to measure the residual potential difference, V_0, between the sphere and the plate and to calibrate the force sensitivity, γ, which relates the sensor output voltage, S, to the applied force according to $F = \gamma S$. In figure 3·2c the voltage output in the X direction (S_X) is plotted versus potential applied between the grounded plate and the microsphere (V_{bias}). This measurement is repeated over a range of separations between 200 nm and 1 µm where electrostatic forces are much larger than the Casimir force. The minima of these voltage sweeps indicate the bias that cancels residual potential between the metal surfaces, and the curvature of the sweeps give a calibration coefficient between the sensor voltage output and force, which can then be used for Casimir force measurements (see detailed discussion in section 3.4.1).

Both the residual potential and the force sensitivity of the device appear to be functions of separation and are approximately linear. Over the full 800 nm scan range, it is observed that V_0 varies by 9 % and γ varies by 20 %, with average values of 0.21 V and 33.5 pN/mV, respectively.

3.5 Results and discussion

3.5.1 Casimir force measurement

The procedure for a single measurement is as follows–first the plate is moved by steps of 20 nm towards the sphere until contact is sensed. The plate is then retracted by 1 µm and V_{bias} is swept, tracing out a parabola as shown in 3·2c, according to equation 3.3. More sweeps are taken as the plate is moved closer by steps of 100 nm. Every data point is the average of 50,000 samples taken in 0.5 s by the ADC with standard deviations between 0.6 and 0.7 mV. The whole electrostatic measurement takes 3.5 min. Over this period of time, thermal drift is negligible (see appendix A.3). Fitting a second-order polynomial to these data sets provides measurements of the residual potential, V_0, as well as the sensitivity, γ, according to equations 3.5 and 3.6. These values are plotted in figure 3·2.

Immediately following the electrostatic measurement, the plate is retracted back 1 µm away from the sphere and then stepped forward by 1 nm increments as V_{bias} is adjusted according to the linear fit, ensuring that the first term of equation 3.1 is minimized at every position. At each plate position, 50,000 samples are taken in 0.5 s using the ADC. This measurement takes 20 min, which requires that the enclosure temperature remain within 3 m°C to avoid unwanted thermal drift (see appendix A.3).

After subtracting the zero-force signal (c_3), the measured data is scaled to units of force using the calibration factor $\gamma(d)$ measured from the electrostatic data. It is then fit to either the ideal Casimir theory (equation 2.24) or the corrected Casimir theory (equation 2.28), with x_s as the only free parameter. These results can be seen in figure 3·3.

The data in figure 3·3 is a measurement of the force applied to the proof-mass along its X axis as a function of separation between the Ag-coated microsphere (which is attached directly to the proof-mass) and an external Au-coated plate. Electrostatic contributions have been minimized by adjusting V_{bias} to be equal and opposite to V_0 at each plate position. The red and black data points are the same set of data fit to either the ideal Casimir force theory (solid red line) given by equation 2.24 or the corrected Casimir force theory (solid black line) given by equation 2.28 with only x_s (i.e., where separation $d = 0$) as a free parameter. According to the ideal fit, the last measured data point at 635.5 pN is 65 nm away from $d = 0$. According to the

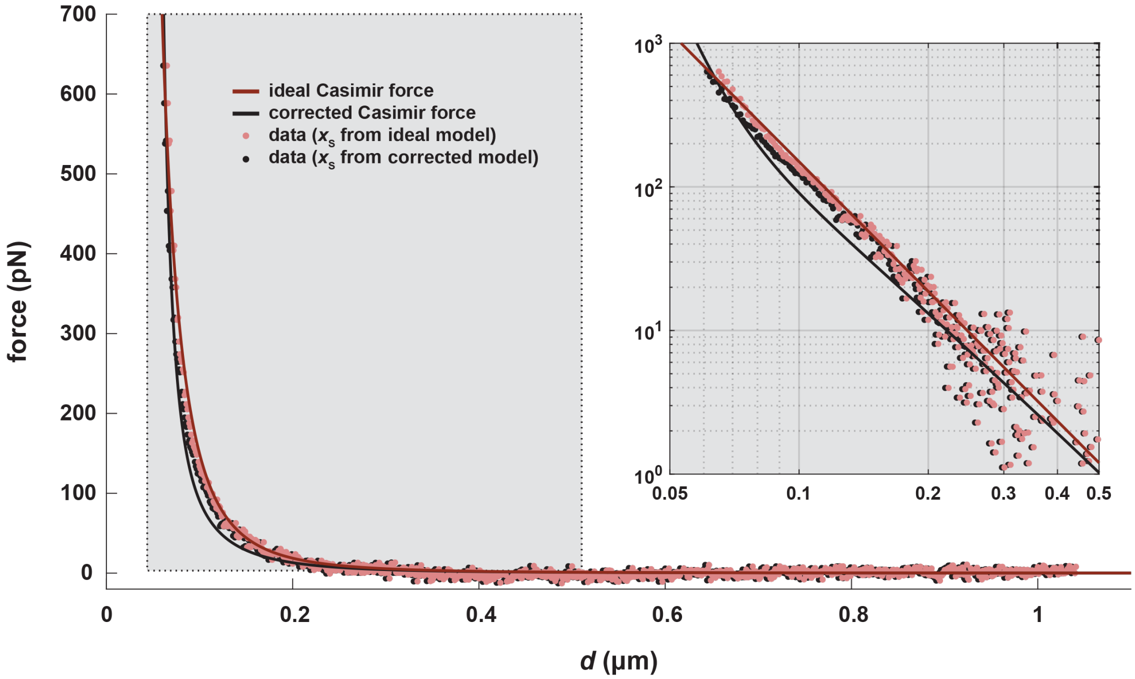

Figure 3·3: Measurement of the Casimir force using the modified accelerometer device. Actual measured data (dots) are compared with ideal theory (equation 2.24, red line) and theory for real metals (equation 2.28. Inset shows the highlighted section of the data in log–log scale for better comparison between data and theory at small separations. The two sets of data are identical but shifted by 2 nm along the abscissa because of the different values of x_s returned from the fits to equations 2.24 and 2.28.

corrected Casimir fit, the last measured data point is 63 nm away from $d = 0$.

3.5.2 Discussion

Distance dependence of residual potential and sensitivity

The separation dependence of the residual potential is a well-known occurrence [Kim et al., 2008, De Man et al., 2009, Behunin et al., 2012] as the potential measured is an effective sum of the contributions from different regions across the surfaces of each metal. As the separation changes, these contributions will sum differently due to the inverse square dependence of the electrostatic force. The linear dependence of the force sensitivity of the device is due to the interaction of the grounded silicon plate with the fringe fields of the interdigitated capacitor fingers of the sensor. The capacitive sensing relies on a small AC signal applied between the fixed fingers and the movable fingers. Because the plate is held at the same ground as the device, it will deflect fringe field lines from this applied voltage and result in an out-of-plane force exerted on the grounded fingers [Tang et al., 1992, Imboden et al., 2014c]. As the plate's position is varied it will overlap with more fringe fields, thus exerting a larger out of plane force and decreasing the sensitivity. This effect is more prominent the closer the plate is to the fingers (see appendix A.2). Therefore, there is an ideal range of plate heights at which the experiment can be performed, where the fringe field interactions are minimized while also ensuring adequate area of interaction between the side of the sphere and the plate.

Casimir force comparison with theory

In figure 3·3 it can be observed that the measured data is modeled more accurately by the ideal Casimir theory (root mean squared error of 7.4 pN) compared to the corrected theory (root mean squared error of 10.5 pN). While the corrected theory takes into account the finite conductivity and non-zero temperature of the surfaces, the perturbation approach used in [Geyer et al., 2002] is in fact only valid for separations ranging from a few hundred nanometers to several micrometers. At short separations, the dielectric permittivity of the respective metals at high frequencies contributes to the force magnitude and changes the scaling with separation (V.M. Mostepanenko, personal communication, October 26, 2018). As a result, although the ideal theory overestimates the measured force in the 80 to 200 nm range, the corrected model in equation 2.28 underestimates it by far greater. More accurate fitting may be possible by performing a numerical calculation of the Lifshitz formula using optical data for the complex index of refraction of the metal surfaces, but such analysis is outside the scope of this study.

Considering random measurement errors, the linear fits shown in figure 3·2d returned root mean square errors to the data of 1.8 mV and 0.6 pN/mV for V_0 and γ, respectively. Assuming a mis-calculated V_0 off by three standard deviations (5.4 mV) at the closest point of approach of 60 nm, we would be introducing an unwanted additional electrostatic force of 0.74 pN, which is just 0.1 % of the Casimir force measured at that point. This value is also much less than the random error in the force measurement due to uncertainty in the product γS_X (whose combined errors propagate to as high as 60 pN at the closest measured point). It is therefore likely that the discrepancy between measurement and theory in this distance range is not due to imperfectly canceled electrostatic forces, as the Casimir force is the dominant interaction.

The reason for this discrepancy is most likely due to the assumptions of the geometry of the cavity, both at the microscale (i.e., sphere and plate shapes and arrangement) and at the nanoscale (surface roughness). The sphere radius, R, is used in both the electrostatic calibration analysis as well as the theoretical Casimir fits. In both cases, we use R in the framework of the PFA, which assumes a perfectly spherical surface and an infinite plane in the $d \ll R$ limit [Derjaguin, 1934]. Because of this, both the calibration factor and the Casimir force are proportional to R, so any errors in the value of R (which was measured optically) do not affect the fitting. However, if the sphere is not perfectly spherical, then we would expect both the electrostatic force and the Casimir force to scale differently depending on the exact shape [Gies and Klingmüller, 2006]. Additionally, due to physical constraints of our setup, the plate is limited to extend only $80 - 90\,\mu\text{m}$ below the central plane of the sphere. Because the PFA assumes an infinite plane, this asymmetry may result in a systematically overestimated force sensitivity of the device.

The surface roughness also becomes very important in Casimir interactions at separations less than $\sim 100\,\text{nm}$ [Van Zwol et al., 2008, Broer et al., 2012]. The AFM scans taken were on separate samples (see appendix A.1), which went through the same coating processes as the sphere and plate used in this device. While this may be useful for capturing average roughness values, it is not specific to this exact cavity, which may have extreme asperities that cause deviation from the expected scaling below $100\,\text{nm}$ separations and also invalidate the PFA assumption. To improve both of these geometry-related systematic uncertainties, characterization of individual spheres would need to be done prior to subsequent assembly.

Nevertheless, our results show that a Ag surface and a Au surface in our atmospheric MEMS system exhibit an interaction that can be described quite well by the ideal Casimir force model. This is a promising finding for future work with Casimir-enabled sensing devices, such as that described by [Imboden et al., 2014b]. The results presented here imply that approximating this interaction as a simple inverse cubic relation is quite sufficient for further analysis and modeling.

Chapter 4

Casimir Energy Detection

4.1 Experimental concept

As explained in section 2.3, it is thought that the sharp response of a superconducting phase transition may allow us to detect slight variations in the Casimir Energy [Bimonte et al., 2005c]. Other work that has attempted to measure this has made use of rigid cavities with dielectric media in between [Bimonte et al., 2005b, Bimonte et al., 2005a]. These cavities can be fabricated with different gap sizes, and it is thought that by measuring several of these "stacks", one might be able to see a shift of the transition correlated with the gap size. A problem with this approach, however, is the highly process-dependent characteristics of superconducting thin films. Even on a single die, different regions of deposited material may display a slightly different superconducting transition temperature due to thickness variation, local roughness, or temperature gradients during deposition. In order to see a change in T_c from a varying Casimir energy, it is estimated that one must be able to measure T_c with a resolution on the order of µK [Bimonte et al., 2008]. It is therefore necessary, in our opinion, that the measurement be done on a single sample with a dynamically tunable cavity, rather than on several different samples with differently sized rigid cavities. This nano-electromechanical approach allows for measurement of one single film with a resolution of around 5 µK.

The goal of this project is to monitor the superconducting transition temperature of a thin film, which constitutes one half of a Casimir cavity, as the size of the cavity is varied. To do this, a nano-mechanical structure is required which consists of a mechanically fixed film of Type-I superconducting material in close proximity to a movable metal plate. If the film and plate are separated by an air gap, the metal plate can be actuated electrostatically by applying a voltage on nearby fixed electrodes, thus changing the size of the cavity. Some requirements of the device are as follows:

- the gap must be on the order of 10s of nanometers
- the transition temperature of the film must be greater than 4K due to limitations of the cryostat
- the film must be smooth and continuous
- both the plate and the film should be pure materials with no oxidation layers

To meet these requirements, Au was chosen for the plate material as it is a noble metal with very good chemical resistance to oxidation, is straightforward to pattern at the sub-micron scale, and is commonly studied as a Casimir material [Decca et al., 2003, Laurent et al., 2012, Rioux et al., 2014, Klimchitskaya et al., 2009].

Another key aspect of the device is the film itself. Depositing very smooth thin films is often difficult with conventional cleanroom methods due to the tendency for the atoms to cluster and form non-continuous islands of material upon landing on the target surface [Neugebauer and Webb, 1962]. This is due to the relatively high kinetic energies of the vaporized atoms landing on a substrate which gives them the mobility to re-arrange and cluster together. It has been shown that evaporating onto a cryogenically cooled surface allows for quench condensation of the material, and can form very smooth, amorphous films [Ekinci and Valles, 1999, Imboden et al., 2017]. For this reason, an *in situ* deposition method is developed in which the superconducting film is deposited at the chip scale, below the superconducting transition temperature. This “fab-on-a-chip” methodology is explained further in section 4.3 as well as in [Imboden et al., 2014a, Han et al., 2015, Imboden et al., 2017].

For the superconducting material, the requirements of Type I and $T_c > 4\mathrm{K}$ allows for Lanthanum, Lead, Tantalum, and Titanium Nitride. Ta and TiN are difficult to evaporate due to their high melting points [Leichtfried et al., 2004] and La displays two different critical temperatures depending on its crystal structure [Ziegler et al., 1953]. For these reasons, Pb, whose bulk structure displays a superconducting transition at 7.196 K was chosen.

In order to deposit a continuous Pb film underneath a Au layer, a three-die configuration was developed (as shown in figure 4·1) in which one target die (the “target” onto which material will be evaporated) is centered between two source dies (material “sources”). The flux of material being evaporated diagonally from each source die will reach the target die and form a continuous film underneath the center of the top Au layer. This top Au layer on the target die serves as both a movable plate and a physical mask. The source dies essentially consist of an array of micro-scale heaters that serve as crucibles for evaporation. Their design and fabrication are explained further in section 4.2.2.

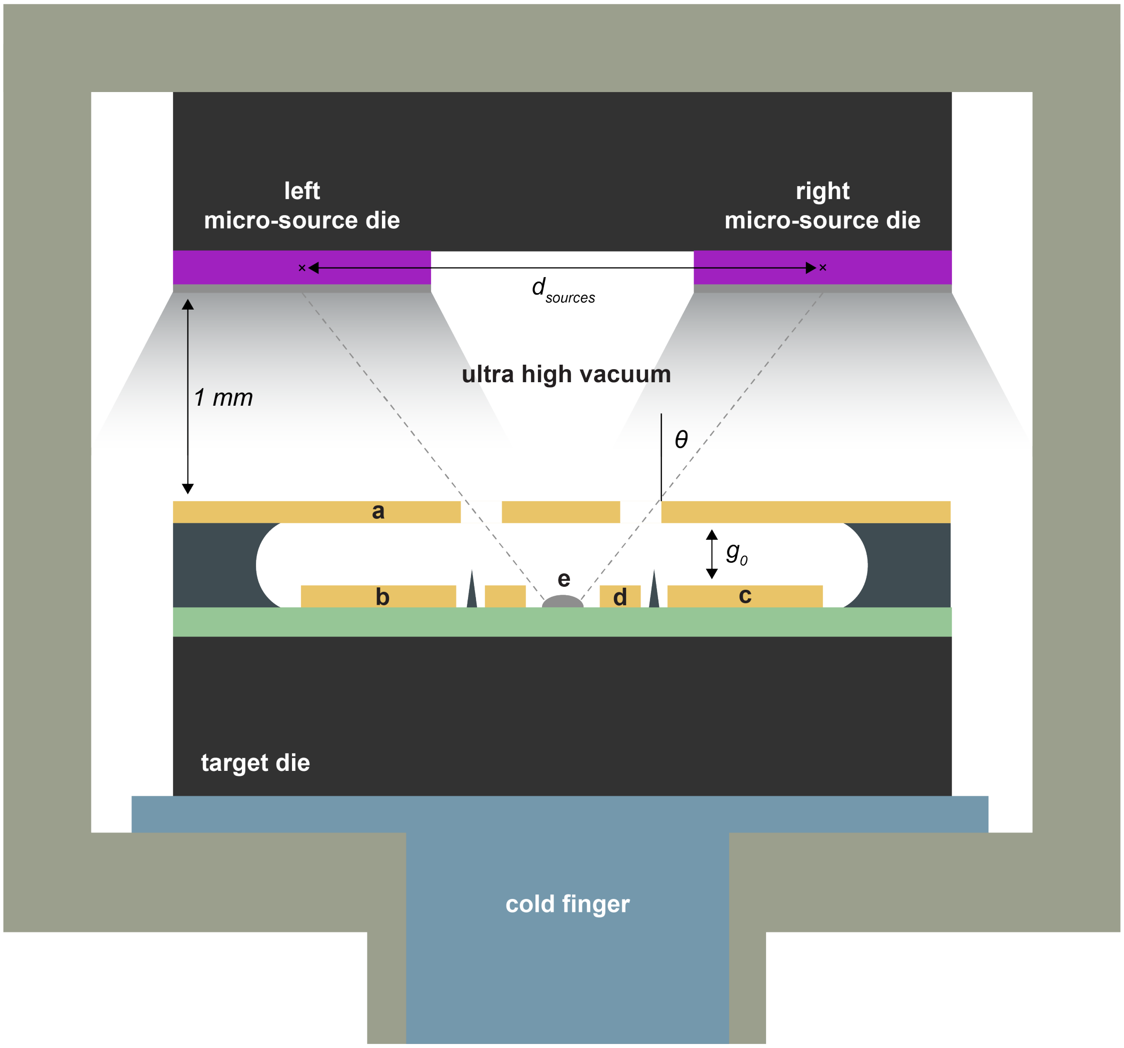
left
micro-source die
right
micro-source die
$d_{sources}$
ultra high vacuum
1 mm
θ
a
g_0
e
b
d
c
target die
cold finger

Figure 4·1: Schematic of the cryogenic die arrangement for low temperature Pb deposition and Casimir measurement. On the target die is the nano-mechanical cavity. This consists of a movable Au top surface (**a**), actuated and sensed by electrodes **b** and **c**. Au guard rings (**d**) surround the electrodes, reducing stray electric fields. The top Au layer also functions as a shadow mask for Pb deposition. Short silicon dioxide pillars are left over from the release process which prevent stick-down and allow for accurate gap size measurements. Two micro-source dies are mounted 1 mm away and laterally spaced by d_{sources} in order to create the required angle θ that results in a continuous Pb film (**e**) deposited underneath the top Au layer. The top Au layer is spaced from the bottom Au and Pb by an silicon dioxide layer of height g_0.

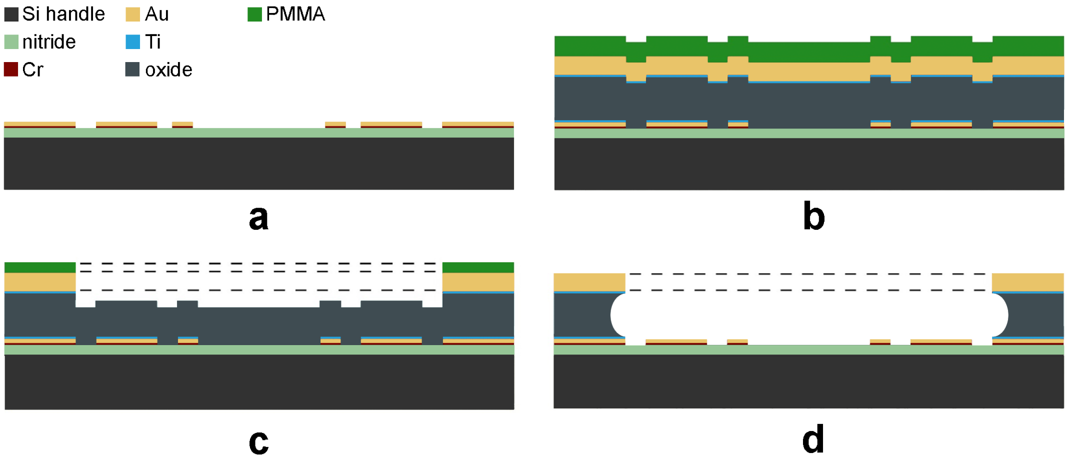

Figure 4·2: Nano-cavity fabrication process. **a.** bottom metal is patterned into electrode, guard, and 4-point leads. **b.** Oxide, Au, and PMMA is deposited. (**c**). EBL patterning and subsequent ion milling of the top Au layer to form shadow mask and allow for plate movement. **d.** The device is released in BOE. This process was developed by Diego Perez at NIST.

4.2 Device design and fabrication

4.2.1 Target

The nano-electromechanical target die is fabricated using a custom layer-by-layer processing method developed and carried out by Diego Perez at the National Institute of Standards and Technology (NIST). A schematic of the process is shown in figure 4·2. First, a 50 nm thick SiN layer on an n-type Si wafer. Next, positive photoresist is patterned to define the bottom metal layer containing the bonding pads, electrodes, guards, and 4-point leads. A layer of 10 nm Cr followed by 50 nm Au is deposited by e-beam evaporation followed by a lift-off (shown in figure 4·2**a**. Next, 286 nm of silicon dioxide is deposited using a plasma enhanced chemical vapor deposition, defining the nominal spacing of the cavity. On top of this oxide layer, 10 nm of Cr followed by 100 nm Au is deposited with e-beam deposition. PMMA is then spin coated to create a resist layer for EBL patterning (see figure 4·2**b**). After EBL patterning and development of the PMMA layer, a Ar ion mill dry etch is used to create holes in the top Au layer to define the shadow mask pattern (figure 4·2**c**). Finally, the devices are released by removing the oxide in a BOE for 6.5 - 7.5 min.

A closer look at the EBL pattern and post-release nano-mechanical cavity can be seen in figure 4·3. The EBL pattern is designed to form a continuous thin film of Pb in a ‘H’ shaped pattern for an angled deposition at $\theta = 35°$. This corresponds to a center-to-center spacing of the micro-source dies $d_{\text{sources}} = 1.1\,\text{mm}$. The ‘H’ pattern will connect the four 4-point measurement leads as well as create one continuous line of Pb down the middle. Once released, the Au plate has a slight bit of curvature, concave towards the direction of actuation. The non-linear dynamics of pre-curved doubly clamped MEMS beam structures has been studied [Younis et al., 2010] and in certain cases shown to introduce more non-linearities than what is captured in the Duffing model. However, in the limit of small initial curvature, (in our case 30 nm of vertical displacement over 25 µm of beam length) the system shows typical spring hardening behavior as predicted by equation 2.36. This is confirmed in our observations of the resonance of the Au plate (section 4.5.2).

4.2.2 Sources

The evaporation of the Pb is done from two different dies, a left and a right. By adjusting the center-to-center spacing between the left and right die (d_{sources}), one can tune the angle of evaporation through the mask (see figure 4·1). The mask geometry used on the target die is designed for a center to center spacing of 1.1 mm. Each source die is 2.5 mm × 2 mm and consists of four individually addressable groups, each containing 24 micro-sources. Current is run in parallel through each group of 24 heaters individually. Figure 4·4**a** shows a colorized CAD file depicting the layout of the two micro-source dies and each of the 8 groups.

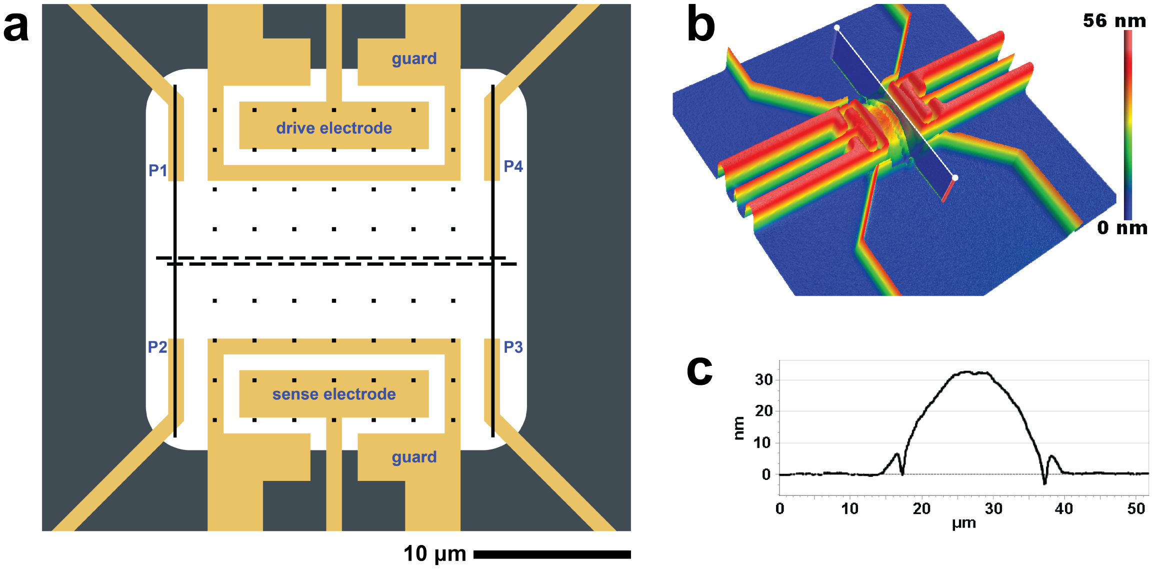
a
guard
drive electrode
P1
P4
P2
P3
sense electrode
guard
10 μm
b
56 nm
0 nm
c
nm
30
20
10
0
0
10
20
30
40
50
μm

Figure 4·3: To-scale diagrams and images of released nano-mechanical cavity for Casimir energy detection. **a**. top view schematic of the target die geometry. The bottom Au layer (in yellow) consists of two sets of electrodes and guards, and four leads for the 4-point measurement of the PB film. The black pattern is the EBL pattern which defines the holes opened up in the top Au layer. The 'H' pattern with dashed center results in a flexible Au plate that simultaneously serves as a shadow mask for angled Pb deposition. **b**. Height map of a released cavity taken from white light interferometer data. The slice indicated on the 3D plot is shown in **c**.

In order to get enough Pb material through the shadow mask and onto the target, a large area of the source dies must be covered in the MEMS heaters. Therefore, there is actually a large range of angles at which Pb gets deposited through the mask pattern. The actual center-to-center spacing of the micro-source dies is around 1.9 mm and the heaters are spaced over a distance of 2 mm which results in an angular deposition range of 24° to 58°. The Pb flux reaching the target at around $\theta = 35°$ is what contributes to the Pb side of the cavity, while the flux at smaller and larger angles contributes to making a good connection between the Pb film and the four Au measurement leads.

Prior to loading into the cryostat, 500-600 nm of Pb is evaporated onto the micro-source dies by heating a resistive thermal crucible inside a vacuum chamber. Some SEM images of pre-loaded micro-sources can be seen in figure 4·4**b** and 4·4**c**. The heaters consist of a poly-silicon square suspended on two ends by a serpentine connection. The small cross-sectional area of these connections causes Joule heating which radiates into the squares, and its serpentine shape allows for deformation and stress relief as it expands due to this heating.

4.3 *In Situ* deposition

The technique used to evaporate Pb from the micro-sources involves applying very small, very short pulses of power to the heaters in order to sublime very low volumes of material from the evaporated Pb. In this regime, very low atomic fluxes can be achieved, and high quality, thin films can be deposited on the target. Because the

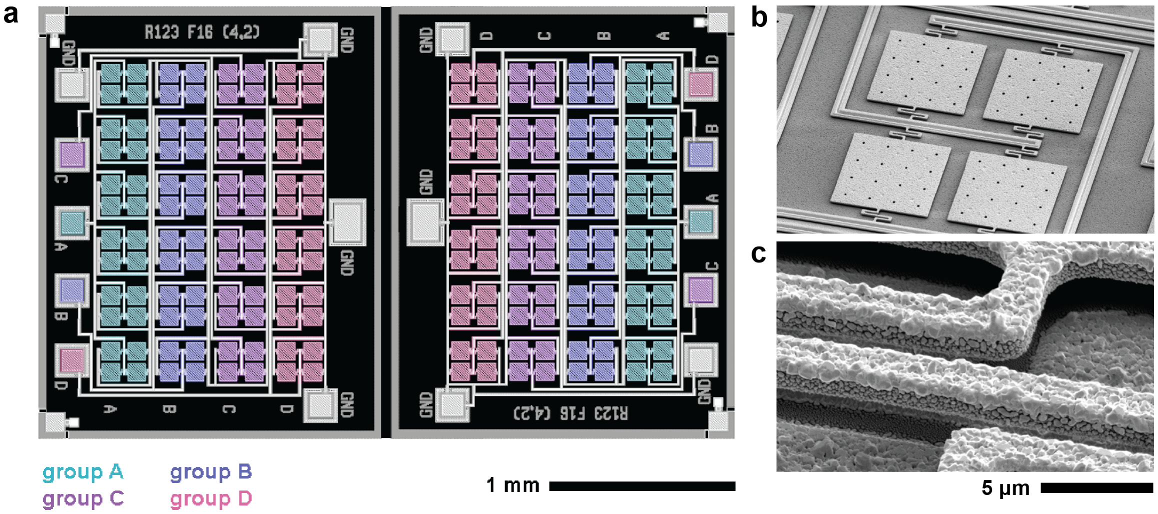

Figure 4·4: Micro-sources for quench condensed Pb deposition. **a.** Images of MEMS design files arranged to depict the actual micro-source configuration in the experiment. Two sets of dies, a left and a right, each contain 4 individually addressable groups of heaters, labelled A, B, C, D and color coded. By pulsing current through each group to ground (white bonding pads), we can sequentially deposit Pb from large angles towards small angles. **b.** SEM image of one set of 4 heaters. Current runs from the center of the quadrant in parallel through each heater to ground through serpentine connections. **c.** Zoomed in SEM image of the serpentine connection with Pb already loaded. The light material laying on top is Pb (about 750 nm thick) and the suspended poly-silicon structure can be seen beneath it.

system is at cryogenic temperature (about 2.9 K), the vacuum is very high, and there is minimal conductive heating between the micro-source poly-silicon and the substrate, or any other large heat-sinks. Therefore, very low power is required to heat the sources. Voltage pulses are applied to each group of sources sequentially, starting from the outside (groups A) and moving inwards towards groups D (see figure 4·4**a**). The reason for this is that as more and more Pb is deposited over the mask on the target, the holes will eventually fill up, reducing the amount of material that will make it through. Since more material is able to be deposited through the holes from directly above, it is desirable to start with the high angles, and finish with the deposition from above.

The waveform of the applied pulses is essentially a very low duty cycle square wave. There is a DC baseline voltage of 0.1 V upon which pulses are added. These pulses have a height of V_{pulse}, a duration of 10 ms and are applied every 2 s. To ensure a quality film is deposited, V_{pulse} begins at 0 V and is very slowly increased to 6 V - 6.5 V in steps of 0.01 V. At each new voltage level, 5 pulses are applied. As mentioned above, this process is repeated for each group of sources for a total of 8 depositions. As V_{pulse} is increased, the resistance of a group of sources, R_{source} changes, due to heating, and due to the changing amount of Pb on them. This resistance versus pulse height plot is shown in figure 4·5.

A typical plot of V_{pulse} is shown in figure 4·5. Certain characteristic points in the plot indicate important points in the deposition process. When deposition begins, a continuous layer of Pb coats the poly-silicon and the resistance is very low, allowing a high amount of current to flow. At around 2 V, (point A) some area of the Pb film melts due to this excessive current and now the current flows primarily through

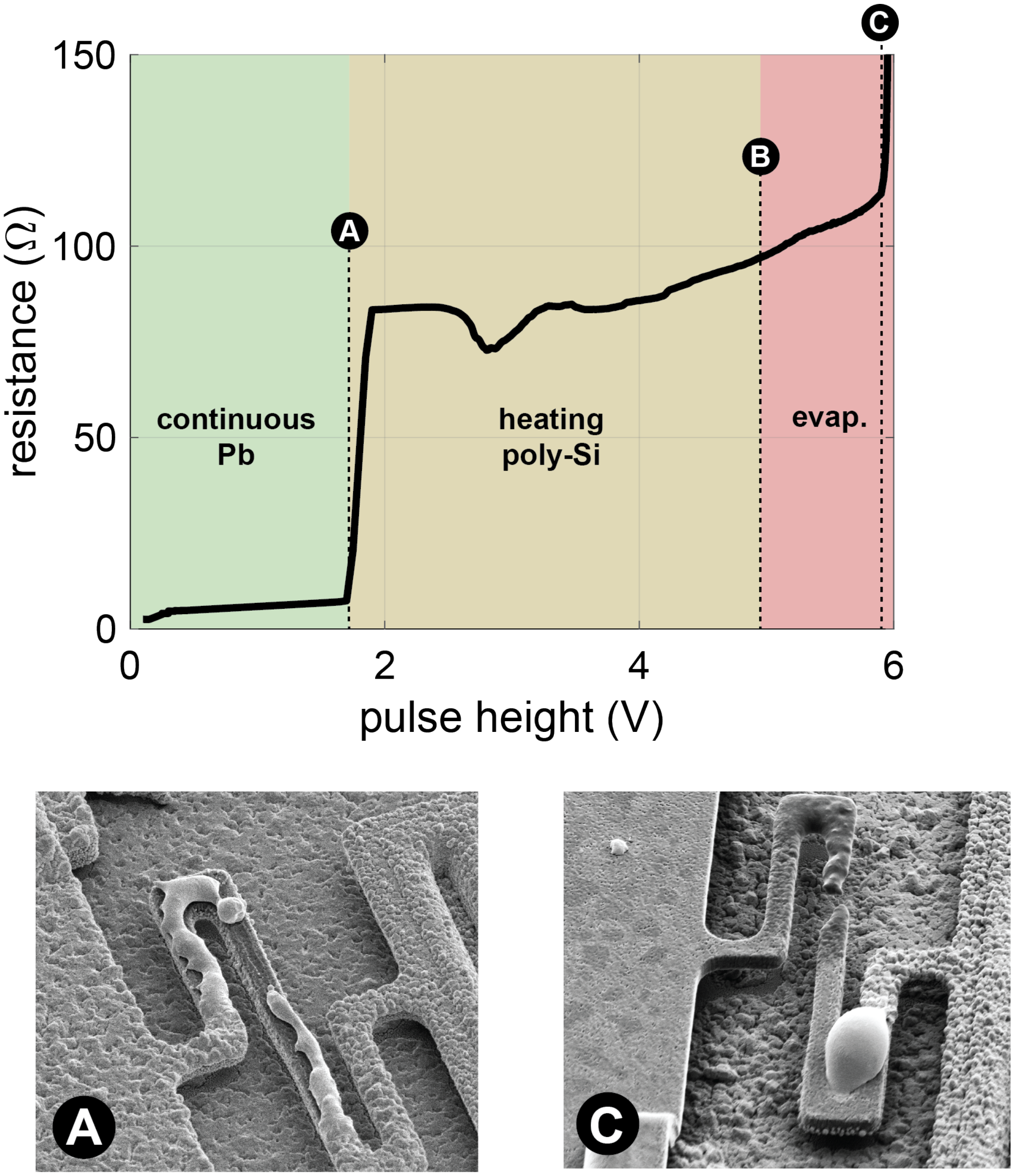

Figure 4·5: Plot of pulse height (V_{pulse}) versus resistance R_{source} for a typical deposition of Pb from a group of poly-silicon micro-sources. The resistance value indicates which stage of the heating and deposition process the system is at. At point A, the current is enough to cause one area of the Pb to melt, breaking the continuous layer and increasing the measured resistance. At point C, the current melts one or more of the poly-silicon springs.

the poly-silicon. This local melting likely occurs at a spring (not on the heater plate itself) where the current is highest. Consequently, the overall resistance increases substantially to 60-80 Ω. Beyond this point, as V_{pulse} increases, the poly-silicon plates begin to heat up. At around 5 V (point B), Pb material begins to deposit onto the target. This is not evident in the V_{pulse} vs. R_{source} plot, however a separate experiment was done in which the MEMS micro-sources were placed opposite a phase-locked crystal resonator (see appendix B.1). As material leaves the hot sources and lands on the resonator, the resonator mass increases, leading to a decrease in the measured frequency. This change was observed to begin at 5.1 V. Between points B and C, Pb flux is going through the target mask and landing on the substrate, forming a film. Eventually, the current going through the poly-silicon is enough to melt one of the poly-silicon springs (point C). This typically happens around 6 V, and this is indicated by a sharp jump in R_{source} to a few hundred Ω.

4.4 Plate actuation and sample measurements

As mentioned previously, the function of the top Au plate on the target is both to serve as a physical mask for the Pb deposition, but also to provide a movable reflective surface to tune the Casimir cavity. Actuation and sensing of the position of the plate is done using two Au electrodes, e_{drive} and e_{sense}. We consider two actuation schemes of the Au plate, static and dynamic. In the static scheme, a DC voltage is applied to the electrode causing an electrostatic force which pulls down on the Au plate.

The dynamic scheme involves applying an AC voltage (and therefore force) to the plate that coincides with its natural resonance. Because the plate geometry is close to that of a doubly clamped beam, the dynamic behavior is well described by a Duffing Oscillator model (see section 2.4.3 for further explanation).

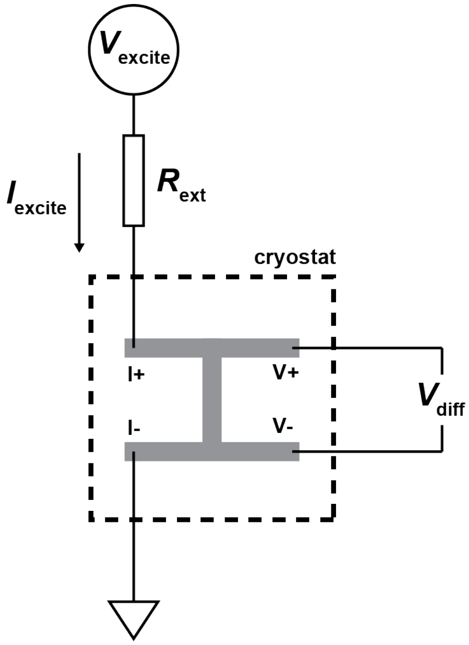

Figure 4·6: 4-point resistance detection scheme. Current is applied through an external resistance and the voltage drop across the Pb sample is measured. Here, the external 1 MΩ resistor and 1 kΩ resistor have been lumped together into one resistor.

In each of these actuation schemes, the resistance of the Pb film is measured using a 4-point configuration, shown schematically in figure 4·6. An excitation current, I_{ex} is applied at lead I+ (in series with an external 1 MΩ resistor) and travels through the central portion of the sample to I-, which is grounded through a 1 kΩ resistor. A voltage difference is then measured between the other two leads, V+ and V-. I_{excite} is a low frequency AC voltage of 5-20 nA at 37.7 Hz. The differential voltage measurement is measured using a lock-in amplifier and the resistance of the sample is then $V_{\mathrm{diff}}/I_{\mathrm{excite}}$.

In the DC detection scheme, the sample resistance, R_{s}, is obtained by considering a simple voltage divider between the sample and the external resistor, according to:

$$R_{\mathrm{s}} = 1.001\,\mathrm{M}\Omega \times \frac{V_{\mathrm{diff}}}{V_{\mathrm{excite}} - V_{\mathrm{diff}}} \tag{4.1}$$

With this measurement, two experiments can be done. First, a measurement of the superconducting transition of the Pb film can be characterized by measuring R_s as a function of temperature. This provides the slope of the transition, $\frac{dR_s}{dT}$ as well as T_c. Then, changes in T_c can be measured by setting the temperature of the system to just below T_c where $\frac{dR_s}{dT}$ is maximum and applying a DC bias to the drive electrode. As the DC voltage on the electrode increases, the plate is pulled downwards. If this change in position causes a change in T_c, this would manifest itself as a change in the measured resistance of the sample. We would be able to measure changes in T_c with a resolution given by the slope of the sample transition and the thermal noise in the cryostat.

The AC scheme involves detecting V_{out} at the same frequency the plate is moving. Again, if we set the cryostat temperature to the steepest part of the transition, the resistance measurement will be most sensitive to changes in temperature. Then, if the position of the plate does indeed influence the sample resistance due to the Casimir effect, we would expect a small modulation of R_s at the plate frequency. The voltage difference measured would then be:

$$V_{\text{diff}} = I_{\text{ex}} \times R_{s,0}\,(1 + \Delta R(t)) \tag{4.2}$$

Where $R_{s,0}$ is the nominal resistance and $\Delta R(t)$ is the small variation due to the plate. We can further break down ΔR:

$$\Delta R(t) = \underbrace{\frac{\partial R}{\partial T}}_{\text{transition slope}} \times \underbrace{\frac{\partial T}{\partial d}}_{\text{Casimir}} \times \underbrace{d(t)}_{\text{plate position}} \tag{4.3}$$

The ‘Casimir’ term is some change in T_c of the Pb sample due to the changing position of the plate, $d(t)$. This is what we hope to detect. Thus, if we consider only the component of V_{diff} at the plate frequency, whose amplitude we will label $|V_{\text{diff}}|_{\text{plate}}$, we can re-arrange equation 4.3 to obtain the amplitude of this expected effect:

$$\left|\frac{\partial T}{\partial d}\right| = \frac{|V_{\text{diff}}|_{\text{plate}}}{|I_{\text{ex}}(t)| \times \frac{\partial R}{\partial T} \times |d(t)|} \tag{4.4}$$

In this case, a more complex detection circuit is required. In figure 4·7, a high frequency AC drive signal is used to actuate the plate at its resonance. The plate amplitude is detected at twice this drive frequency using LIA 1. Simultaneously, a current is going through the sample at a low frequency, while V_{diff} is being measured at the same frequency as the plate using LIA 2. The output of LIA 2 is then fed into LIA 3 which is locked into the low frequency of the excitation signal. The DC output of LIA 3 is then equal to the amplitude $|V_{\text{diff}}|_{\text{plate}}$.

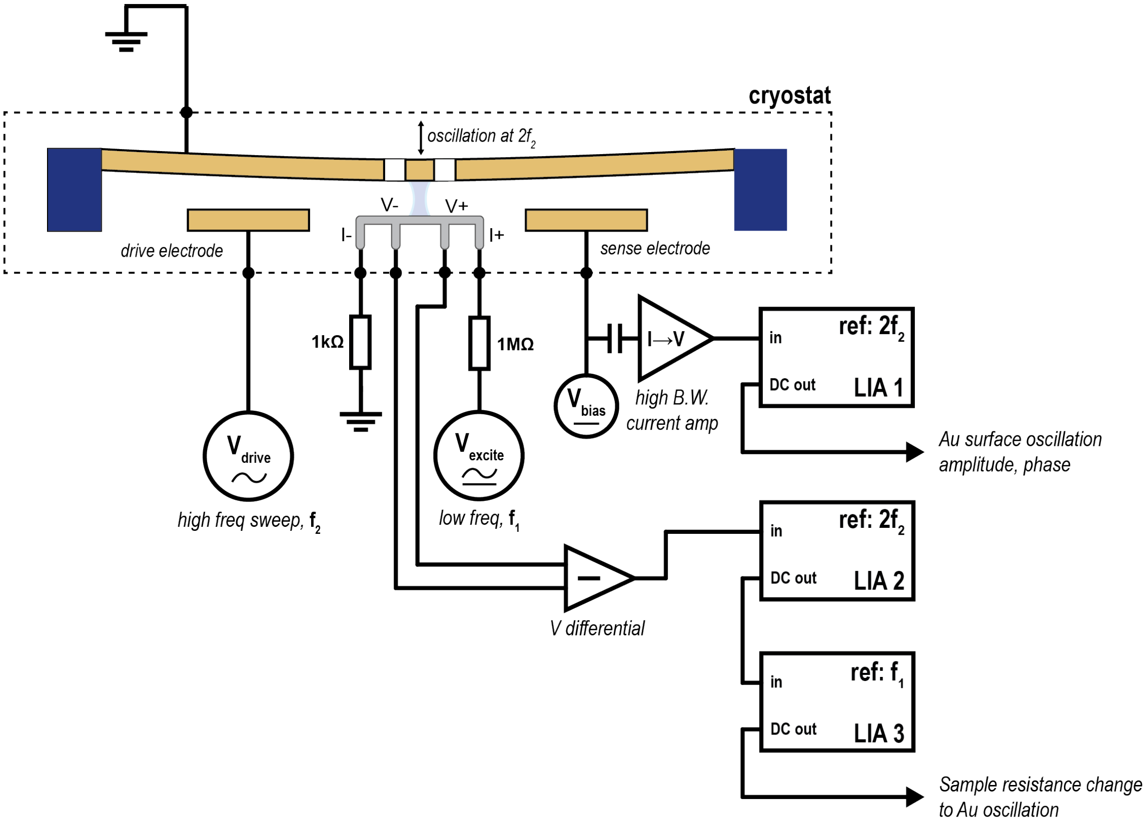
cryostat
oscillation at 2f2
V-
V+
I-
I+
drive electrode
sense electrode
1kΩ
1MΩ
I→V
Vbias
high B.W. current amp
ref: 2f2
in
DC out
LIA 1
Au surface oscillation amplitude, phase
Vdrive
high freq sweep, f2
Vexcite
low freq, f1
ref: 2f2
in
DC out
LIA 2
V differential
ref: f1
in
DC out
LIA 3
Sample resistance change to Au oscillation

Figure 4·7: High frequency detection circuit. The cryostat is held at a constant temperature just below T_c on the slope of the transition. The high frequency V_{drive} signal is applied to the drive electrode and swept at frequency f_2. The plate then feels an electrostatic force at frequency $2f_2$. The amplitude of the plate is monitored by measuring the AC current going through the sense electrode using a current-to-voltage amplifier and a lock-in referenced to $2f_2$ (LIA 1). The voltage drop across the Pb sample is also being detected at $2f_2$. If there is any change in T_c due to the Casimir cavity size, this is the frequency it would occur at. Because the excitation current, I_{ex}, is cycling at f_1, the DC output of LIA 2 is fed into a third lock-in, LIA 3, which is referenced at f_1.

4.5 Results and discussion

4.5.1 Superconducting transition of quench condensed Pb film

The micro-sources are heated according to the methods explained above, and a thin Pb film forms in a ‘H’ shape, connecting the leads and allowing a 4-point resistance

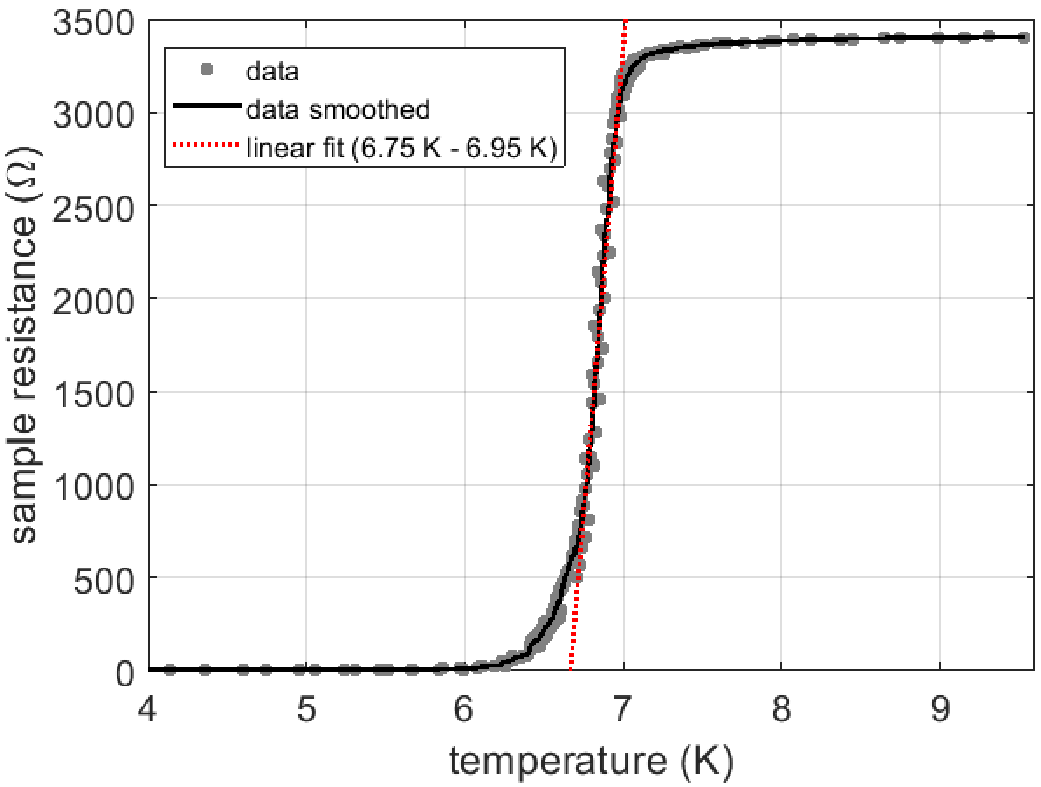

Figure 4·8: Superconducting transition of the quench condensed Pb film. Data points (gray dots) are taken both sweeping up and down through the transition and the black line is a smoothed average of these data points. The slope of the transition is calculated to be 10 kΩ/K and the steepest point is at 6.88 K.

measurement to be made using the circuit shown in figure 4·6 with $V_{\text{excite}} = 5\,\text{mV}$ at 37.7 Hz. The temperature is swept from 4 K to 9.5 K and back down. This data is plotted in figure 4·8. The temperature at which the Pb film begins to condense into the superconducting phase is 7.05 K, just under the bulk value of 7.162 K indicating a thicker film (likely around 20 nm [Imboden et al., 2017]). The resistance of the film above T_c is 3.4 kΩ and the slope of the transition is 10 kΩ/K.

4.5.2 Plate mechanics

To measure the motion of the plate, a detection circuit is used in which the current between the grounded Au plate and e_{sense} is monitored as a constant AC voltage is applied to e_{drive} and swept in frequency (see figure 4·7). At room temperature, plate resonance is typically measured to be 690 kHz and at low temperature the resonance (before depositing Pb) is typically 1.8 MHz. This implies significant changes in stress going on in the cavity as the device is cooled. Because the structure is a suspended Au film anchored on its sides by silicon dioxide, the different coefficients of thermal expansion of the two materials greatly change its internal stresses. Although the resonance and therefore stiffness are different between room temperature and cryogenic temperature, the amplitude of oscillation can still be determined from the amplitude of the sense electrode signal and an accurate estimate of the plate position can be determined upon observing contact with the oxide stops (see appendix B.2.2).

DC actuation and temperature sweeps

In these experiments, a DC voltage is applied to the sense electrode and drive electrode from 0 V to 4 V and sweeping the temperature across the superconducting transition. Meanwhile, a current is being applied through the sample and the voltage drop is measured according to the configuration in figure 4·6. V_{excite} is set to 1 mV and is purely AC at 37.7 Hz. V_{diff} is measured with a lock-in amplifier at 37.7 Hz then converted to a resistance by considering a simple voltage divider circuit between the sample and the external resistance of 1.001 MΩ. The advantage of this method is that the full transition curve can be mapped out, so features like slope, and T_c can be extracted, which were measured to be 2.5 kΩ/K and 6.88 K respectively. When the excitation voltage is increased to 5 mV the slope of the transition is measured to be 10 kΩ/K As we can see in figure 4·10, it was observed that varying the DC bias on

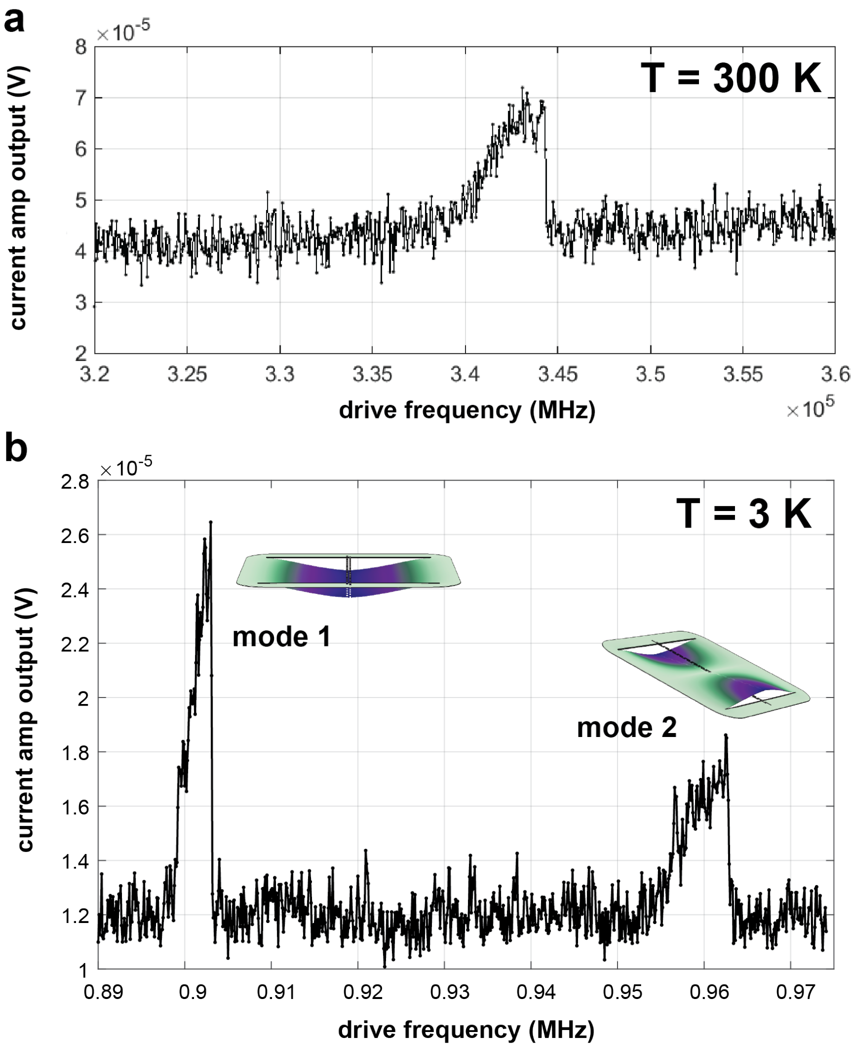

Figure 4·9: Resonant response of movable Au plate. **a**. Plate resonance at room temperature. **b.** Plate resonance (and second mode) at 3 K. In both figures, the y-axis is the amplitude of current (scaled by $20\,\mu\mathrm{A\,V^{-1}}$) at the sense electrode (at twice the drive frequency). This signal is proportional to plate position, indicating typical spring hardening non-linearity. The resonant frequencies of the fundamental mode of plate at room temperature and low temperature are 690 kHz and 1.8 MHz respectively.

the electrodes has no measurable affect on these values however.

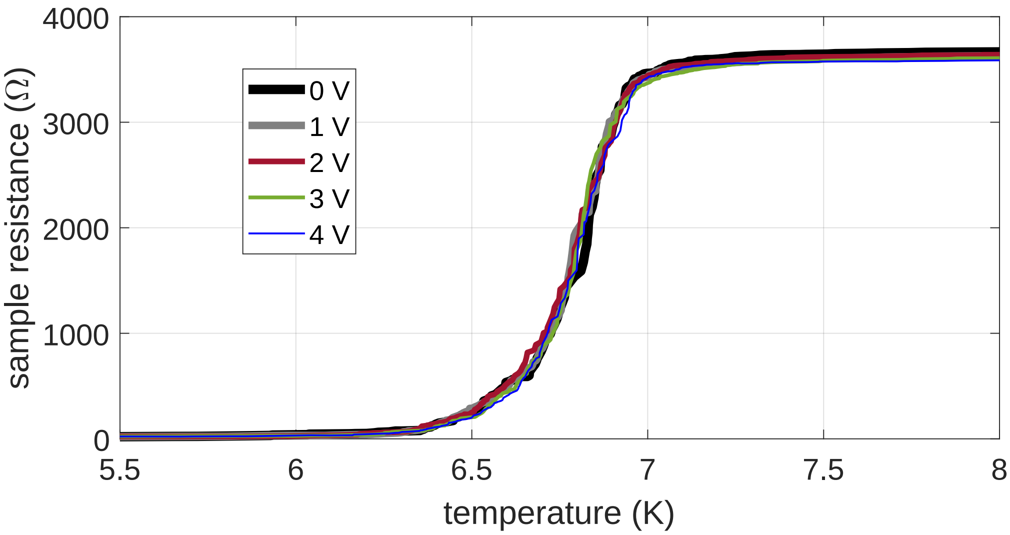

Figure 4·10: Quench condensed Pb film transition at different plate bias voltages.

4.5.3 High frequency detection of T_c shift

This detection method is inherently higher resolution due to its high frequency. Additionally, detecting *only* the component of the voltage drop across the sample at the same frequency means that our measurement is only sensitive to the effect we are looking for. Plotted in figure 4·11 are three trials using this detection method, Trial 1, Trial 2, and Trial 3. In Trial 3, the scan stops just after the frequency jump of the plate however a few useful data points are still obtained. The voltage difference measurement is scaled to resistance by I_{ex} and then into units of temperature change based on the slope of the transition. One data point is taken every 90 s. The time constants on LIA 1 and LIA 3 are set to 30 s but the time constant on LIA 2, where the differential voltage measurement is detected, is set to 10 ms in order to resolve the 37.7 Hz modulation of the high frequency signal, which is occurring due to the AC excitation frequency. The frequency values in the x-axis of these plots refer to the

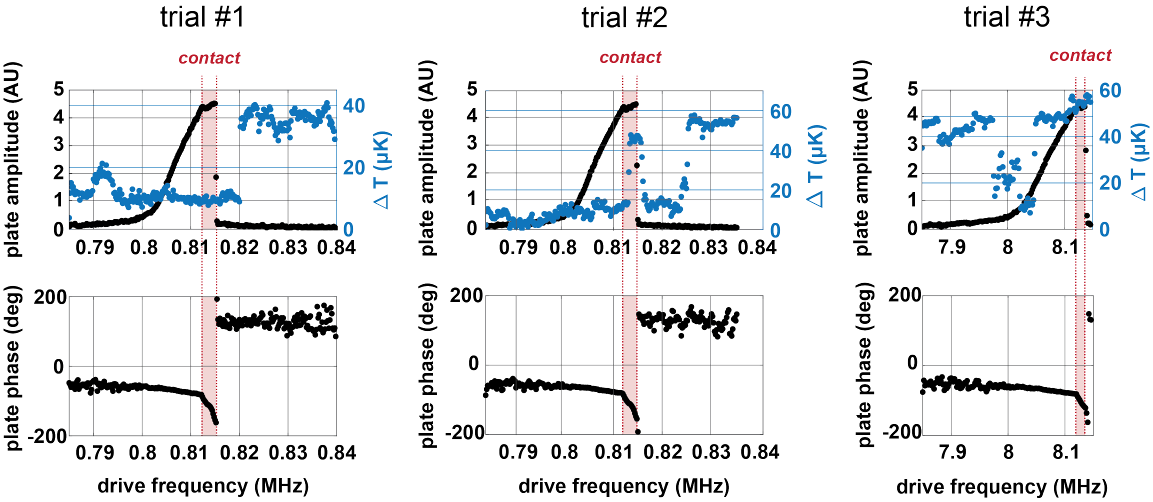

Figure 4·11: High frequency detection of superconducting Pb film and cavity size. Here, any changes in resistance are scaled to units of temperature change using the slope of the superconducting transition. Note that $\Delta T = 0$ is arbitrary from plot to plot. The regions where the plate is reaching contact with the oxide stops are highlighted in red.

frequency of the signal being applied at the drive electrode, so the plate is actually moving at twice this value. In these experiments, we also monitor the temperature of the cold finger of the cryostat (measured by an internal thermometer) as well as the temperature of the room of our apparatus (measured by a calibrated resistance temperature detector). The room temperature may have some influence the excitation current (because of the temperature dependence of the external resistors) so this measurement is useful to log as well.

Also plotted in figure 4·12 is the same data as figure 4·11 but zoomed in to the region of interest (where the amplitude drops). In addition to plotting the data points, we include two sliding average curves to help visualize trends in the noisy data. For each point, x_i, the sliding average value for a given integer n is just:

$$S_i(n) = \frac{1}{2n+1} \sum_{j=-n}^{n} x_{i+j} \tag{4.5}$$

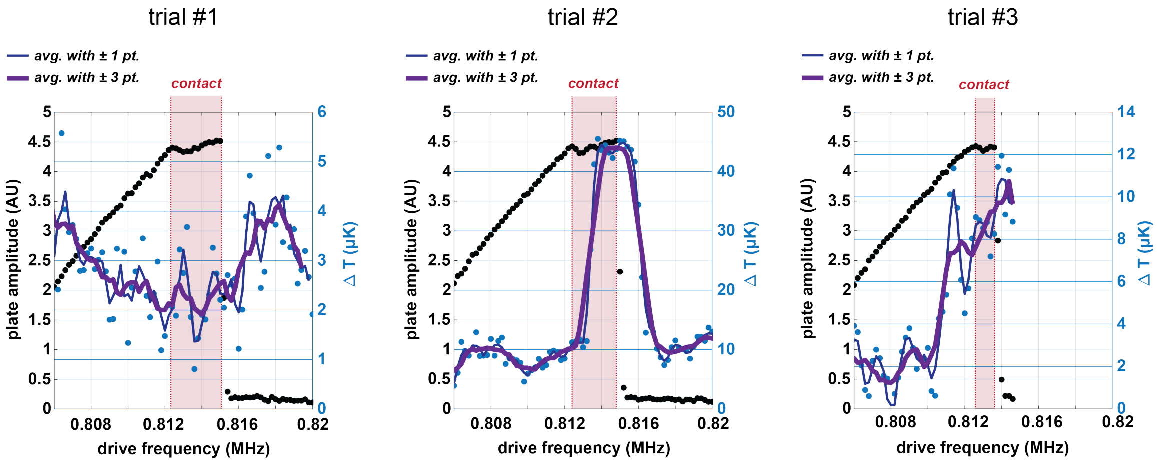

Figure 4·12: A closer look at high frequency results. Only the regions before, during, and after contact are plotted. Note the differing scales of ΔT between trials due to measurement instabilities. In addition to data points, sliding averages are plotted with $n = 1$ (thin line) and $n = 3$ (thick line).

4.5.4 Discussion of results

Two different experiments are done to measure the resistance of the superconducting Pb film as the cavity size is changed. In the first set of experiments, a full temperature sweep is made at different static plate positions. The plate is actuated by applying a DC bias to the electrodes between 0 V and 4 V. This results in a maximum plate deflection of only a few nanometers at 4 V (see appendix B.2). Any voltages above this value risk shorting between bonding pads on the device. Given that the nominal gap between the sample and the plate is around 260 nm, it is unlikely that any Casimir induced changes from this small displacement would be large enough to measure.

Additionally, because the resistance of the sample is being measured at essentially DC

(37.7 Hz) it is prone to low frequency fluctuations in temperature. The main source of this unwanted noise is actually due to the cyclic pumping of the closed-cycle cryostat, and results in ±0.1 K fluctuations at around 1 Hz. These fluctuations can be averaged out with sufficiently long time constants on the resistance measurement, however the maximum temperature resolution with this scheme is still a few mK.

The AC method involves using the natural resonance of the plate to detect changes in the sample resistance at the frequency of the plate. One interesting point to note is that the resonant frequency has shifted down by roughly 170 kHz due to the added mass from the deposited Pb (see figure 4·9 for pre-deposition dynamics). In this set of experiments, the temperature of the cryostat is set to the steepest part of the transition (6.88 K) and three long sweeps are made driving the plate to resonance from low to high frequency until it abruptly loses amplitude. An important feature in the plate response is the evidence in all three trials of a sudden change in the amplitude and phase behavior occurring at around 811.2 kHz. This is due to the onset of some new interaction with the plate, which we believe is indication of contact with the oxide stops. Any additional non-linearities in the plate mechanics due to deformation alone would not appear in this manner, but instead would be gradual. Also, the amplitude is nearly fixed beyond this point, which is further indication of contact. Because the drive is large however, the oscillations into contact are still stable, so the 90° phase shift before the jump is still reached.

So, to interpret these results in terms of real displacement, the plate likely reaches a minimum separation of between 80 nm and 100 nm when in contact with the oxide stops (see analysis in appendix B.2.2). Then, when the jump occurs around 815 kHz, the separation abruptly increases from this spacing to the initial gap size–

about 260 nm. This large and sudden change in gap size is where we might expect to see a shift in the sample resistance if there were indeed a dependence of the superconducting transition temperature on the cavity size.

Another feature of the high frequency results are seemingly random jumps of 30 - 40 µK. We are not sure what the origin of these instabilities are, however based on analyzing the three trials, we do not believe it is anything related to the plate position. For example, in trial #1, we observe a large displacement at 820 kHz, which is well after the large plate oscillations have ceased. In trial #2, there is a large jump that is interestingly close to the contact range, but a closer inspection of the data in figure 4·12 shows that it lags the plate contact by 5 or 6 points (corresponding to 7.7 - 9 min), which is impossible for the effect we are looking for. Finally, in trial #3, the ΔT measurement seems to be tracking the plate amplitude, but then after the oscillations jump down, the signal does not follow.

In all three trials, no clear correlation between plate amplitude and transition temperature is observed within a resolution of 5 µK both during the slow approach where the plate finally reaches just under 100 nm of separation, and during abrupt jump where the plate amplitude drops to 260 nm separation. There are a few reasons which may explain this null result. No observation of this effect may be due to one or more of the following reasons: device limitations, superconductor limitations, or lack of parallel magnetic field.

Firstly, the device geometry may not allow for a small enough cavity to observe a shift. The minimum cavity size we are able to achieve with this system is just under 100 nm. Furthermore, the patterning of the shadow mask results in an interacting area between the Au and Pb that more closely resembles two parallel wires, rather than two parallel plates. These geometrical limitations, as evidenced simply by equation 2.2 (small A and large d), likely produce a small shift if any.

Regarding the superconducting film itself, there are certain key material properties to consider when conducting this type of experiment. First of all, a low T_c value is generally desired because the condensation energy, $\varepsilon_{\mathrm{cond}}$ goes as $T_c^{2.6}$ [Lewis, 1956]. It is the ratio of the Casimir free energy to the condensation energy that determines the magnitude of the shift in critical field, so generally speaking, the lower T_c the better. In the case of the experiment presented here, Pb has a relatively high T_c value, but was chosen for other experimental advantages. Future work may involve investigating lower T_c materials. One caveat to this point however, is that some low T_c type I superconductors, such as Beryllium, are actually found to have an *increased* T_c for thin films [Adams et al., 1998], which is opposite to what is observed in Pb. Another important material property is the plasma frequency. Bimonte et al. show that high plasma frequency materials can change the strength of the Casimir free energy term by almost one order of magnitude [Bimonte et al., 2005c]. Many of the calculations in their work assume Be, which has a plasma frequency of around 18 eV compared to Pb which has a value of roughly 8 eV [Ordal et al., 1985].

Finally, there is the question of what we expect theoretically in the limit of zero applied field. As discussed previously in section 2.3.2, the theory behind this experiment is for shifts in parallel critical field, not critical temperature. Because of the methods used for the calculations, in the low field, it is not exactly clear what one might expect the critical temperature to do when the Casimir cavity varies. What our experiment shows is that for our geometry, materials, and in the range of temperatures we can resolve, it does nothing. Most certainly, the next step in this project will be to include magnetic characterization as well as thermal. Including coils in the setup would allow for critical field shifts to be measured, and perhaps an experimental result that can be more directly compared to theory will be obtained.

Chapter 5

Related MEMS Projects

5.1 Micro-gluing enabled devices

In order to realize the modified accelerometer device discussed in chapter 3, techniques were developed to carefully place and glue micro-sized objects onto the post-release MEMS (discussed in section 3.3). This micro-gluing methodology is not just limited to Casimir force devices, however, and has in fact led to some other sensing devices currently being developed and researched.

5.1.1 Gradient magnetometer

Device concept and fabrication

An accelerometer senses external accelerations applied to the body of the device by means of a physical displacement of the proof-mass. However, if one ignores inertial forces and instead directly, mechanically couples an external force to the proof-mass, that force will also be sensed by the device. This idea was used for the Casimir force measurement device, and it also applies here. By gluing a permanent magnet to an ADXL203 proof-mass, we can sense any force applied to that magnet, i.e. gather information about the magnetic field of the environment. In these devices, the direction of magnetization of the micro-magnets is aligned with either the X or Y sensing axis of the accelerometer.

Approximating the magnet as a dipole moment, $\vec{\boldsymbol{\mu}}$, an external field, $\vec{\boldsymbol{B}}$ will pro-

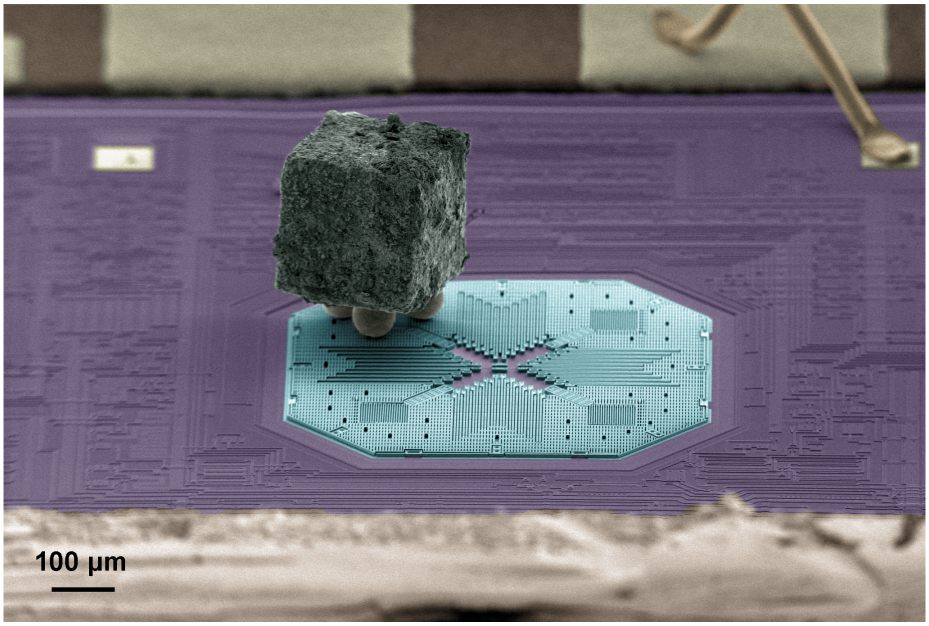

Figure 5·1: SEM image of an ADXL203 accelerometer re-purposed into a magnetometer. The moment of the magnet is aligned along one of the sensing directions of the accelerometer and rigidly attached to the proof-mass (blue) by using three micro-spheres as supports.

duce both a torque and a force on the moment, given respectively by:

$$\tau = \vec{\boldsymbol{\mu}} \times \vec{\boldsymbol{B}} \tag{5.1}$$

$$F = \nabla \left(\vec{\boldsymbol{\mu}} \cdot \vec{\boldsymbol{B}} \right) \tag{5.2}$$

Because the ADXL203s are designed to be sensitive to linear motion, not rotation, a magnetometer device like the one shown in figure 5·1 will be inherently a gradient field sensor. Its output is proportional to the gradient (along the direction of the magnet) of an external magnetic field.

Modifying an accelerometer to become a gradient magnetometer involves several of same techniques as building the Casimir force sensor. Based off of the assembly of the prototype device shown in figure 5·1, a fabrication process for assembling the micro-objects required to achieve a robust, highly sensitive gradient magnetometer has since been developed [Javor et al., 2019]. This process, developed by Josh Javor at Boston University, is shown in figure 5·2. First, four individual microspheres are glued with UV curable epoxy onto a platform designed to fit onto the ADXL203 proof-mass. Next, this platform is flipped over so it is resting on the four support spheres. By pulling vacuum through an angled micro-pipette, a permanent micro-magnet (NdBFe N52 grade) can be picked up, dipped in UV curable glue, and placed onto the center of the platform. After curing the glue, the magnet is again picked up and the whole assembly is glued with the same UV epoxy onto the proof-mass of the accelerometer. Continuously monitoring the output of the sensor provides feedback for this attachment process, indicating the moment the spheres have contacted the proof-mass.

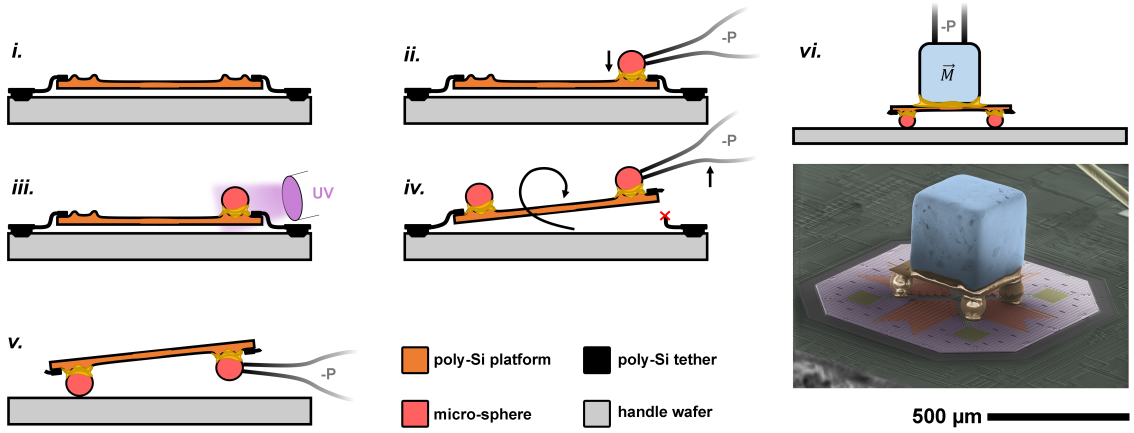

Figure 5·2: Assembly process for MEMS gradient magnetometer. **i.** custom-made suspended poly-silicon platforms with tethers are fabricated. **ii.** using UV epoxy and pick-and-place, micro-spheres are positioned onto dedicated locations on the platform and cured in place (**iii.**). **iv.-v.** platform is picked up with vacuum and flipped over. **vi.** micro-magnet is glued onto top of platform and then the whole assembly is placed onto ADXL203 proof-mass (inset SEM image).

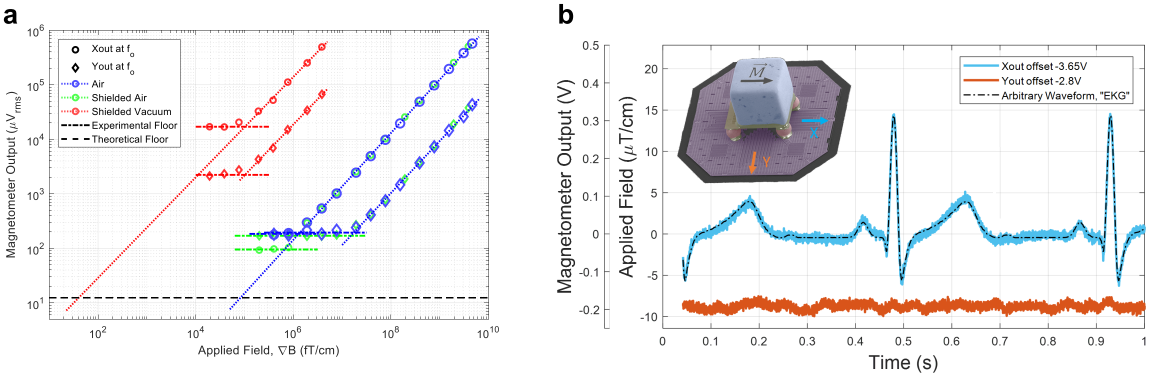

Figure 5·3: MEMS gradient magnetometer performance. **a.** plot of sensor output amplitude versus magnetic field gradient amplitude. Each data point is taken by driving the MEMS device to its mechanical resonance with an AC magnetic field. **b.** Raw sensor output in response to an arbitrary magnetic field waveform resembling an electrocardiogram signal. Near perfect tracking is achieved in the sensing direction (X) with essentially no cross-talk along the Y direction.

Characterization of this device is done by placing the device equidistant and along the axis of two sets of coils in an anti-parallel configuration. In this arrangement, the uniform field magnitude is zero at the center but the field gradient is maximum. Then, the current through the coils can be driven to apply a translational force on the magnet. Measurements are made in air, in air with magnetic shielding, and in vacuum with magnetic shielding.

Device performance and applications

Figure 5·3 shows data taken with one of the devices assembled using the process shown in figure 5·2. When driven at its mechanical resonance, the sensor can resolve magnetic field gradients down to 1.05 $\mathrm{nT\,cm^{-1}}$, 700 $\mathrm{pT\,cm^{-1}}$, and 100 $\mathrm{pT\,cm^{-1}}$ in air, air with magnetic shielding, and vacuum with magnetic shielding respectively. To put these values into perspective, the magnetic field gradients produced by the human heart and brain are around 100 $\mathrm{pT\,cm^{-1}}$ and 200 $\mathrm{fT\,cm^{-1}}$ respectively. Currently, these types of biomagnetic measurements are made with superconducting quantum interference devices (SQUIDs), which are high cost, large, and require a relatively large amount of power to run, due to the requirement for low temperatures. Additionally, SQUIDs and other advanced magnetic sensing devices will pick up uniform magnetic fields, including earth's field, which is always present. This can severely limit resolution if the measurement is not done in a heavily shielded room. Because the MEMS device presented here is much more sensitive in a linear direction than rotationally, it is inherently less responsive to these uniform fields.

The performance of the MEMS gradient magnetometer is remarkable, considering its footprint, cost, and room temperature operation. Improvements to this device are currently being made, but in theory, its sensitivity could be able to compete with the current state-of-the-art technologies and potentially be integrated into cheap, wearable medical devices.

5.1.2 Large angle micro-mirror

Device concept and fabrication

In this project, the methods developed for pick-and-placing micro-objects onto post-release MEMS (described in 3.3 and 5.1.1) are used to build a magnetically actuated micro-mirror [Pollock et al., 2019b]. Compared to commonly used actuation forces in MEMS devices (electrothermal, electrostatic, e.g.), magnetic forces can be relatively large–especially on permanent NdFeB magnets with very high magnetic moments. Using such a high force allows for very large range, very fast driving of a compliant poly-silicon platform.

The structure of this device can be seen in the colorized SEM images in figures 5·4**a** and 5·4**b** along with a schematic for how it is actuated in figure 5·4**c**. The micro-magnet (aligned vertically) is glued on top of a circular poly-silicon platform which is raised a few hundred µm off of the substrate with four bimorphs. Each bimporh

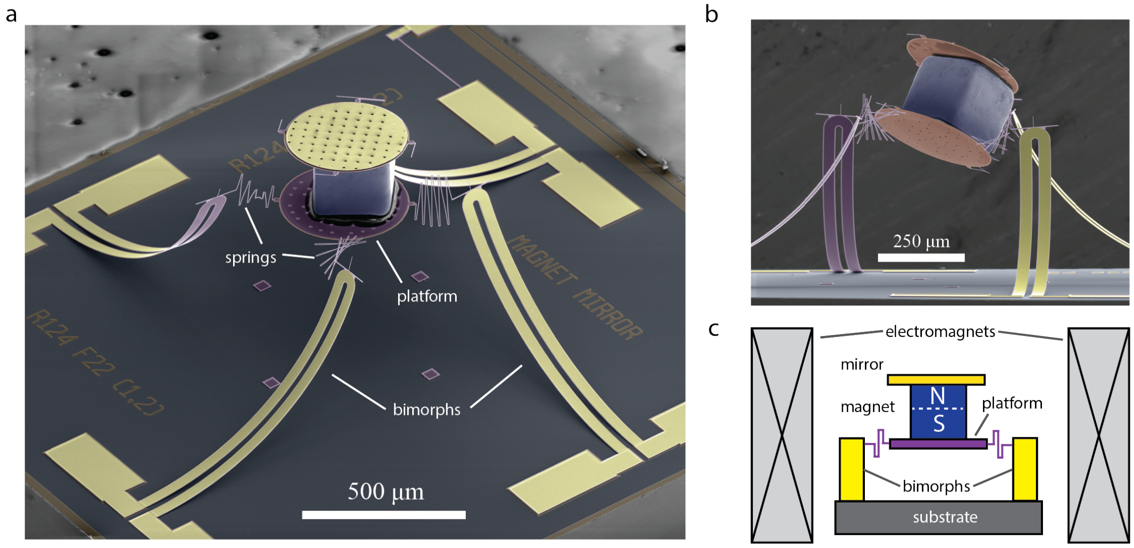
a
springs
platform
bimorphs
R124
MAGNET MIRROR
R124 F22 (1,2)
500 µm
b
250 µm
c
electromagnets
mirror
magnet
N
S
platform
bimorphs
substrate

Figure 5·4: Magnetically driven micro-mirror

obtains this extreme curvature due to the two-layer stack of materials they consist of: poly-silicon and Au. Because the Au is evaporated onto the poly-silicon at a high temperature, as it solidifies and cools to room temperature, it contracts more than the poly-silicon it is adhered to due to their different coefficients of thermal expansion. This residual tensile stress causes the bimorph structures to bend upwards when the devices are released. Each bimorph is then connected to the platform with a thin serpentine spring. It is the combination of raised initial height, soft spring constants, and large magnetic forces, that allow this magnet to be actuated to such large angles. The final component is a Au-coated poly-silicon mirror that is glued on top of the magnet for an optically reflective top surface.

The magnet (and therefore mirror) is actuated in the radial and azimuthal directions by controlling the current going through two sets of coils, an 'X' directed pair, and a 'Y' directed pair (where X and Y are the cardinal axes in the plane of the die). A finite element simulation of how the magnet is steered can be seen in figure 5·5.

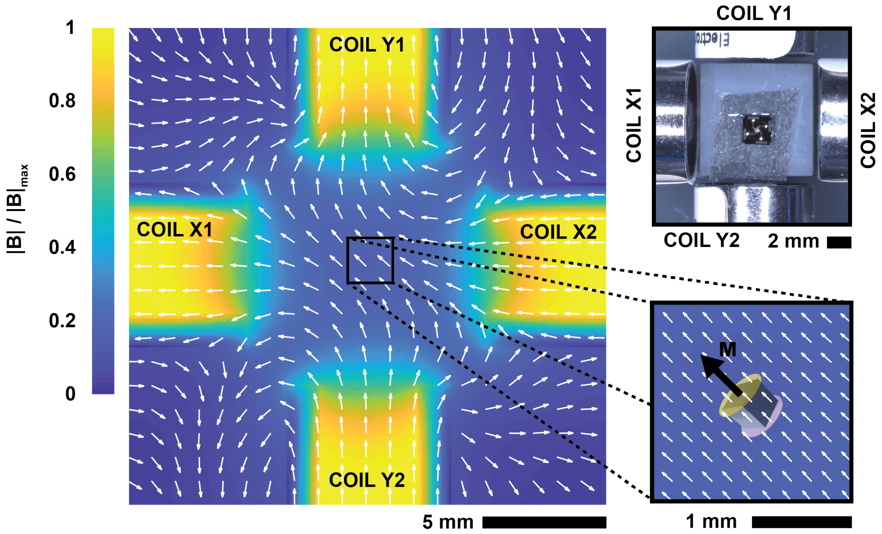

Figure 5·5: Steering the magnetically actuated micro-mirror. In the finite element plot, the relative magnetic field strength is indicated by the colorbar and the direction of the field is indicated by the arrows. In this example, the X and Y coils are both set to the same current, so a diagonal field is produced. The zoomed in plot also shows how a vertically aligned magnet would rotate in such a field. The top right image is the actual setup with the die in the center and 4 coils on each side.

This figure plots the magnetic field vectors in the X and Y directions from a top-down view of the device. As long as the X pairs have the same current ($I_{X1} = I_{X2}$), and the Y pairs have the same current ($I_{Y1} = I_{Y2}$), the field in the center will uniform (i.e. have zero spatial gradient). By adjusting the relative magnitudes of the X and Y currents, we can rotate the direction of the magnetic field and steer the magnet. Although the field strength varies close to the coils, in the center, where the device is, it is very uniform.

If we consider one dimension of rotation, the tilt angle, θ (azimuthal direction), of the platform can be approximated by assuming a linear rotational spring and magnetic torque balancing each other. The spring constant is defined by the stiffness of the springs, and is linear with θ. The torque is defined by the cross product of the

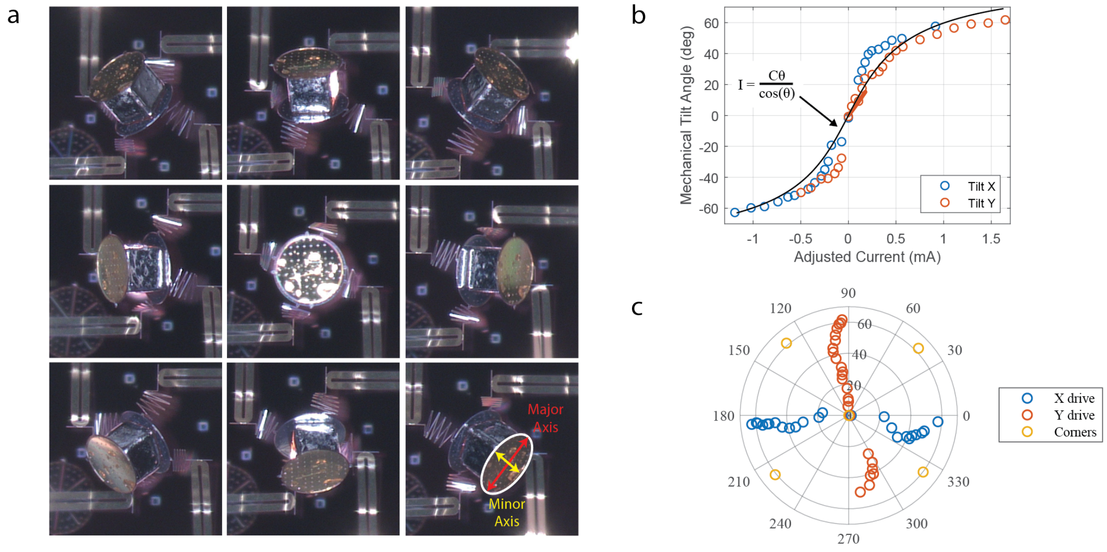

Figure 5·6: Magnetically driven micro-mirror range results. **a**. Top-down optical microscope images of the mirror driven over several angular positions. **b**. Azimuthal tilt angle versus drive current. **c**. Azimuthal tilt and rotation for X drive only, Y drive only, and combinations of maximum X,Y.

magnetic moment with the magnetic field vector (see equation 5.1). This torque will then scale as $I\cos(\theta)$ where I is the applied current through the coils. Equating the torque with the spring restoring force, we find:

$$I \propto \frac{\theta}{\cos\theta} \tag{5.3}$$

Device performance and applications

By simply changing the currents through the X and Y coils, we can steer the mirror over a radial range of 360° and an azimuthal range of ± 60°. Figure 5·6**a** contains several top-down microscope images displaying this range, with corresponding angular measurements in figures 5·6**b** and 5·6**c**.

Reaching ±60° of mechanical angle is significant because it corresponds to ±120° of optical angle (if one considers an incident beam coming down on the mirror from directly above the device). This means one could direct a laser to cover an entire hemisphere (and more) with this mirror. This would have significant technological advantages in imaging, optical communication (allowing for more routing paths for beams) and LIDAR (by being to map out the environment in front and around the sensor).

5.2 MEMS drive techniques

5.2.1 Open loop driving for fast step-and-settle times

In MEMS actuators there is often a trade-off between actuation range and settling time. Settling time is directly related to the amount of damping in the system (see section 2.4.1). For many actuators, a short settling time is desired. However, the more damping is present in a system, the more force is required to move it from one point to another. Engineers will often design a system which is some bargain between the two. However, as we show in the following work, it is possible to reshape the impulse of the driving force to reduce this settling time and get the system to move from point **A** to point **B** much much faster than the ring down time defined by $1/\lambda$ [Imboden et al., 2016, Pollock et al., 2018].

In this section, we only consider one-sided driving, which is often found in most MEMS systems. This means when we apply a force to our MEMS, it is only in one direction (this would be the case for parallel plate electrostatic actuation for example). In this system, we have control over how fast moves *towards* our desired equilibrium point (from **A** to **B**), but not how fast it slows down to reach there. In this case, we must anticipate the deceleration of the system due to damping and restoring spring force such that the mass is no longer in motion when it reaches point **B**. In the limit of zero damping, this is a simple problem: how much force should we apply to our mass such that it reaches our desired equilibrium point with zero velocity? The answer is

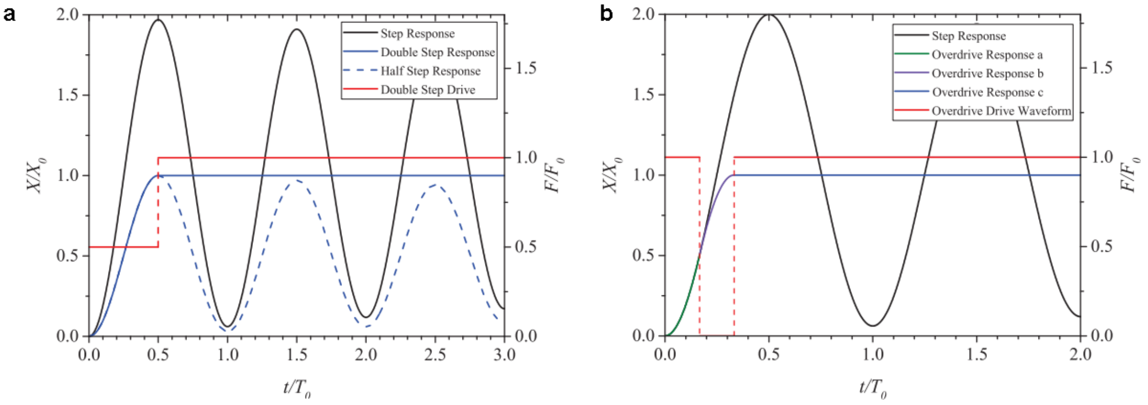

Figure 5·7: Simulations of under-damped system response to one-sided advanced drive pulses. **a.** double-step pulse technique moving the mass from 0 to X_0. **b.** single-step pulse technique for moving the mass from 0 to X_0.

half of whatever force it needs to get to **B**. To see why this is the case, we can refer to figure 5·7**a**. We see that driving the mass with half of the final force (red pulse) will cause the mass to overshoot, and then stop at exactly the position we want it to be in, with zero velocity. If at this moment the force is then switched to the full amount, the mass will remain in place with no ringing. This means that we will have moved and settled an under-damped system to a new position in time time of one-half of a period.

Such a driving method requires that we have some way of controlling the magnitude force in an analog way on the driven mass. If, say, we only have a 'digital' driving force, on or off, the timing is slightly different. In this scenario, shown in figure 5·7**b**, the full force is turned on for $1/6^{\text{th}}$ of a period, then turned off for another $1/6^{\text{th}}$ of a period. After this total of $1/3^{\text{rd}}$ of a period, the mass will have reached the desired position and will have zero velocity. Further discussion of the theory behind this model can be found in [Imboden et al., 2016].

Depending on how under-damped a MEMS system is, a typical response to a step input may involve ring down over hundreds or even thousands of oscillations, so cutting this down to 1/2 or 1/3 of a period is significant. For example, the magnetically actuated micro-mirror presented in section 5.1.2 takes 1.35 s to ring down to 2 % of the final position with a simple step input. Using a one-sided advanced driving pulse, we can move and settle it in 4.5 ms.

5.2.2 Pulse width modulation for analog positioning

Pulse width modulation is a technique seen in many electronic drive systems which involves varying the duty cycle of a square wave–that is, the percentage of the period of the signal at which it is on versus off. PWM is a convenient way of producing a psuedo-analog signal from a digital one. To see why this is so, let's examine the following square wave shown in figure 5·8.

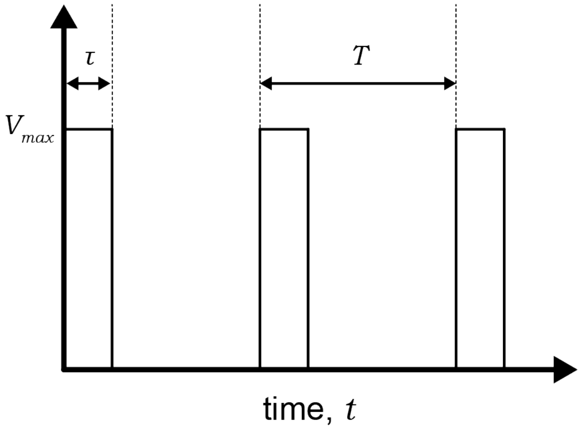

Figure 5·8: Plot of a typical PWM signal. The duty cycle is equal to τ/T and the frequency is $1/T$.

In figure 5·8 we have a square wave that goes from 0 to $V_{\max}$, with a period of T and a duty cycle given by τ/T. The Fourier series for this waveform can be written as:

$$V(t) = V_0\frac{\tau}{T} + V_0\sum_{n=1}^{\infty}\frac{2}{n\pi}\sin\left(n\pi\frac{\tau}{T}\right)\cos\left(\frac{2n\pi}{T}t\right) \tag{5.4}$$

In equation 5.4 we see a leading static term followed by an infinite series of harmonics that sum to create the sharp edges of our pulses. The lowest frequency in this series (when $n = 1$) is $1/T$, or the same frequency as the square wave, which makes sense. To isolate the leading static term from this square wave, one simply needs to filter out these higher harmonics. Then, the value of that static term can be adjusted by simply varying the duty cycle of the square wave. This is the essence of PWM–in any linear system that is too slow to respond to the frequency of the PWM wave, the alternating PWM input will act as if it is a constant signal. The value of this constant signal is then linearly proportional to the duty cycle.

PWM control can be found in thermal systems, electrical systems, and lighting. An under-used application however, is in MEMS. A convenient system to use for this study is the ADXL203 accelerometer from Analog Devices–the same device used in the work described in chapter 3. These devices have a digital input pin known as "self-test" which will applies a constant electrostatic force to the proof-mass when above a certain threshold (around 2.5 V). If the pin is above that threshold, a DC force is applied, moving the proof-mass. This feature is intended to be a simple check that the device is functioning properly, but as shown below, it can also be used to demonstrate PWM analog driving of MEMS [Pollock et al., 2018] and to even enhance the range of the sensor.

Because the self-test pin is digital, we can use it to apply force to the proof-mass in a digital manner (i.e. either high or low). In order for a PWM signal to appear like a constant force on the proof-mass, the frequency needs to be much faster than the mechanics of the MEMS can respond. If we call the position of the proof-mass with self-test off **A** and the position of the proof-mass with the self-test pin high **B**, high

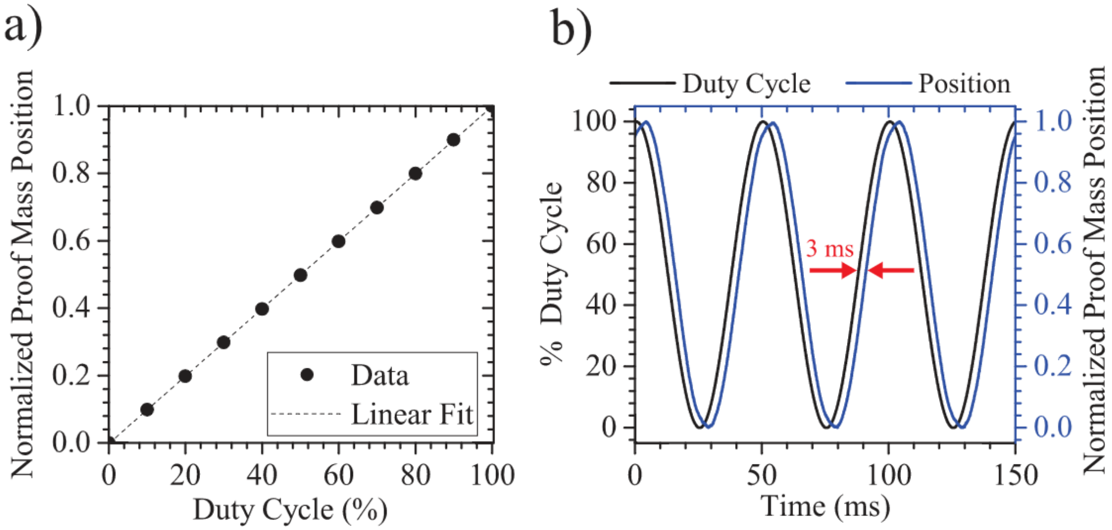

Figure 5·9: PWM enabled analog positioning of an accelerometer. **a.** Proof-mass position versus PWM wave duty cycle. **b.** A sinusoidally varied duty cycle is used to drive the accelerometer at 20 Hz.

frequency PWM driving allows us to position the proof-mass anywhere in between points **A** and **B** by simply varying the duty cycle. Some results of this are shown in figures 5·9**a** and 5·9**b**.

PWM can also be used when an analog method of driving already exists, but it's not linear. For example, let us consider a parallel plate capacitor on a spring. Schematically, this will look exactly like the accelerometer shown in figure 2·9 but instead of a sensor, we are interested in positioning the movable mass by applying a voltage between the plates, V. As mentioned in section 2·10, the force scales as V^2/d. The position of the mass is then:

$$x(V) = \frac{\varepsilon_0 A V^2}{d} \tag{5.5}$$

Of course, d is itself a function of x, and as x becomes larger, the effective spring constant of the system will go to zero leading to an instability causing the plate to pull-in [Zhang et al., 2014]. However, for $x \ll d$, we can assume the force is

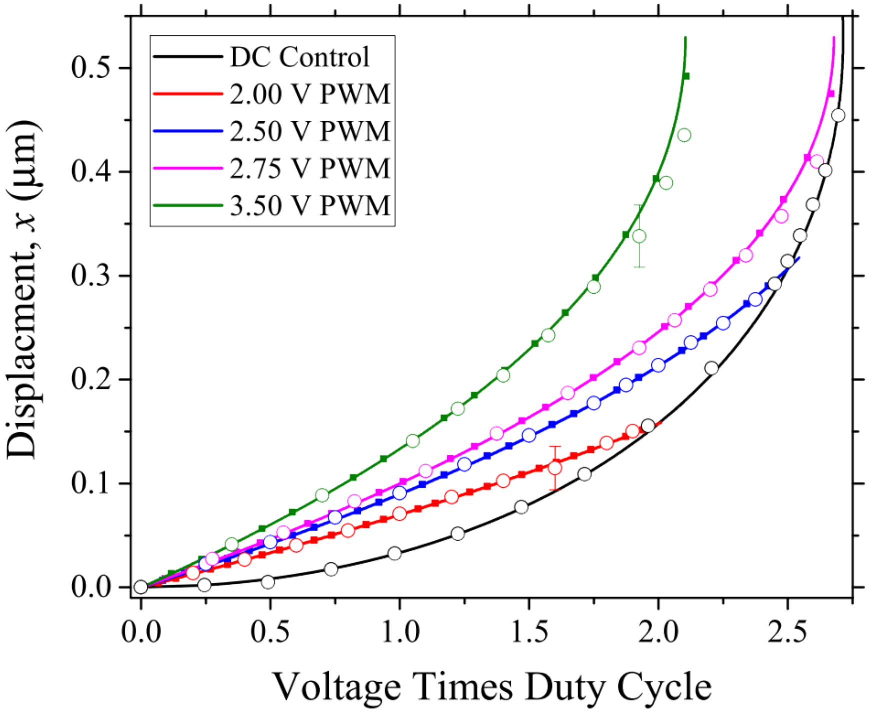

Figure 5·10: Comparison of DC voltage control (black) with PWM control at different pulse hights in a parallel plate system.

linear, and x simply scales as V^2. Therefore, if one wanted to position the plate in an accurate manner, the corresponding analog voltage would need to be applied between the plates according to equation 5.5. Generally speaking, the precision of the positioning is set by the precision of the applied analog voltage. If instead we replace the static voltage with a high frequency PWM signal, this required precision in voltage amplitude is replaced by precision in pulse timing [Pollock et al., 2019a]. There is also the added benefit of linearization of the forcing–that is, changing the input (duty cycle) by a factor of two for example, will change the output (position) of the system by a factor of 2, which is not the case for the $x \propto V^2$ method of driving. In figure 5·10 we plot the response of a parallel plate capacitor on a spring driven with both an analog voltage (black curve) and by PWM signals of varying pulse heights (red, blue, pink, and green curves).

It is evident from figure 5·10 that the PWM drive effectively linearizes the positioning of the system. When the duty cycle is equal to 100 %, the position is the same as it would be for DC voltage control with $V = V_{\text{pulse height}}$. In this sytem, electrostatic pull-in occurs at around 2.7 V, so only PWM drives whose pulse height is less than that value (red and blue curves) will be linear across the whole range. It is possible to use pulse heights larger than the pull-in voltage, but the linear range will only occur for smaller duty cycle values (as seen in the pink and green curves).

The great advantage of this method is that the problem of precise positioning comes down to precise, high-speed timing, rather than precise, analog voltage control. In modern digital circuitry, the former is a much easier and cheaper problem to solve. This methodology was implemented in a commercial MEMS deformable mirror device (BMC MultiDM) built by Boston Micromachines Corporation. A high speed switching circuit was built to produce high speed, high voltage digital pulses whose duty cycle could be varied. The difference in cost between the original analog circuitry and the PWM circuit was estimated to be $980 [Pollock et al., 2019a].

Chapter 6

Conclusions and future outlook

6.1 Summary of Casimir force measurement with a commercial MEMS sensor

In chapter 3, a commercial MEMS accelerometer was modified to perform a measurement of the Casimir force between a Ag-coated microsphere and a Au-coated plate. In order to do this, a feedback-enabled pick-and-place system was developed to assemble micro-scale objects onto the post-release proof-mass of the accelerometer. The required components of this assembly were a smooth, Ag-coated microsphere and a very soft, electrically conducting wire in order to cancel out unwanted residual potential on the sphere. The Au-coated plate was then positioned near the sphere with piezoelectric actuators in order to control the separation between the two surfaces.

First, a force calibration of this device was performed in which a known electrostatic force was applied between the sphere and the plate and the voltage was varied. This was repeated over a range of sphere-plate separations. This calibration was used to determine the sensitivity of the device and also to find the bias which would cancel out the residual potential between the two surfaces.

Next, ensuring that the system was properly biased, the plate was stepped carefully towards the sphere and the remaining force on the sphere was measured. This data was fit to the theory for the Casimir force in this system with only the initial separation as a free parameter. The results agreed excellently with theory, resulting in a root mean squared error of just 7.4 pN.

The importance of this work is that it showed it is possible to perform highly sensitive quantum metrology in ambient conditions with off-the-shelf consumer MEMS sensors, which are widely available and very inexpensive. Once functionalized, these devices can be used as a novel tool for experimenters—a literal platform capable of performing a variety of interesting micro- and nanoscale low-force experiments. Using the feedback-assisted micro-gluing process we have developed, one can re-purpose the sensor to transduce any measurand that can be coupled into a displacement of the proof-mass.

The micro-gluing work developed for this project also enabled the creation of two other MEMS devices: a gradient magnetometer capable of measuring down to $100\,\mathrm{pT\,cm^{-1}}$ and a magnetically actuated micro-mirror capable reaching ± 60° mechanical tilting and therefore full hemispheric optical coverage.

6.2 Summary of Casimir energy detection with superconductor in a tunable cavity

In chapter 4 we present a chip-scale system which, at cryogenic temperatures, can deposit and measure a superconducting thin film while simultaneously actuating and sensing a nano-mechanical metal plate. The *in situ* deposition process is achieved with two arrays of MEMS heaters that have been pre-loaded with a thick film of Pb, and can be pulsed at low temperature to evaporate small amounts of material. The thin film is produced by using a shadow mask to define a precise pattern of the evaporated Pb (incident on the mask from two sides), that connects four metallic measurement leads and also creates a thin section of Pb directly underneath the movable Au plate.

By driving a current with two sets of leads and measuring the voltage drop with the other two, we can measure the resistance of the Pb. We monitor this resistance as we vary the temperature of the cryostat and also the height of the plate. There was no observed change in the resistance vs. temperature behavior during this actuation.

We also drove the Au plate to its mechanical resonance and simultaneously monitored the resistance of the sample at that same frequency, while the temperature of the cryostat was just below T_c. Then, any Casimir induced changes on the T_c of the sample would manifest as changes in this resistance measurement. This technique resulted in much higher resolution, and larger plate displacements. In these experiments, the gap size was decreased until the Pb and Au surfaces were between 80 nm and 100 nm apart, but no effect on the T_c of the sample greater than 5 µK was observed. Our experiments conclude that for a Pb and Au cavity, with an interacting area of approximately $4\,\mu\mathrm{m}^2$, the Casimir energy does not shift the relative critical temperature of the superconductor ($\Delta T_c/T_c$) by more than 0.7 µK/K at zero applied field.

6.3 Future outlook

6.3.1 Searching for evidence of the Casimir energy

The carefully designed and executed Casimir energy experiments, both from other research groups and our own, have so far all come up short [Bimonte et al., 2008, Norte et al., 2018]. These null results are still useful however as they put upper bounds on the magnitude of the effect in a given system, and help guide the on-going theoretical work as well as inspire future experiments.

For example, in our device discussed in chapter 4, there are indeed future improvements to be made and experiments to try, including modified plate geometries allowing for greater actuation range, different superconducting materials, and critical magnetic field studies. Theory has implied that in low field limit, a 14 nm thick film of Al would shift by a few µK when an Au plate is brought to 6 nm away [Bimonte et al., 2008]. The required order of magnitudes in this theory are all achievable with our system and an observed shift may be possible to measure with just a few more iterations of the design and methodology.

As experimentalists, we hope to provide incremental pieces of concrete information that can be used to either confirm or challenge the theoretical picture of the world around us. What goes on energetically in the empty vacuum is one of the biggest questions in physics and we believe the apparatus and measurement technique presented here may be a useful piece in this puzzle.

6.3.2 The Casimir Effect in technology

Sensing the Casimir effect with an accelerometer is important for a couple of reasons. First of all, this platform for Casimir studies could allow experimenters to more easily investigate the Casimir Effect with non-trivial geometries, materials, or surface morphologies such as nanostructures or chiral metamaterials [Zhao et al., 2009, Van Zwol and Palasantzas, 2010, Intravaia et al., 2013, Woods et al., 2016, Tang et al., 2017].

Research applications aside, however, this work is particularly important because it is a stepping stone towards using the Casimir Effect as an engineering tool. By demonstrating that this quantum phenomenon can be harnessed in a commercially available platform, we believe it could lead to a new class of 'Casimir-enabled' devices. The Casimir force is known to scale with separation as d^{-4} compared to d^{-2} for electrostatics, so enhancements in sensitivity could be significant. The MEMS industry has already solved many of the engineering problems of producing reliable, high-performance devices at scale, so the jump necessary to incorporate this fascinating and practical quantum effect into MEMS may not be a very far one to make.

Appendix A

Supplementary information for Casimir force measurement

A.1 Surface roughness measurements

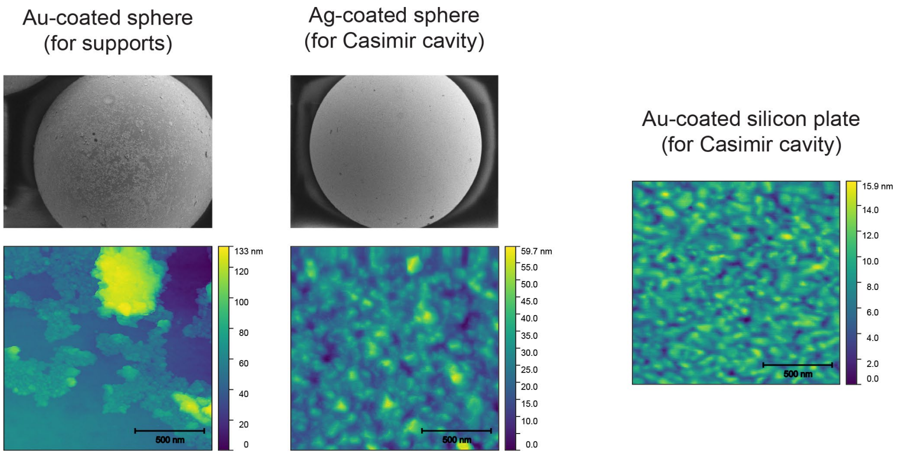
Au-coated sphere
(for supports)
Ag-coated sphere
(for Casimir cavity)
Au-coated silicon plate
(for Casimir cavity)
133 nm
120
100
80
60
40
20
0
500 nm
59.7 nm
55.0
50.0
45.0
40.0
35.0
30.0
25.0
20.0
15.0
10.0
0.0
500 nm
15.9 nm
14.0
12.0
10.0
8.0
6.0
4.0
2.0
0.0
500 nm

Figure A·1: SEM and AFM characterization of typical spherical and planar surfaces used in the device. The gold spheres had abnormally distributed roughness and tended to contain large (> 1 µm) debris and were therefore only used for structural purposes. The silver spheres and gold coated silicon plate showed much lower RMS roughness and were used to construct the Casimir cavity. The data shown are taken of samples prepared in the same manner as those used in the experiment but are not scans of the specific surfaces in our Casimir cavity.

A.2 Plate height sensitivity

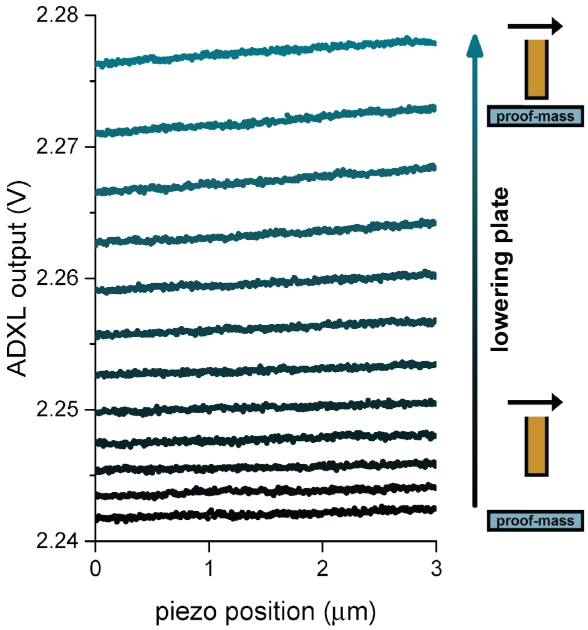

Figure A·2: Data illustrating the effect of the plate height on the sensor output due to interactions with the fringe fields of the sensing electrodes. These scans were taken with the plate starting at approximately 12 µm above the proof-mass (black) and decreasing in height by 1 µm for each dataset. At each height, the plate is scanned by 3 µm in the X direction with the piezo stack actuator. Data was taken over a portion of the proof-mass far away from the sphere with the sphere and plate both grounded.

A.3 Casimir force sensor temperature stability

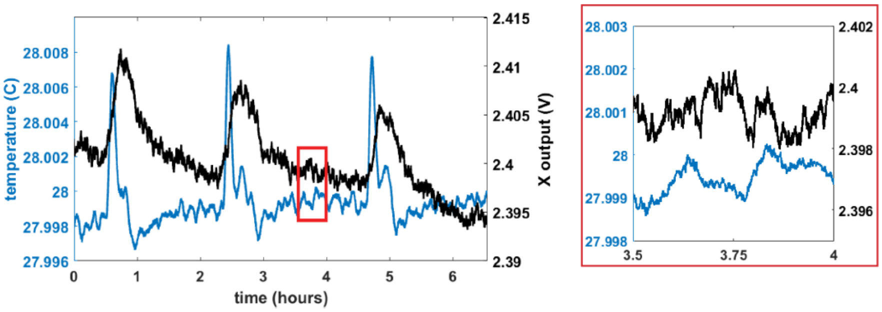

Figure A·3: Stability of the temperature and the sensor output in the temperature controlled enclosure over a 6.5 h period. The periodicity of both datasets is a result from the heaters in the building turning on and off every two hours. Long term drift in the ADXL signal is also apparent. Between these unstable periods (red inset), our PID system is able to hold the temperature to within 3 m°C for 0.5 h within the length of a full experiment. For this data, the plate is placed 1 µm away from the sphere and a bias of 1 V is applied between the two surfaces resulting in an applied electrostatic force of approximately 1 nN.

Appendix B

Supplementary information for Casimir energy detection

B.1 Deposition characteristics of MEMS micro-sources

A simple experiment was carried in a cryostat out to determine the deposition characteristics of the micro-sources. The pulse widths applied to the sources were fixed at 10 ms and the spacing between pulses was fixed at 2 s while the pulse height was slowly increased. A quartz crystal resonator is mounted opposite to the sources while oscillating at its natural frequency driven by a phase-locked loop circuit. In this loop, the output signal of the oscillator is converted a series of digital pulses with a zero-crossing detector and then a time delay is applied. This pulse signal is then used to trigger a wave function generator which drives the oscillator. An optimal delay can be found which maximizes the amplitude of the resonance. The measured frequency of this loop is therefore the natural resonance of the system. When mass is added to the resonator, the frequency shifts, and we can use this shift to determine when Pb begins to evaporate off of the micro-sources. Figure B·1 shows a schematic of this set-up as well as a plot of the pulse height along with the frequency. The sharp drop-off indicates that Pb has been added to the resonator, which happens around 5.1 V. The temperature of the cryostat is also monitored to ensure the frequency drop is not due to some heating effects from the pulsing.

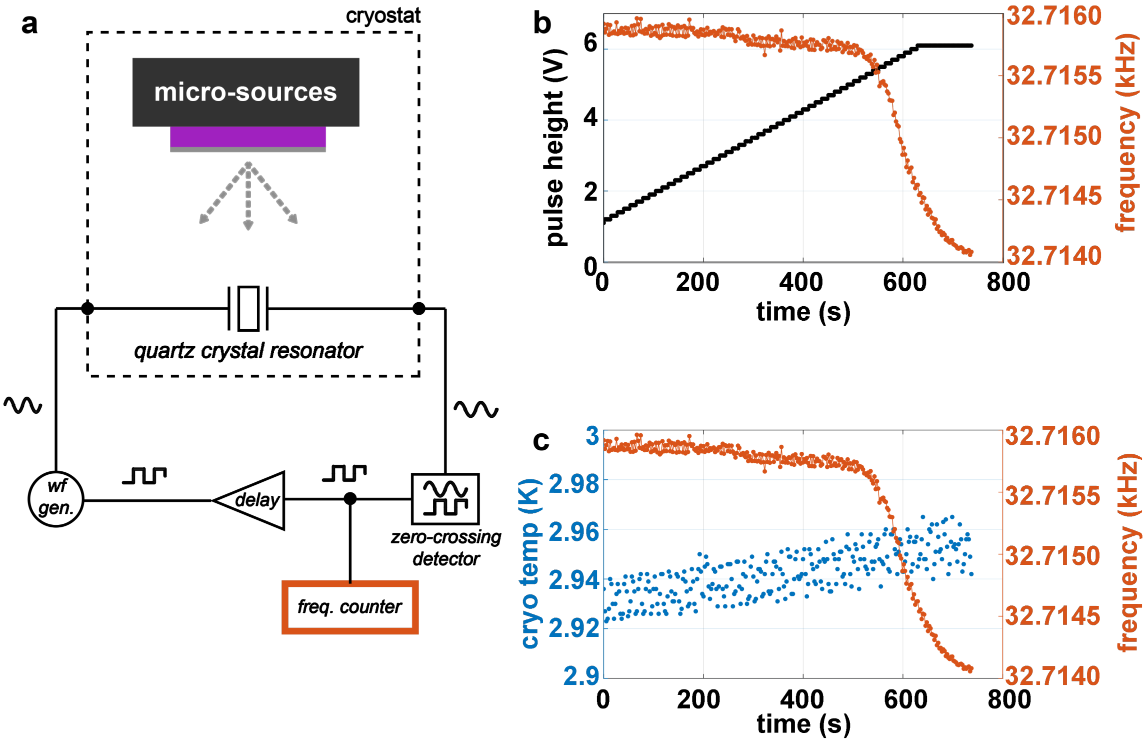

Figure B·1: Characterizing the micro-source deposition with a quartz crystal resonator and PLL. **a.** Micro-source die and un-capped quartz crystal resonator are placed opposite each other within the cryostat. The oscillator is driven with a phase-locked loop. The micro-sources are heated up with increasing pulse heights and the frequency is monitored. **b.** Plots of pulse height and frequency over time. Drop in frequency corresponds to onset Pb deposition which occurs at around 5.1 V. **c.** Plotting frequency versus cryostat temperature.

B.2 Determining plate height

B.2.1 Static actuation

Plotted in figure B·2 is data taken using a white light interferometer on a released plate on a Casimir cavity device. A full height map is taken while applying different DC voltages to the electrodes. The data is taken at room temperature, however, so comparing the voltage vs. displacement here will not be the same as comparing voltage to displacement at 3 K. When the device is cooled to low temperature, we observe

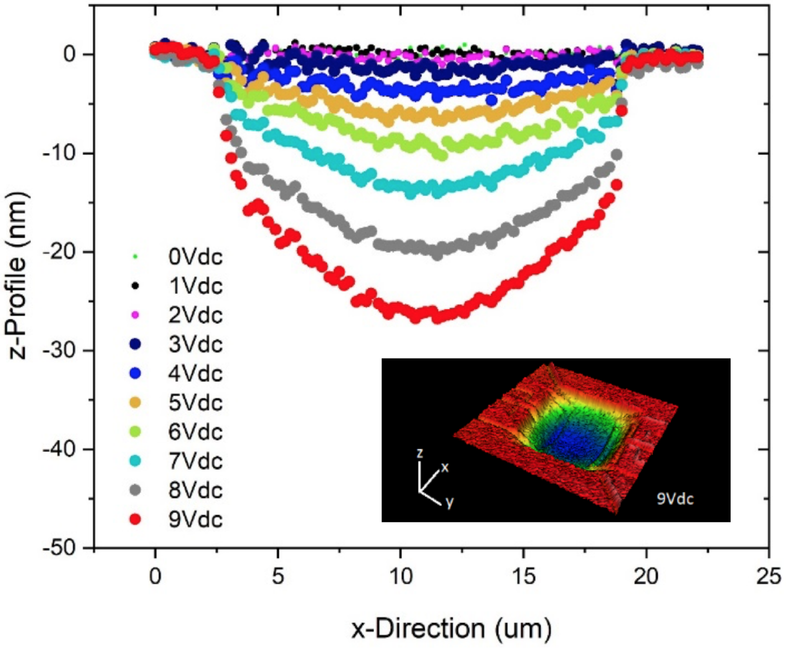

Figure B·2: White light interferometry data of a released Au plate at room temperature. As the DC bias voltage is increased, the electrostatic force pulls the plate downwards.

a 2X increase in resonant frequency. All other things equal, this would correspond to a 4X increase in structure stiffness. While it is difficult to make an accurate estimate of how far the plate deflects for a given applied voltage, it is correct to assume it will be less than what is observed at room temperature.

B.2.2 Post-experimental sample characterization and estimate of minimum gap size

After completing the experiment in the cryostat, AFM characterization of the nanocavity (with the top Au surface removed) is performed. Figure B·3 shows height measuremnts of the sample and the oxide stops. The sample height is measured to vary between 20 nm and 30 nm and the height of the oxide stops is 160 ± 1 nm.

Because the plate comes into contact with the pillars, it is possible to estimate the vertical displacement of the center of the plate, however in order to do this, an

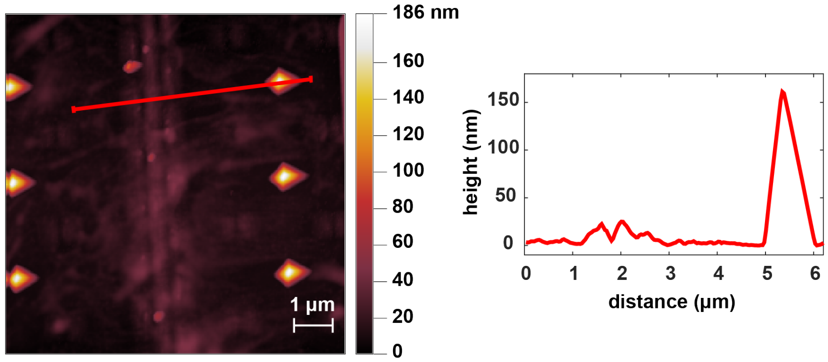

Figure B·3: AFM analysis of the cavity. The Pb sample and several oxide stops are visible in this scan. The height data corresponding to the red profile is plotted on the right.

assumption of the shape of the deformed Au plate needs to be made. In figure B·4, three models for the shape of the deformed plate are considered. The difficulty of this estimate is that the stress state of the suspended Au layer at cryogenic temperature is unknown. Therefore, by plotting a few different scenarios, a likely range of gap size can be obtained.

In all three models, no matter the deformed shape, the curve of the Au plate always goes through two points: the edge of the cavity (where the height is equal to 286 nm) and the top of the pillar (where the height is equal to 162 nm) First, a simple doubly-clamped linear beam model is considered. In this case, the gap size would be equal to 99 nm. In the next two models, the entire geometry is modeled in 3D in a finite element analysis program (COMSOL). First, the shape of the fundamental resonant mode is solved for with no initial stress on the Au. In this model, the reported frequency of this mode is only 400 kHz which does not agree with experiment (the measured resonance was approximately 1 MHz). This is because there is likely a large amount of uniaxial stress being applied to the Au plate along the direction in which it is anchored (due to the thermal contraction of the surrounding oxide). The

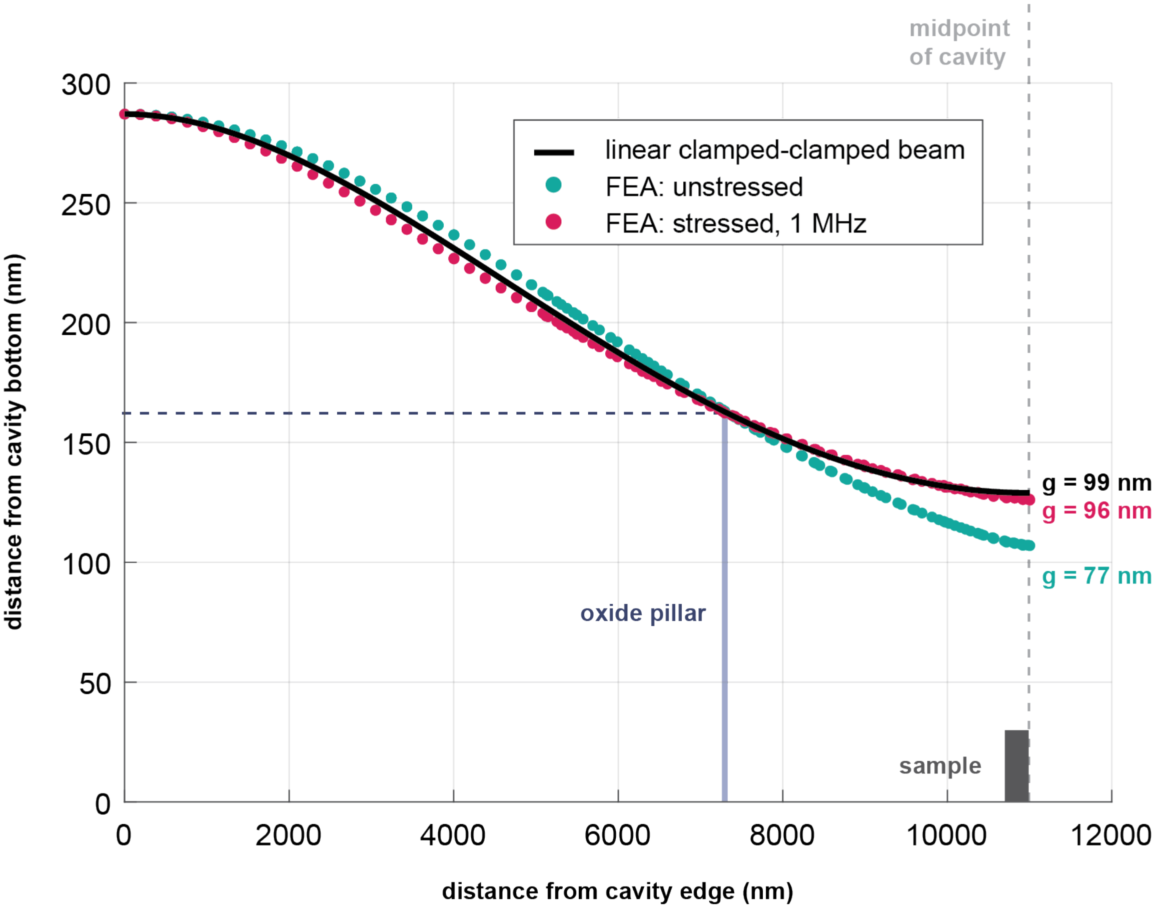

Figure B·4: Modeling the shape of the deformed Au plate. The analytical expression for a doubly-clamped beam is plotted in black, while results from FEA computations considering a zero-stress condition and a stressed condition are plotted in green and pink respectively.

second model adds in this external stress until the resonant frequency reaches 1 MHz. In this case, the shape of the deformed plate changes, leading to a gap size of 96 nm. The results of these three models are shown in figure B·4. Based on this analysis, we infer that the minimum gap size achieved in our system is likely somewhere between 80 nm and 100 nm.

References

Adams, P. W., Herron, P., and Meletis, E. I. (1998). First-order spin-paramagnetic transition and tricritical point in ultrathin Be films. *Physical Review B*, 58(6):R2952–R2955.

Adler, R. J., Casey, B., and Jacob, O. C. (1995). Vacuum catastrophe: An elementary exposition of the cosmological constant problem. *American Journal of Physics*, 63(7):620–626.

Alcubierre, M. (1994). The warp drive: hyper-fast travel within general relativity. *Classical and Quantum Gravity*, 11:L73–L77.

Analog Devices Data Sheet (2018). Data Sheet ADXL103/ADXL203. Technical report, Analog Devices.

Behunin, R. O., Intravaia, F., Dalvit, D. A., Neto, P. A., and Reynaud, S. (2012). Modeling electrostatic patch effects in Casimir force measurements. *Physical Review A - Atomic, Molecular, and Optical Physics*, 85(1):1–9.

Bimonte, G., Born, D., Calloni, E., Esposito, G., Hübner, U., Il, E., Rosa, L., Scaldaferri, O., Tafuri, F., and Vaglio, R. (2005a). The Aladin2 experiment: status and perspectives. (https://arxiv.org/abs/quant-ph/0511139).

Bimonte, G., Born, D., Calloni, E., Esposito, G., Huebner, U., Il'ichev, E., Rosa, L., Tafuri, F., and Vaglio, R. (2008). Low noise cryogenic system for the measurement of the Casimir energy in rigid cavities. *Journal of Physics A: Mathematical and Theoretical*, 41(16):164023.

Bimonte, G., Calloni, E., Esposito, G., Milano, L., and Rosa, L. (2005b). Towards Measuring Variations of Casimir Energy by a Superconducting Cavity. *Physical Review Letters*, 94(18):180402.

Bimonte, G., Calloni, E., Esposito, G., and Rosa, L. (2005c). Variations of Casimir energy from a superconducting transition. *Nuclear Physics B*, 726(3):441–463.

Boersma, S. L. (1996). A maritime analogy of the Casimir effect. *American Journal of Physics*, 64(5):539–541.

Bohr, M. T. and Young, I. A. (2017). CMOS Scaling Trends and Beyond. *IEEE Micro*, 37:20–29.

Broer, W., Palasantzas, G., Knoester, J., and Svetovoy, V. B. (2012). Roughness correction to the Casimir force at short separations: Contact distance and extreme value statistics. *Physical Review B - Condensed Matter and Materials Physics*, 85(15):1–13.

Bulgac, A., Magierski, P., and Wirzba, A. (2006). Scalar Casimir effect between Dirichlet spheres or a plate and a sphere. *Physical Review D*, 73(2):025007.

Casimir, H. B. G. (1948). On the attraction between two perfectly conducting plates. *Proceedings of the Koninklijke Nederlandse Akademie*, 360(April):793–795.

Casimir, H. B. G. and Polder, D. (1948). The Influence of Retardation on the London-van der Waals Forces. *Physical Review*, 73(4):360–372.

Chan, H. B., Aksyuk, V. A., Kleiman, R. N., Bishop, D. J., and Capasso, F. (2001a). Nonlinear micromechanical Casimir oscillator. *Physical review letters*, 87(21):211801.

Chan, H. B., Aksyuk, V. A., Kleiman, R. N., Bishop, D. J., and Capasso, F. (2001b). Quantum mechanical actuation of microelectromechanical systems by the Casimir force. *Science*, 291(5510):1941–1944.

De Man, S., Heeck, K., and Iannuzzi, D. (2009). No anomalous scaling in electrostatic calibrations for Casimir force measurements. *Physical Review A - Atomic, Molecular, and Optical Physics*, 79(2):4–7.

Decca, R. S., López, D., Fischbach, E., and Krause, D. E. (2003). Measurement of the Casimir Force between Dissimilar Metals. *Physical Review Letters*, 91(5):3–6.

Derjaguin, B. (1934). Untersuchungen über die Reibung und Adhäsion, IV. Theorie des Anhaftens kleiner Teilchen" [Analysis of friction and adhesion, IV. The theory of the adhesion of small particles]. *Kolloid-Zeitschrift*, 69:155–164.

Ekinci, K. L. and Valles, J. M. (1999). Morphology of Quench Condensed Pb Films near the Insulator to Metal Transition. *Physical Review Letters*, 82(7):1518–1521.

Elshurafa, A. M., Khirallah, K., Tawfik, H. H., Emira, A., Abdel Aziz, A. K., and Sedky, S. M. (2011). Nonlinear dynamics of spring softening and hardening in folded-mems comb drive resonators. *Journal of Microelectromechanical Systems*, 20(4):943–958.

Emig, T., Graham, N., Jaffe, R. L., and Kardar, M. (2007). Casimir Forces between Arbitrary Compact Objects. *Physical Review Letters*, 99(17):170403.

Garrett, J. L., Somers, D. A. T., and Munday, J. N. (2018). Measurement of the Casimir Force between Two Spheres. *Physical Review Letters*, 120(4):40401.

Geyer, B., Klimchitskaya, G. L., and Mostepanenko, V. M. (2002). Perturbation approach to the Casimir force between two bodies made of different real metals. *Physical Review A - Atomic, Molecular, and Optical Physics*, 65(6):6.

Gies, H. and Klingmüller, K. (2006). Worldline algorithms for Casimir configurations. *Physical Review D - Particles, Fields, Gravitation and Cosmology*, 74(4):1–12.

Han, H., Imboden, M., Stark, T., Del Corro, P. G., Pardo, F., Bolle, C. A., Lally, R. W., and Bishop, D. J. (2015). Programmable solid state atom sources for nanofabrication. *Nanoscale*, 7(24):10735–10744.

Hawking, S. W. (1992). Chronology protection conjecture. *Physical Review D*, 46(2):603–611.

Imboden, M., Chang, J., Pollock, C., Lowell, E., Akbulut, M., Morrison, J., Stark, T., Bifano, T. G., and Bishop, D. J. (2016). High-Speed Control of Electromechanical Transduction: Advanced Drive Techniques for Optimized Step-and-Settle Response of MEMS Micromirrors. *IEEE Control Systems*, 36(5):48–76.

Imboden, M., Han, H., Stark, T., and Bishop, D. (2017). Cryogenic Fab-on-a-Chip Sticks the Landing. *ACS Nano*, 11(9):8707–8716.

Imboden, M., Han, H., Stark, T., Lowell, E., Chang, J., Pardo, F., Bolle, C., Del Corro, P. G., and Bishop, D. J. (2014a). Building a Fab on a Chip. *Nanoscale*, 6(10):5049–5062.

Imboden, M., Morrison, J., Campbell, D. K., and Bishop, D. J. (2014b). Design of a Casimir-driven parametric amplifier. *Journal of Applied Physics*, 116(13):1–18.

Imboden, M., Morrison, J., Lowell, E., Han, H., and Bishop, D. J. (2014c). Controlling levitation and enhancing displacement in electrostatic comb drives of MEMS actuators. *Journal of Microelectromechanical Systems*, 23(5):1063–1072.

Intravaia, F., Koev, S., Jung, I. W., Talin, A. A., Davids, P. S., Decca, R. S., Aksyuk, V. A., Dalvit, D. A. R., and López, D. (2013). Strong casimir force reduction through metallic surface nanostructuring. *Nature Communications*, 4.

Israelachvili, J. (2011). *Intermolecular and Surface Forces.* Academic Press, third edition.

Jaffe, R. L. (2005). Casimir effect and the quantum vacuum. *Physical Review D*, 72(2):021301.

Javor, J. (2018). Sensitive MEMS-based Gradiometer. In *APS March Meeting*, Los Angeles. Bulletin of the American Physical Society.

Javor, J., Stange, A., Pollock, C., Fuhr, N., and Bishop, D. J. (2019). 100pT/cm Sensitive MEMS Resonant Magnetometer from a Commercial Accelerometer. *Ongoing work.*

Kim, W. J., Brown-Hayes, M., Dalvit, D. A. R., Brownell, J. H., and Onofrio, R. (2008). Anomalies in electrostatic calibrations for the measurement of the Casimir force in a sphere-plane geometry. *Physical Review A*, 78(2):020101.

Kingsbury, K. (2009). The Casimir Effect: A Comprehensive Exercise. (Retrieved from https://aphyr.com/media/comps.pdf).

Kittel, C. (1953). *Introduction to Solid State Physics.* Wiley & Sons.

Klimchitskaya, G. L., Mohideen, U., and Mostepanenko, V. M. (2009). The Casimir force between real materials: Experiment and theory. *Reviews of Modern Physics*, 81(4):1827–1885.

Kuhn, T. S., Rosenfeld, L., Bohr, A., and Rudinger, E. (1963). Interview of Hendrik Casimir. *Niels Bohr Library & Archives, American Institute of Physics, College Park, MD USA*, (https://www.aip.org/history-programs/niels-bohr-library/oral - histories/4550-1).

Lamoreaux, S. K. (1997). Demonstration of the Casimir Force in the 0.6 to 6 μ m Range. *Physical Review Letters*, 78(1):5–8.

Laurent, J., Sellier, H., Mosset, A., Huant, S., and Chevrier, J. (2012). Casimir force measurements in Au-Au and Au-Si cavities at low temperature. *Physical Review B*, 85(3):035426.

Leichtfried, G., Stickler, R., and Knabl, W. (2004). *Springer Handbook of Condensed Matter and Materials Data.* Springer.

Lewis, H. W. (1956). Superconductivity and Electronic Specific Heat. *Physical Review*, 101(3):939–939.

Lifshitz, E. M. (1956). The Theory of Molecular Attractive Forces between Solids. *Soviet Physics*, 2(1):73–83.

Liu, C. (2012). *Foundations of MEMS.* Prentice Hall, Upper Saddle River, NJ, second edition edition.

Maradudin, A. A. and Mazur, P. (1980). Effects of surface roughness on the van der Waals force between macroscopic bodies. *Physical Review B*, 22(4):1677–1686.

Milonni, P. (1994). *The Quantum Vacuum: An Introduction to Quantum Electrodynamics.* Academic Press.

Mohideen, U. and Roy, A. (1998). Precision Measurement of the Casimir Force from 0.1 to 0.9μm. *Physical Review Letters*, 81(21):4549–4552.

Neugebauer, C. A. and Webb, M. B. (1962). Electrical conduction mechanism in ultrathin, evaporated metal films. *Journal of Applied Physics*, 33(1):74–82.

Nonnenmacher, M., O'Boyle, M. P., and Wickramasinghe, H. K. (1991). Kelvin probe force microscopy. *Applied Physics Letters*, 58(25):2921–2923.

Norte, R. A., Forsch, M., Wallucks, A., Marinković, I., and Gröblacher, S. (2018). Platform for Measurements of the Casimir Force between Two Superconductors. *Physical Review Letters*, 121(3):1–6.

Ordal, M. A., Bell, R. J., Alexander, R. W., Long, L. L., and Querry, M. R. (1985). Optical properties of fourteen metals in the infrared and far infrared: Al, Co, Cu, Au, Fe, Pb, Mo, Ni, Pd, Pt, Ag, Ti, V, and W. *Applied Optics*, 24(24):4493.

Pollock, C., Barrett, L. K., Del Corro, P. G., Stange, A., Bifano, T. G., and Bishop, D. J. (2019a). PWM as a low cost method for the analog control of MEMS devices. *Journal of Microelectromechanical Systems*, 28(2):245–253.

Pollock, C., Imboden, M., Stange, A., Javor, J., Mahapatra, K., Chiles, L., and Bishop, D. J. (2018). Engineered PWM Drives for Achieving Rapid Step and Settle Times for MEMS Actuation. *Journal of Microelectromechanical Systems*, 27(3):513–520.

Pollock, C., Javor, J., Stange, A., Barrett, L. K., and Bishop, D. J. (2019b). Extreme angle, tip-tilt MEMS micromirror enabling full hemispheric, quasi-static optical coverage. *Optics Express*, 27(11):15318.

Poole, C. P. (2000). *Superconductivity.* Elsevier.

Rahi, S. J., Emig, T., Graham, N., Jaffe, R. L., and Kardar, M. (2009). Scattering theory approach to electrodynamic Casimir forces. *Physical Review D*, 80(8):085021.

Rioux, D., Vallières, S., Besner, S., Muñoz, P., Mazur, E., and Meunier, M. (2014). An analytic model for the dielectric function of Au, Ag, and their Alloys. *Advanced Optical Materials*, 2(2):176–182.

Roy, A. and Mohideen, U. (1999). Demonstration of the nontrivial boundary dependence of the casimir force. *Physical Review Letters*, 82(22):4380–4383.

Sabato, A., Niezrecki, C., and Fortino, G. (2017). Wireless MEMS-Based Accelerometer Sensor Boards for Structural Vibration Monitoring: A Review. *IEEE Sensors Journal*, 17(2):226–235.

Speake, C. C. and Trenkel, C. (2003). Forces between Conducting Surfaces due to Spatial Variations of Surface Potential. *Physical Review Letters*, 90(16):4.

Stange, A., Imboden, M., Javor, J., Barrett, L. K., and Bishop, D. J. (2019). Building a Casimir metrology platform with a commercial MEMS sensor. *Microsystems and Nanoengineering*, 5(1).

Stoer, J. and Bulirsch, R. (1993). *Introduction to Numerical Analysis.* Springer-Verlag, second edition.

Szulc, A. (2012). The Casimir Effect. (https://physics.bgu.ac.il/COURSES/QuantumMechCohen/Contributions/Casimir_Effect.pdf).

Tang, L., Wang, M., Ng, C. Y., Nikolic, M., Chan, C. T., Rodriguez, A. W., and Chan, H. B. (2017). Measurement of non-monotonic Casimir forces between silicon nanostructures. *Nature Photonics*, 11(2):97–101.

Tang, W. C., Lim, M. G., and Howe, R. T. (1992). Electrostatic Comb Drive Levitation and Control Method. *Journal of Microelectromechanical Systems*, 1(4):170–178.

Tez, S., Aykutlu, U., Torunbalci, M. M., and Akin, T. (2015). A Bulk-Micromachined Three-Axis Capacitive MEMS Accelerometer on a Single Die. *Journal of Microelectromechanical Systems*, 24(5):1264–1274.

Van Blokland, P. H. G. M. and Overbeek, J. T. G. (1978). Van der Waals forces between objects covered with a chromium layer. *Journal of the Chemical Society, Faraday Transactions 1: Physical Chemistry in Condensed Phases*, 74:2637–2651.

Van Zwol, P. J. and Palasantzas, G. (2010). Repulsive Casimir forces between solid materials with high-refractive-index intervening liquids. *Physical Review A - Atomic, Molecular, and Optical Physics*, 81(6):1–9.

Van Zwol, P. J., Palasantzas, G., and De Hosson, J. T. M. (2008). Influence of random roughness on the Casimir force at small separations. *Physical Review B - Condensed Matter and Materials Physics*, 77(7):1–5.

Weisskopf, V. (1935). Probleme der neueren Quantentheorie des Elektrons. *Naturwissenschaften*, 23(37):631–637.

Wheeler, J. A. (1955). Geons. *Physical Review*, 97(2):511–536.

Woods, L. M., Dalvit, D. A., Tkatchenko, A., Rodriguez-Lopez, P., Rodriguez, A. W., and Podgornik, R. (2016). Materials perspective on Casimir and van der Waals interactions. *Reviews of Modern Physics*, 88(4).

Younis, M. I., Ouakad, H. M., Alsaleem, F. M., Miles, R., and Cui, W. (2010). Nonlinear dynamics of MEMS arches under harmonic electrostatic actuation. *Journal of Microelectromechanical Systems*, 19(3):647–656.

Zhang, W. M., Yan, H., Peng, Z. K., and Meng, G. (2014). Electrostatic pull-in instability in MEMS/NEMS: A review. *Sensors and Actuators, A: Physical*, 214:187–218.

Zhao, R., Zhou, J., Koschny, T., Economou, E. N., and Soukoulis, C. M. (2009). Repulsive casimir force in chiral metamaterials. *Physical Review Letters*, 103(10):1–4.

Ziegler, W. T., Young, R. A., and Floyd, A. L. (1953). Crystal Structure and Superconductivity of Lanthanum The Crystal Structure and Superconductivity of Lanthanum1-2. *Journal of the American Chemical Society*, 75(5):1215–1221.

Zou, J., Marcet, Z., Rodriguez, A. W., Reid, M. T., McCauley, A. P., Kravchenko, I. I., Lu, T., Bao, Y., Johnson, S. G., and Chan, H. B. (2013). Casimir forces on a silicon micromechanical chip. *Nature Communications*, 4.

CURRICULUM VITAE

[redacted]

[redacted]

[redacted]